博 士 学 位 論 文
Doctoral Dissertation

Exploration and Mechanism Study of Catalysts for Efficient Electrocatalytic Nitrate Reduction to Ammonia

(効率的な電極触媒による硝酸塩のアンモニアへの還元のための触媒の探索とメカニズムの研究)

東北大学大学院環境科学研究科
Graduate School of Environmental Studies, Tohoku University

	先進社会環境学専攻	専攻 major／コース course
学籍番号 Student ID No.	C0GD1005	
氏　名 Name	饒 旭峰	

指　導　教　員 Supervisor at Tohoku Univ.	井上 千弘 教授	
研 究 指 導 教 員 Research Advisor at Tohoku Univ.		
審　査　委　員 （〇印は主査） Dissertation Committee Members Name marked with "○" is the Chief Examiner	○　井上 千弘 教授	
	1　高橋 英志 教授	2　上高原 理暢 教授
	3	4
	5	6

Abstract

Ammonia is useful chemical. About 80% of ammonia is used for fertilisers, while the remainder is used for various industrial applications, such as plastics, explosives and synthetic fibres. While the use of ammonia as a fuel show promise in the context of clean energy transitions. Ammonia as a fertilizer, raise one third of the population. 50% of the protein nitrogen in human body comes from ammonia fertilizers. Most of ammonia is produced by the traditional HB process, using natural gas as the raw material under high temperature and pressure conditions. Through this method, global ammonia production exceeds 200 million tons. It accounts for about 2% of the world's energy consumption and generates 3% of carbon dioxide emissions. Recently, due to the war between Ukraine and Russia, the price of natural gas has risen more than 10 times. Affected by the rise in raw materials, the price of fertilizers has more than tripled. The population of the earth has exceeded 8 billion in this year. So, to raise 8 billion population, the world needs more ammonia in the future, but can't afford more for economy and environment. On the other hand, nitrate exists in nature in large quantities as a common pollutant. High concentrations of nitrate in the water table can cause drinking water to become toxic. High levels of nitrate in surface waters will cause overstimulation of algal growth, such as blooms. These blooms block sunlight and create anoxic zones which create an un-inhabitable environment for marine life, often referred to as eutrophication. Treating water contaminated with nitrates costs a lot of money every year. With the aim to tackle this problem and recycle the fixed nitrogen, electrochemical nitrate reduction serves as a “two birds-one stone” approach as nitrate can be potentially converted to ammonia.

In this dissertation, the mechanism of electrochemical nitrate reduction to ammonia was studied in depth, and the influence of various metal catalysts on the reaction was discussed. In Chapter 2, we combine density functional theory (DFT) and experimental methods to reveal the important role of nitrate adsorption energy in determining the reactivity. This finding sheds new light on understanding key steps in the electrochemical ammonia synthesis process.

In the study in Chapter 3, we systematically compared different metal catalysts and found that copper and cobalt metal catalysts exhibited excellent catalytic performance. Further research shows that the performance of copper and cobalt-based catalysts is likely to be directly affected by the element species, which provides important clues for the design of more efficient catalysts.

The Chapter 4 focuses on Co_3O_4 catalysts, and Co_3O_4-CP is obtained by electrodeposition on carbon paper. This catalyst not only exhibits a rate exceeding that of conventional HB in ammonia synthesis, but also maintains a Faradaic efficiency of nearly 100% for a long time, showing broad application potential. This finding contributes a new strategy for the development of sustainable ammonia synthesis technology.

In summary, this study systematically investigated the mechanism of electrochemical nitrate reduction to ammonia and the performance of various metal catalysts. These findings have important implications for understanding the principles of key steps in the ammonia synthesis process and optimizing catalyst design. In addition, our research results also provide a valuable reference for realizing efficient and sustainable ammonia synthesis technology.

Keywords: Nitrate reduction to ammonia; electrocatalyst; pollutant removal

Menu

List of Abbreviations

Nitrate reduction reaction: NRR

Hydrogen evolution reaction: HER

Reversible hydrogen electrode: RHE

Faradaic efficiency: FE

Linear sweep voltammetry: LSV

Projector Augmented Wave: PAW

Perdew-Burke-Ernzerhof: PBE

Perdew-Burke-Ernzerhof Generalized Gradient Approximation: PBE-GGA

Generalized Gradient Approximation: GGA

Local Density Approximation: LDA

Vienna Ab initio Simulation Package: VASP

Zero point energy: ZPE

National Institute of Standards and Technology: NIST

Chapter 1 General Introduction

1-1 Crucial Compound – Ammonia

Ammonia (NH_3) is a colorless gas with a strong odor at room temperature and pressure. It was purified and isolated by Joseph Priestley, Joseph Black, Carl Wilhelm Scheele and Peter Woulfe. The chemical composition was first determined in the research of Claude Louis Berthollet in the eighteenth century. Because of its excellent solubility in water, it is often used as an important source of alkaline nitrogen in the chemical industry. Ammonia is used as a raw material or intermediate in the production of plastics, fibers, explosives, nitric acid, as well as dyes and pharmaceuticals. About 80% of the ammonia is used to make fertilizers such as urea, ammonium nitrate, calcium ammonium nitrate, diammonium phosphate and urea ammonium nitrate. Ammonia is also the cornerstone of the synthesis of many pharmaceutical and chemical products.

Although most of ammonia is currently used to produce fertilizers, it is also considered a high energy density carbon-free fuel and hydrogen carrier. Using ammonia as a fuel to react with oxygen in a fuel cell can quietly release energy and only produce water and nitrogen. It is a green fuel with absolutely no greenhouse gas emissions. Compared to hydrogen, the volumetric energy density of liquid ammonia (12,822 MJ/m^3) is higher than that of liquid hydrogen (8496 MJ/m^3) [1]. What's more, hydrogen liquefaction is expensive, it needs to be cooled to -253 ℃, and the energy loss is large (the energy required for hydrogen liquefaction is 30% of the liquefied hydrogen combustion capacity), and there is inevitable evaporation loss. The liquefaction temperature of ammonia is only −33 ℃, and it can be easily stored in steel cylinders at one-sixteenth the cost of hydrogen [2].

$$3NH_3 + 3O_2 \rightarrow 2N_2 + 6H_2O$$

Humans have a long history of utilizing ammonia. When human society entered the agricultural era, farmers would fertilize in various ways in different parts of the world. In Asia, humans scattered their excrement in rice fields. In Europe and America, humans pulverized animal bones for used as fertilizer. Until Justus Fresher von Liebig discovered that nitrogen can be supplied in the form of ammonia and recognized the possibility of replacing natural fertilizers with chemical fertilizers in 1840. After that, the demand for ammonia used as a fertilizer and as a raw material for industry has been growing steadily along with the population growth. The Chincha Islands in Peru were developed for their ammonia-rich guano deposits and exported to Europe and the Americas in the 1860s. Until more than 10 million tons of guano deposits are completely exhausted. Subsequently, research began on the source of ammonia minerals to replace guano. The large quantities of saltpeter in the Atacama Desert were developed as new fertilizers. But these non-renewable resources were predicted at the beginning of the twentieth century to be unable to meet the needs of human society in the future. To ensure food

security for a growing population, a new economical and reliable method of obtaining ammonia must be developed.

Food security problem was particularly serious in Germany. Germany's arable land is barren, and food production relies heavily on saltpeter imported from Chile. Influenced by this, in 1895, German chemists Adolf Frank and Nikodem Caro successfully used calcium carbide reacted with nitrogen to obtain nitrolime. Then continue to react with water to obtain ammonia fertilizer.

$$CaC_2 + N_2 \rightarrow CaCN_2 + C \text{ (1-1)}$$

$$CaCN_2 + 3H_2O \rightarrow CaCO_3 + 2NH_3 \text{(1-2)}$$

The CaC_2 powder and N_2 reacted for several hours and maintained a high temperature in excess of 1000°C, producing about 0.005% ammonia [3]. This is the first breakthrough in human history to synthesize ammonia from atmospheric nitrogen, albeit with poor efficiency. Since 1908, five ammonia fertilizer plants have been established in Germany with a total capacity of 500,000 tons per year. It was the cheapest ammonia fertilizer available at the time and had additional efficacy against weeds and plant pests, giving it a great advantage over traditional fertilizers.

During the ensuing World War I, the Allies blocked the German trade in raw materials. Therefore, there is a need to find a more efficient way to prepare ammonia as a precursor for explosives or as a fertilizer.

$$N_2 + 3H_2 \leftrightarrows 2NH_3 \text{(1-3)}$$

In 1913, Fritz Haber and Carl Bosch developed a new method called Haber-Bosch process to synthesize ammonia. This method uses Fe as a catalyst and nitrogen and hydrogen as raw materials to synthesize ammonia under the conditions of 200 atmospheres and 400°C. The Haber-Bosch process can achieve ammonia yields as high as 20 % under such conditions. This revolutionary technological advance has greatly reduced the energy demand of the ammonia synthesis industry and made possible large-scale industrial synthesis of ammonia. For this, Fritz Haber was awarded the Nobel Prize in Chemistry in 1918. The Haber-Bosch process freed human beings from the passive situation of relying only on natural nitrogen fertilizer mineral resources, especially sodium nitrate, which accelerated the development of world agriculture and greatly increased food production [4]. At present, there is 235 million tons of synthetic ammonia in the world, with sales exceeding 100 billion US dollars. More than 40% of the world's population relies on fertilizers for food production, and more than 50% of the nitrogen in the human body comes from synthetic ammonia [5].

All in all, ammonia is an important chemical, whether it is used as a fertilizer to feed humans or as a green fuel. Human society needs more ammonia but cannot afford more emissions.

1-2 Potential green ammonia synthesis technology

Today, more than 200 million tons of ammonia is produced annually through the Haber-Bosch process to meet the needs of human society. It requires a source of H_2 gas, which is generated from natural gas in a reaction using pressurized superheated steam. Carbon dioxide is left behind, accounting for about 50 % of the emissions from the entire process. The second feedstock N_2 gas is easily collected from air, which contains 78% nitrogen. But creating the pressure needed to fuse hydrogen and nitrogen in a reactor consumes more fossil fuel, which means more CO_2. Emissions add up: Ammonia production consumes about 2% of global energy and generates 3% of CO_2 [5].

The price of natural gas, an important feedstock for ammonia synthesis, has skyrocketed recently due to the war between Russia and Ukraine. As of August 2022 in Japan, liquefied natural gas import prices have raised 10 times compared to 2019. This has directly led to the increase in the price of chemical fertilizers, and ammonia fertilizers represented by urea have risen by 260 %. Therefore, it is very attractive to develop a new technology to replace the Haber-Bosch process that has been used for more than a century, whether it is to feed the more than 7.7 billion people on the planet or reduce carbon emissions.

1-2-1 Electrocatalytic reduction of nitrogen to ammonia

As an environmentally friendly NH_3 synthesis technology, electrocatalytic reduction nitrogen under ambient conditions is considered as a promising alternative to the energy-intensive Haber-Bosch process. More and more research has been devoted to this topic recently, with over 500 papers published in this field in the past 5 years [6]. This method uses H_2O and N_2 as raw materials, and relies on electricity as the driving force to gently produce ammonia. The whole process is completely carbon-free.

$$2N_2 + 6H_2O \rightarrow 4NH_3 + 3O_2 \quad (1\text{-}4)$$

Despite the great practical value of this approach, unsatisfactory catalytic activity and selectivity remains a major obstacle. Low Faradaic efficiency (FE) and ammonia yield rate limit its practical application.

In order to find an efficient catalyst for the reduction of nitrogen to ammonia, it is first necessary to understand the reaction mechanism. For ammonia synthesis in aqueous solution, it is generally carried out by 6 electron transfer.

$$N_2 + 6H^+ + 6e^- \rightarrow 2NH_3 \text{(1-5)}$$

This reaction mechanism consists of dissociation and association, which mainly involve distal, alternating, and enzymatic pathways as shown in Fig.1-1 [7]. For the dissociative mechanism, the triple bond of the nitrogen molecule adsorbed on the catalyst may be cleaved before protonation as shown in Fig. 1-1a. Subsequently, the nitrogen atom remaining on the surface of catalyst is independently transformed into NH_3 and released. Since breaking triple bonds requires a large amount of energy (941 kJ/mol), this explains why the Haber-Bosch process following the dissociation pathway requires extreme conditions to operate. For the associative pathway, it includes 3 parts: (1) adsorption of nitrogen on the surface of catalyst; (2) triple bond of nitrogen split and step-by-step protonation; (3) the departure of the product. First, a nitrogen molecule is adsorbed onto catalytic active sites (*) without requiring much energy to directly break the triple bond, as follows:

$$N_2 + * \rightarrow *N_2 \text{(1-6)}$$
$$*N_2 + e^- + H^+ \rightarrow *NNH \text{(1-7)}$$
$$*NNH + e^- + H^+ \rightarrow *NNH_2 \text{(1-8)}$$
$$*NNH_2 + e^- + H^+ \rightarrow *N + NH_3 \text{(1-9)}$$
$$*N + 3e^- + 3H^+ \rightarrow NH_3 + * \text{(1-10)}$$

The activation energy for ammonia synthesis (12.3 kJ/mol) via the associative pathway is much lower than that of the Haber-Bosch process [8]. According to the different protonation sequence and direction of nitrogen atoms, it is divided into distal or alternating as shown in Fig. 1-1b and 1-1c. The first way in which hydrogen atoms are added to the outer nitrogen atoms is by associating distal pathways. After synthesizing an ammonia molecule and leaving the catalyst surface, the hydrogen atom continues to react with another nitrogen atom to form ammonia, as follow:

$$*N_2 + 3e^- + 3H^+ \rightarrow NH_3 + *N \text{(1-11)}$$
$$*N + 3e^- + 3H^+ \rightarrow NH_3 + * \text{(1-12)}$$

For the associative alternation pathway, the two nitrogen atoms are successively reacted by the hydrogen atoms until finally the two products ammonia is released simultaneously:

$$*N_2 + 4e^- + 4H^+ \rightarrow *NH_2NH_2 \text{(1-13)}$$
$$*NH_2NH_2 + 2e^- + 2H^+ \rightarrow 2NH_3 + * \text{(1-14)}$$

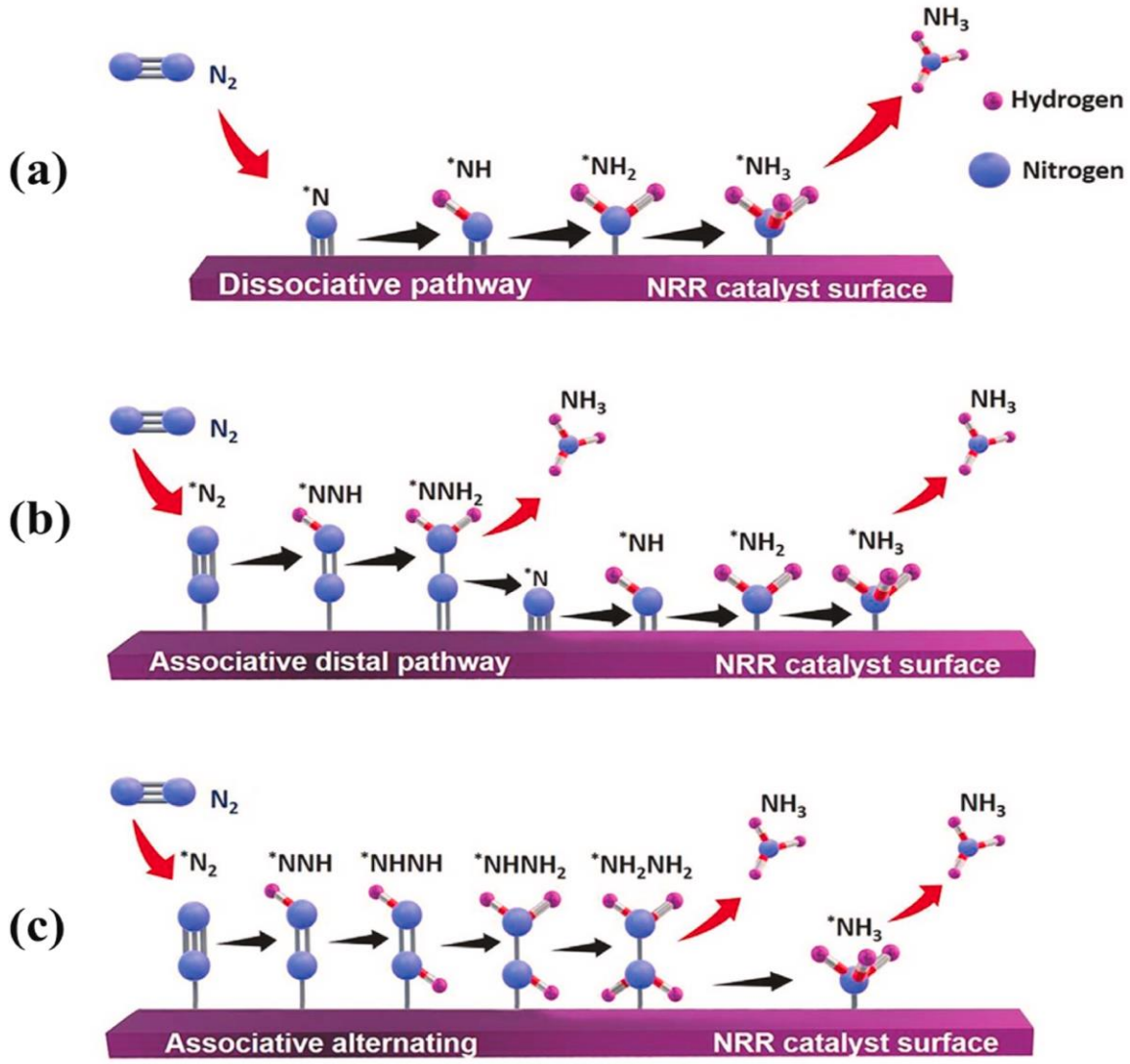

Fig. 1-1. Schematic illustration of the three mechanisms for electrocatalytic nitrogen reduction to ammonia [9].

These mechanisms allow electrochemical nitrogen reduction to ammonia to proceed without high temperature or pressure. Since the first step in the mechanism of the reaction is nitrogen adsorption and activation on the catalyst surface, the interaction between nitrogen and catalyst is an important prerequisite to start the catalytic reaction. According to the Sabatier principle, the catalyst-reactant bond can neither be too weak nor too strong [10]. Too weak makes the catalyst less likely to adsorb and activate the reactants. Too strong will poison the catalyst surface, and both will severely impair catalytic activity. Metal elements with moderate binding force, such as Ru, Rh, and Ir, show enhanced catalytic performance.

Both theoretical and experimental studies have shown that the electrons in the unfilled d orbitals in the catalyst can promote the catalytic reaction [11, 12]. Some metal elements (Au, Ag, Ru, Rh, Ir,

Pd, Pt, Re and Os) containing unfilled d orbitals can also show strong catalytic performance. The competitive hydrogen evolution reaction (HER) directly affects the efficiency of reaction, since the reaction potential of HER (0 V_{RHE}, RHE: reversible hydrogen electrode) is very close to that of nitrogen reduction (0.1 V_{RHE}). Therefore, metals (Ag and Au) with extremely poor HER reactivity can also achieve better catalytic activity.

Table 1-1 Catalytic performance of catalysts for nitrogen reduction to ammonia.

Catalyst	NH_3 detection method	NH_3 yield rate	FE (%)	Ref.
Au nanorods	Nessler's reagent	1.648 μg h^{-1} cm^{-2} at −0.2 V_{RHE}	4.0	[13]
Au clusters	Indophenol blue	18.9 μg h^{-1} cm^{-2} at −0.2 V_{RHE}	37.8	[14]
Au film	Indophenol blue	30.5 μg h^{-1} $mg_{cat.}^{-1}$ at −0.2 V_{RHE}	5.0 at −0.2 V_{RHE}	[15]
Au nanostar	Nessler's reagent Indophenol blue	2.6 μg h^{-1} cm^{-2} at −0.2 V_{RHE}	10.2	[16]
Au/TiO_2	Salicylate method	21.4 μg h^{-1} $mg_{cat.}^{-1}$ at −0.2 V_{RHE}	8.1	[17]
Au-Fe_3O_4	Indophenol blue	21.42 μg h^{-1} $mg_{cat.}^{-1}$ at −0.2 V_{RHE}	10.5	[18]
Au/WO_{3-x}	Indophenol blue	23.15 μg h^{-1} $mg_{cat.}^{-1}$ at −0.2 V_{RHE}	14.7	[19]
Au/CoO_x	Indophenol blue	15.1 μg $h^{-1}$$cm^{-2}$ at −0.5 V_{RHE}	19	[20]
Au/TiO_2	Nessler's reagent	64.6 μg h^{-1} $mg_{cat.}^{-1}$ at −0.4 V_{RHE}	29.5	[21]
Au/Ti_3C_2	Indophenol blue	30.06 μg h^{-1} $mg_{cat.}^{-1}$	18.3	[22]
Au/CeO_x	Indophenol blue	8.3 μg h^{-1} $mg_{cat.}^{-1}$	10.1	[23]
B-Ag	Nessler's reagent	26.48 μg h^{-1} $mg_{cat.}^{-1}$	8.9	[24]
BD-Ag/AF	Indophenol blue	2.07×10^{-11} mol s^{-1} cm^{-2} at −0.6V_{RHE}	7.4, at −0.6 V_{RHE}	[25]
Ag/CPE	Indophenol blue	4.62×10^{-11} mol s^{-1} cm^{-2} at −0.6 V_{RHE}	4.8, at −0.6V_{RHE}	[26]
Ag-rGO	Indophenol blue	18.86 μg h^{-1} $mg_{cat.}^{-1}$ at −0.7 V_{RHE}	3.6, at − 0.7 V_{RHE}	[27]
AgTPs	Indophenol blue	58.5 μg h^{-1} $mg_{cat.}^{-1}$ at −0.25 V_{RHE}	25, at −0.25 V_{RHE}.	[28]
Ru/C	Ion chromatography	0.25 μg h^{-1} cm^{-2} at −0.96 $V_{Ag/AgCl}$	0.9	[29]

		0.21 μg h^{-1} cm^{-2} at −1.10 $V_{Ag/AgCl}$	0.3	
Ru NPs	Indophenol blue	24.88 μg h^{-1} $mg_{cat.}^{-1}$ at −0.15 V_{RHE}	0.4	[30]
Ru NPs	Indophenol blue	5.5 mg h^{-1} cm^{-2} at −0.1 V_{RHE}	5.4	[31]
		21.4 mg h^{-1} cm^{-2} at −0.1 V_{RHE}		
Ru-PEI	Indophenol blue	188.90 μg h^{-1} $mg_{cat.}^{-1}$ at −0.2 V_{RHE}	30.9	[32]
Ru	Indophenol blue	23.88 μg h^{-1} $mg_{cat.}^{-1}$ at −0.2 V_{RHE}	0.2	[33]
3D Rh	Indophenol blue	35.58 μg h^{-1} mg_{cat}^{-1} at −0.2 V_{RHE}	1.2	[34]
Ru/Ti	Salicylate method	7.31 μg h^{-1} cm^{-2} at 2 mA cm^{-2}	-	[35]
Rh/Ti	Salicylate method	0.918 μg h^{-1} cm^{-2} at 2 mA cm^{-2}	-	[35]
np-$PdH_{0.43}$	Indophenol blue	20.4 μg h^{-1} $mg_{cat.}^{-1}$ at −0.15 V_{RHE}	43.6	[36]
Pt/TiO_2	Indophenol blue	2520.5 μg h^{-1} $mg_{cat.}^{-1}$ at −0.1 V_{RHE}	1.6	[37]
Pd/TiO_2		1847.3 μg h^{-1} $mg_{cat.}^{-1}$ at −0.1 V_{RHE}	2.6	[37]
Pd/C	Indophenol blue	4.5 μg h^{-1} mg_{Pd}^{-1} at -0.1 V_{RHE}	8.2 at -0.1 V_{RHE}	[38]
30 wt% Pt/C	Nessler's reagent	69.8 μg h^{-1} cm^{-2} at 1.6 V cell voltage	0.5	[39]
30 wt% Pt/C	Nessler's reagent	9.37×10^{-6} mol m^{-2} s^{-1} at 1.2 V cell voltage	0.8	[40]
Pt NPs	Indophenol blue	4.049×10^{-11} mol s^{-1} cm^{-2} at 0.5 V cell voltage	0.01	[41]
Pt-HEX	Indophenol blue	26.4 μg h^{-1} cm^{-2} at −0.3 V_{RHE}	1.8	[42]
Pt-FeP/C	Indophenol blue	10.22 μg h^{-1} cm^{-2} at −0.05 V_{RHE}	15.3	[43]
Pt/TiO_{2-x} NA	Indophenol blue	4.81×10^{-10} mol s^{-1} cm^{-2} at –0.35 V_{RHE}	14.9 at –0.35 V_{RHE}	[44]
Ir	Indophenol blue	2.763×10^{-11} mol s^{-1} cm^{-2} at 0.25 V cell voltage	0.1	[41]
Ir/C	Nessler's reagent	2.09×10^{-12} mol s^{-1} cm_{ECSA}^{-2} at –0.4 V_{RHE}	0.02	[45]
AuP/NF	Indophenol blue	36.52 μg h^{-1} μg_{cat}^{-1} at –0.2 V_{RHE}	20.3	[46]
Au_1/C_3N_4	Indophenol blue	1305 μg h^{-1} $mg_{cat.}^{-1}$ at −0.1 V_{RHE}	11.1	[47]

Au_1/C_3N_4	Indophenol blue	2.32 μg h^{-1} cm^{-2} at −0.2 V_{RHE}	12.3	[48]
SA-Ag/NC	Indophenol blue Ion chromatography	270.9 μg h^{-1} $mg_{cat.}^{-1}$ at −0.6 V_{RHE}	21.9	[49]
Pt SAs/WO_3	^{15}N isotope	342.4 μg h^{-1} $mg_{cat.}^{-1}$ at −0.2 V_{RHE}	31.1	[50]
Ru-Mo_2CT_X	Indophenol blue	40.57 μg h^{-1} $mg_{cat.}^{-1}$ at −0.3 V_{RHE}	25.8	[51]
Ru_1/g-C_3N_4	Nessler's reagent	23.0 μg h^{-1} $mg_{cat.}^{-1}$ at −0.05 V_{RHE}	8.3	[52]
Ru@ZrO_2	Indophenol blue	3665 μg h^{-1} $mg_{cat.}^{-1}$ at −0.11 V_{RHE}	21	[53]
Ru SAs/N-C	Indophenol blue	120.9 μg h^{-1} $mg_{cat.}^{-1}$ at −0.2 V_{RHE}	29.6	[54]
Au-Cu	Indophenol blue	154.91 μg h^{-1} $mg_{cat.}^{-1}$ at −0.2 V_{RHE}	55.0	[55]
Au_6/Ni	Nessler reagent	7.4 μg h^{-1} $mg_{cat.}^{-1}$ at −0.14 V_{RHE}	67.8	[56]
$Pt_{93}Ir_7$	Indophenol blue	28.0 μg h^{-1} cm^{-2} at −0.3 V_{RHE}	40.8	[57]
Pt_3Fe NWs	Nessler's reagent	18.3 μg h^{-1} mg_{cat}^{-1} at −0.05 V_{RHE}	7.3	[58]
PdCu NPs	Indophenol blue	35.7 μg h^{-1} $mg_{cat.}^{-1}$ at −0.1 V_{RHE}	11.5	[59]
Pd-Ag	Nessler's reagent	45.6 μg h^{-1} cm^{-2} at −0.6 V_{RHE}	19.6	[60]
Pd_1Ag_1	Nessler's reagent Indophenol blue	24.1 μg h^{-1} mg^{-1} at −0.2 V_{RHE}	1.7 at −0.0 V_{RHE}	[61]
Pd-Co/CuO	Indophenol blue	10.04 μg h^{-1} $mg_{cat.}^{-1}$ at −0.2 V_{RHE}	2.2	[62]
PdAgCu	Nessler's reagent Indophenol blue	40.4 μg h^{-1} $mg_{cat.}^{-1}$ at −0.2 V_{RHE}	-	[63]
Pd_3Pb	Indophenol blue	18.2 μg h^{-1} mg_{cat}^{-1} at −0.2 V_{RHE}	21.5	[64]
Au_1Co_1	Nessler's reagent Indophenol blue	36.82 μg h^{-1} $mg_{cat.}^{-1}$ at −0.2 V_{RHE}	22.0	[65]
$Pd_{0.2}Cu_{0.8}$	Indophenol blue	2.80 μg h^{-1} $mg_{cat.}^{-1}$ at −0.2 V_{RHE}	4.5 at −0.0 V_{RHE}	[66]
CuAg/Ti_3C_2	Indophenol blue	4.12 μmol h^{-1} cm^{-2} at −0.5 V_{RHE}	9.8	[67]
RuPt/C	Nessler's reagent	5.1×10^{-9} g s^{-1} cm^{-2} at −0.123 V_{RHE}	13.2	[68]
Ru/Cu_2O	Indophenol blue	37.4 μg h^{-1} $mg_{cat.}^{-1}$ at −0.2V_{RHE}	17.1	[69]
$Rh_{0.6}Ru_{0.4}$	Indophenol blue	57.75 μg h^{-1} $mg_{cat.}^{-1}$ at −0.2 V_{RHE}	3.4	[70]

PdO/Pd	Indophenol blue	18.2 μg h^{-1} $mg_{cat.}^{-1}$ at 0.1 V_{RHE}	11.5	[71]
PdP_2	Indophenol blue	30.3 μg h^{-1} $mg_{cat.}^{-1}$ at −0.1 V_{RHE}	12.6	[72]
IrP_2	Indophenol blue	94.0 μg h^{-1} $mg_{cat.}^{-1}$ at −0.2 V_{RHE}	17.8	[73]
$Ru_{88}Pt_{12}$	Nessler's reagent	47.1 μg h^{-1} mg_{cat}^{-1} at −0.2 V_{RHE}	8.9	[74]
AuPdP	Indophenol blue	18.78 μg h^{-1} $mg_{cat.}^{-1}$ at −0.3 V_{RHE}	15.4	[75]
Pd-Ag	Indophenol blue	9.73 μg h^{-1} $mg_{cat.}^{-1}$ at −0.2 V_{RHE}	18.4	[76]
AuCuB	Indophenol blue	13.2 μg h^{-1} $mg_{cat.}^{-1}$ at −0.5 V_{RHE}	12.8	[77]
Au@C	Indophenol blue	241.9 μg h^{-1} $mg_{cat.}^{-1}$ at −0.45 V_{RHE}	40.5	[78]
Au@CeO_2	Indophenol blue	293.8 μg h^{-1} $mg_{cat.}^{-1}$ at −0.4 V_{RHE}	9.5	[79]
Rh-Se	Indophenol blue	175.6 ± 23.6 μg h^{-1} $mg_{cat.}^{-1}$ at −0.1 V_{RHE}	13.3 ± 0.4	[80]
AuHNCs	Indophenol blue	3.9 μg h^{-1} cm^{-2} at −0.5 V_{RHE}	30.2	[81]
Ag-Au	Nessler reagent	3.74 μg h^{-1} cm^{-2} at −0.4 V_{RHE}	35.9	[82]
Au-Ag-Pd-	^{1}H NMR Indophenol blue	5.8 μg $h^{-1}cm^{-2}$ at −0.3 V_{RHE}	48.9	[83]
Ag_2Au_1 NTs	Indophenol blue	21.7 μg h^{-1} $mg_{cat.}^{-1}$ at −0.3 V_{RHE}	3.8	[84]
Rh_2Sb RNR	Indophenol blue	228.85 ± 12.96 μg h^{-1} $mg_{cat.}^{-1}$ at −0.45 V_{RHE}	6.5	[85]
PdRu NRAs	Indophenol blue	34.2 μg h^{-1} $mg_{cat.}^{-1}$ at −0.2 V_{RHE}	2.4	[86]
$IrTe_4$ PNRs	Indophenol blue	51.1 μg h^{-1} mg_{cat}^{-1} at −0.2 V_{RHE}	15.3	[87]
RhCu	Indophenol blue	95.06 μg h^{-1} mg_{cat}^{-1} at −0.2 $_{VRHE}$	1.5	[88]
Au flowers	Indophenol blue	25.57 μg h^{-1} $_{mgcat.}^{-1}$ at −0.2 V_{RHE}	6.1	[89]
PdRu TPs	Indophenol blue	37.23 μg h^{-1} $mg_{cat.}^{-1}$ at −0.2 $_{VRHE}$	1.9	[90]
PdCuIr-LS	Indophenol blue	13.43 μg h^{-1} $mg_{cat.}^{-1}$ at −0.3 V_{RHE}	5.3	[91]
Ag_3Cu	Indophenol blue	24.59 μg h^{-1} $mg_{cat.}^{-1}$ at −0.5 V_{RHE}	13.3	[92]
np-Pd_3Cu_1	Nessler's reagent Indophenol blue	39.9 μg h^{-1} $mg_{cat.}^{-1}$ at −0.25 V_{RHE}	1.2	[93]
PdRu BPNs	Indophenol blue	25.92 μg h^{-1} $mg_{cat.}^{-1}$ at −0.1 V_{RHE}	1.5	[94]

PdRu	Indophenol blue	34.1 μg h^{-1} $mg_{cat.}^{-1}$ at −0.2 V_{RHE}	2.1	[95]
PdPb	Indophenol blue	25.68 μg h^{-1} $mg_{cat.}^{-1}$ at −0.05 V_{RHE}	5.8	[96]
Ag-Au	Indophenol blue	10 pmol s^{-1} cm^{-2} at −2.9 $V_{Ag/AgCl}$	18 ± 4	[97]
AuCu	Indophenol blue	63.9 μg h^{-1} $mg_{cat.}^{-1}$ at −0.2 V_{RHE}	0.5	[98]
Au NPG	Indophenol blue	22.0 ± 0.3 μg h^{-1} cm^{-2} at −0.6 V_{RHE}	44	[99]
Pt/Au@ZIF	Indophenol blue	161 μg h^{-1} $mg_{cat.}^{-1}$ at −2.9 $V_{Ag/AgCl}$	44	[100]
Au/M-BOP	Indophenol blue	75.89 μg h^{-1} mg_{cat}^{-1} at −0.2 V_{RHE}	10.4	[101]
Au NPs	Indophenol blue	0.36 μg h^{-1} m^{-2} at −0.2 V_{RHE}	22	[102]
Pt/NiO-NSs	Indophenol blue	20.59 μg h^{-1} $mg_{cat.}^{-1}$ at −0.2 V_{RHE}	15.6	[103]
Au film/NF	Indophenol blue	22.7 μg h^{-1} $mg_{cat.}^{-1}$ at −0.2 V_{RHE}	17.2	[104]

As shown in Table 1-1, many of the previous catalysts for the reduction of nitrogen to ammonia have not performed well. The ammonia yield rate and FE of existing related studies are extremely low. Most ammonia yield rate are in the nanomolar range (10^{-9} mol), and FE are generally below 50% and even below 1% in some cases. This results in a very low ammonia concentration in the product. And unfortunately, low concentrations of ammonia in solution are difficult to accurately measure experimentally.

The methods used to determine ammonia concentrations in the vast majority of studies are indophenol blue, Nessler's reagent and ion chromatography. Among them, indophenol blue method relies on the Berthelot reaction of phenol, hypochlorite and ammonia under alkaline conditions for determination. The blue indophenol product can be quantified and colorimetrically determined at a wavelength of approximately 640 nm. Citrate buffer is usually added to stabilize pH and prevent hydroxide precipitation, while sodium nitroprusside can be added to enhance the color reaction.

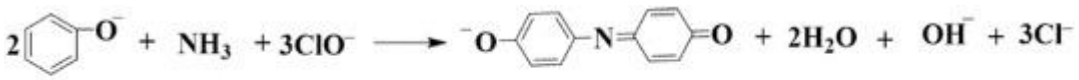

phenol indophenol (blue)

The Nessler method utilizes the colored compounds produced by the reaction of K_2HgI_4 and ammonia, and detects absorption spectra at a wavelength of about 400 nm.

$$NH_4^+ + 2[HgI_4]^{2-} + 4OH^- \rightarrow NH_2Hg_2OI + 7I^- + 3H_2O \quad (1\text{-}15)$$

Compared with the tedious Nessler method and indophenol blue method, the ion chromatography method is more convenient and efficient for the detection of NH_3. The ion chromatography method has high stability and sensitivity for separation of cationic species from columns packed with cation exchange material. Positive ions can be detected on a conductivity detector by comparing the retention time to that of a known standard sample. The NH_3 produced was then quantitatively analyzed by comparing the peak areas obtained with those of the standard samples.

However, the accuracy of these classical and practical NH_3 detection techniques is not ideal at low concentrations. Almost all test methods showed poor reproducibility at NH_3 concentrations below 0.2 ppm, and the results were extremely unreliable. At this concentration, the standard NH_3 solution changes by 0.1 ppm, the error of Nessler method is 20.5 %, and the error of ion chromatography method is 71.2 % [105]. In addition, trace amounts of nitrogen oxides and NH_3 in the air can interfere with the experimental results, resulting in false positive NH_3 [106]. Even lab-use nitrile gloves can cause severe NH_3 contamination. Accurate results from electrochemical nitrogen reduction of NH_3 can only be obtained when all ammonia contaminants are removed and nitrogen is the only possible source of NH_3 formation.

In conclusion, the method of reducing nitrogen to ammonia is feasible. However, there are some unavoidable problems. For example, extremely low ammonia yield rate and FE result in little practical potential and a lot of wasted electrical energy. Poor detection accuracy at low concentrations of ammonia leads to potential false positive ammonia.

1-2-2 Electrocatalytic reduction of nitrate to ammonia

With the rapid development of human society in recent centuries, there has been an imbalance in the global nitrogen cycle. Nitrate concentrations in surface and groundwater are rapidly rising due to the use of fertilizers, the burning of fossil fuels, and the discharge of industrial wastewater. In Europe in 2003, 80% of groundwater nitrate concentrations are greater than 25 mg-N/L in Spain, 50% in the UK, 36% in Germany, 34% in France and 32% in Italy [107]. In 2011, approximately 14.4% of groundwater in EU member states had nitrate concentrations above 50 mg-N/L [108]. In Japan, nitrate is found at the highest concentrations of 100 mg-N/L in water [109], which is equivalent to 10 times the limit for drinking water of the World Health Organization [110].

High concentrations of nitrate in water bodies pose potential risks to the environment and public health. It stimulates the growth of a large number of algae, thereby promoting the eutrophication of the water body. Livestock ingestion of nitrate-contaminated water can cause acute mortality [111]. Excess nitrate in drinking water has been linked to a variety of human diseases, such as colorectal cancer, bladder cancer, breast cancer risk, and thyroid disease [112]. For this reason many methods have been developed for the treatment of nitrate pollution, such as physical adsorption [113, 114], ion resin

exchange [115-117], reverse osmosis [118-120] and biological denitrification [121-123] and other commercial technologies[124]. Governments spend large sums of money each year to combat nitrate pollution, and then have little success. Nitrate pollution is on the rise around the world.

In order to solve the problem of nitrate pollution, generating economical ammonia is killing two birds with one stone. Similar to the nitrogen reduction reaction, the nitrate reduction reaction (NRR) is carried out under ambient conditions and does not require additional reducing agents or reagents. Some related researches have been carried out. Li developed strained ruthenium nanoclusters electrodes for electrocatalytic conversion of nitrate to ammonia. The Ru-based catalyst can achieve nearly 100 % ammonia FE (1 M KOH at -0.2 V_{RHE}) at a current density of 120 mA cm^{-2} by inhibiting the splitting of water to promote the participation of hydrogen radicals in the reaction [125]. Wang efficiently catalyzed ammonia synthesis via in situ generated Cu/Cu_2O (FE: 95.8 %, at -0.85 V_{RHE}). The electron transfer phenomenon at the catalyst surface promotes the formation of *NOH intermediate and suppresses the hydrogen evolution reaction (HER) [126]. Sargent tunes the nitrate adsorption capacity of the electrode to enhance NRR activity by alloying Cu and Ni. Among them, the $Cu_{50}Ni_{50}$ alloy (FE: 99 %, pH 14 at 0 V_{RHE}) obtained 6 times the catalytic activity of pure copper [127].

Table 1-2. Reported catalysts for the nitrate reduction to ammonia

Catalyst	NH_3 yield rate	FE (%)	Ref.
Ti	-	82	[128]
TiO_2	0.024 mmol $g_{cat.}^{-1}$ h^{-1}	66.3	[129]
TiO_{2-x}	0.045 mmol $g_{cat.}^{-1}$ h^{-1}	85	[129]
Cu-PTCDA	0.026 mmol h^{-1} cm^{-2}	85.9	[130]
$Cu_{50}Ni_{50}$	-	99	[127]
Cu/Cu_2O	0.245 mmol h^{-1} cm^{-2}	95.8	[126]
Strained Ru	5.56 mmol $g_{cat.}^{-1}$ h^{-1}	99.9	[125]

As shown in Table 1-2, the FE and ammonia yield rate of NRR is much higher than that of nitrogen reduction reaction. A thousand-fold increase in ammonia yield rate can be achieved while maintaining nearly 100% FE. More importantly, the concentration of ammonia solution obtained by NRR experiment is not low (dozens of ppm). This concentration of ammonia can be accurately measured by indophenol blue, Nessler's reagent and ion chromatography method.

The traditional Haber-Bosch process requires 4 kWh of energy to produce 1kg of ammonia [131]. However, the Strained Ru catalyst of NRR technology consumes about 22 kWh of electricity to produce 1 kg of ammonia. And the ammonia yield rate of 5.56 mmol $g_{cat.}^{-1}$ h^{-1} is already higher than the traditional Haber-Bosch process [125]. This means that electrocatalytic ammonia synthesis could be an attractive alternative to the traditional Haber-Bosch process.

1-3 Objectives of the study

Ammonia is an important resource to ensure the safety of food production. However, the traditional Haber-Bosch process to produce ammonia needs to consume a large amount of natural gas and emit a large amount of greenhouse gases. In the current era of carbon neutrality and skyrocketing natural gas prices, how to find a green, efficient and economical new ammonia production process has become a research hotspot. In recent decades, researchers all over the world have achieved a series of research results by electrocatalytic nitrogen reduction to ammonia. However, limited by the chemical inertness of nitrogen, low solubility and competition from HER, the obtained ammonia yield rate and FE are very poor, and it is still far from industrial application. In addition, low concentrations of ammonia (< 0.1 ppm) are difficult to accurately measure by traditional detection methods. All of these cast a shadow over the research on electrochemical reduction of nitrogen to ammonia.

Electrochemical reduction of nitrate to ammonia has been shown to be a feasible method. This method of converting nitrate pollutants to ammonia has environmental and economic benefits for human society. However, there is not much research on this at this stage. The current best Ru-based catalysts have achieved ammonia yields and energy consumption comparable to conventional Haber-Bosch processes. However, the high price of Ru metal limits its possibility of being applied on a large scale and replacing the traditional Haber-Bosch process in the future. Therefore, the purpose of this thesis is to find possible efficient and affordable catalysts for the electrochemical reduction of nitrate to ammonia.

1-4 Contents of this thesis

The Doctoral thesis consists of five Chapters.

Chapter 1, “General introduction” was written about background information on the uses and production of ammonia and potential alternatives to conventional ammonia production. And the purpose of this study is presented.

Chapter 2, “Exploring the mechanism of nitrate reduction to ammonia” The determinants of the reduction of nitrate to ammonia were studied by combining experiments and theoretical calculations.

Chapter 3, “The study of Cu-based and Cobalt-based catalysts for catalyzing the reduction of nitrate to ammonia” By studying the NRR selectivity on various metals and their compounds, it was confirmed that the electronic structure directly determines the NRR selectivity.

Chapter 4, “A porous Co_3O_4-carbon paper electrode enabling nearly 100% electrocatalytic nitrate reduction to ammonia”. The Co_3O_4 was electrodeopsited on carbon paper (CP) for high-efficient electrochemical nitrate-to-ammonia conversion. The Co_3O_4-CP electrode achieved a nearly 100% Faradaic efficiency over a wide potential range from -0.2 to -1.0 V_{RHE} in neutral pH and the highest NH_3 yield of 3.43 mmol h^{-1} cm^{-2} (2.25 mol g_{Co}^{-1} h^{-1}).

Chapter 5, “Conclusion and discussion” summarized all results obtained in this thesis and the most promising catalyst metals are discussed.

Chapter 2 Exploring the mechanism of nitrate reduction to ammonia

2-1 Introduction

The mechanism of a catalytic reaction refers to how a catalyst facilitates a chemical reaction. In a catalytic reaction, a catalyst lowers the activation energy of the reaction, thereby accelerating the rate of the chemical reaction. The catalyst interacts with the reactants, forming intermediates or transition states, and provides an alternative reaction pathway that allows the reaction to proceed at a faster rate. The mechanism of a catalytic reaction can be described through the following steps: 1. Adsorption of the reactants: The catalyst adsorbs reactant molecules, typically through physical or chemical adsorption. During the adsorption process, weak chemical or ionic bonds are formed between the catalyst and the reactants; 2. Activation of the reactants: The adsorbed reactant molecules undergo activation, where the chemical bonds of the adsorbed reactants begin to break or form. This activation process involves changes in the electronic structure and surface configuration of the catalyst; 3. Reaction: The activated reactant molecules undergo a chemical reaction on the catalyst surface. The catalyst provides a new reaction pathway, reducing the activation energy of the reaction. This can be achieved by adjusting the relative positions of the reactant molecules, providing an appropriate chemical environment, or altering the electron density, among other factors; 4. Desorption of the products: The reaction products dissociate from the catalyst surface and are released. The desorbed products can re-adsorb and interact with the catalyst through physical adsorption or undergo further chemical reactions, completing the catalytic cycle. The mechanism of a catalytic reaction can be complex, involving the formation and dissociation of various intermediates and transition states. Factors such as the type of catalyst, reaction conditions, and the nature of the reactants can all influence the mechanism of the catalytic reaction. By studying the mechanism of catalytic reactions, one can gain a better understanding of and optimize catalytic processes, improving reaction efficiency and selectivity. Therefore, in order to find potential excellent catalysts, we should start from exploring the mechanism first.

The Sabatier principle, also known as the Sabatier reaction or the Sabatier principle of catalysis, states that the most efficient catalytic activity for a given reaction occurs when the catalyst's electronic properties are close to those of the reactants. This principle is named after the French chemist Paul Sabatier, who was awarded the Nobel Prize in Chemistry in 1912 for his work on catalysis. According to the Sabatier principle, an optimal catalyst should neither bind too weakly nor too strongly with the reactants. If the catalyst binds too weakly, the reactants will not be sufficiently adsorbed and activated, resulting in a slow reaction rate. On the other hand, if the catalyst binds too strongly, the reactants may become strongly adsorbed and deactivated, preventing the reaction from occurring.

The principle suggests that the ideal catalyst should have electronic properties, such as electron density and reactivity, that are similar to those of the reactants. This similarity facilitates the adsorption of reactant molecules onto the catalyst's surface and the formation of appropriate reaction intermediates. It allows for efficient activation of the reactants and promotes the desired chemical transformations. The Sabatier principle has been widely used in the design and development of catalysts for various catalytic reactions, including hydrogenation and hydrogenolysis reactions. By understanding and applying this principle, researchers aim to identify and create catalysts that can provide optimal catalytic activity, selectivity, and efficiency for specific chemical transformations.

Therefore, according to the Sabatier principle, the mechanism that determines the rate of nitrate reduction to ammonia should be the bond strength between the catalyst and a certain kind intermediate. So, the next specific work will be the following three steps: 1. Find different intermediates 2. Obtain the corresponding bond strength 3. Compare the experimental results. Finally, the results are consistent with the experiments are the intermediates that determine NRR activity.

The electrochemical reduction of nitrate to ammonium requires 8 e^- and 10 H^+ to participate in the whole process. The adsorbed nitrate is reduced to nitrite in the rate-limiting step. Nitrite is the main by-product in alkaline or neutral environments. Then the nitrite is further reduced to nitric oxide when it is on the surface and undergoes a series of complicated processes to finally generate ammonia.

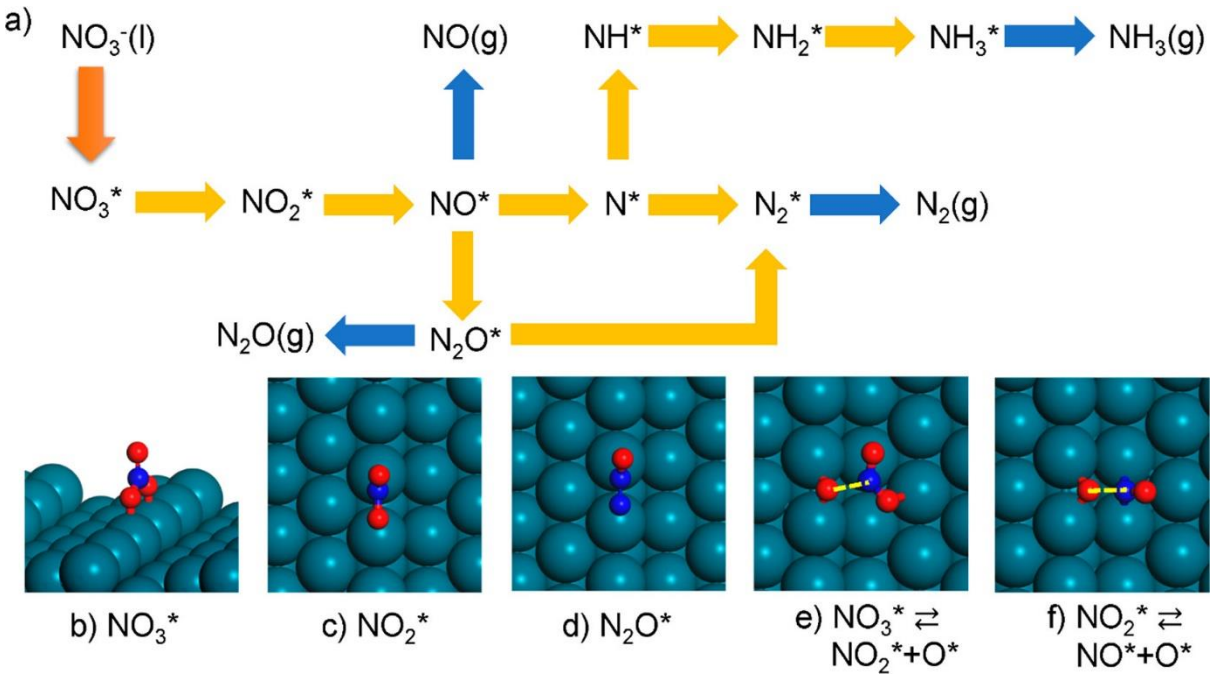

Fig.2-1The electrocatalytic nitrate reduction mechanism [132]

On the other hand, the HER competes with NRR for electrons and protons as the main side reaction in the solution. Various by-products and unavoidable side reactions make electrochemical NRR very complex (Fig.2-1). Therefore, an excellent NRR catalyst should have two characteristics of high

selectivity and low HER activity. So, we investigated their catalytic activity and selectivity trends by studying the nitrate reduction products (ammonia, nitrite, and hydrogen) on various metal (Ag, Fe, Ni, Co, Bi, Mo, Cu, Ti and Pt).

2-2 Methods

2-2-1 Materials and reagants

Platinum foil (99%), nickel sulfate hexahydrate ($NiSO_4 \cdot 6H_2O$), disodium molybdate dihydrate ($Na_2MoO_4 \cdot 2H_2O$), bismuth nitrate pentahydrate ($Bi(NO_3)_3 \cdot 5H_2O$),silver nitrate ($AgNO_3$), sodium hydroxide (NaOH), sodium sulfate (Na_2SO_4), potassium nitrate (KNO_3), cobalt sulfate ($CoSO_4 \cdot 7H_2O$), Ti, Fe and Cu plate, sodium hypochlorite (NaClO, available chlorine 4.00-4.99%), sodium nitroprusside ($C_5FeN_6Na_2O$), salicylic acid ($C_7H_6O_3$), ammonium chloride (NH_4Cl), and sodium citrate ($Na_3C_6H_5O_7$). All reagents involved in this experiment are of analytical grade without purification and provided by FUJIFILM Wako Pure Chemical Corporation, Japan. The nitrate solution required for this study was obtained by dissolving potassium nitrate in ultrapure water.

2-2-2 DFT Modeling

In density functional theory (DFT) calculations, the Projector Augmented Wave (PAW) method is a technique for dealing with pseudopotentials, which is used to approximately describe the interaction between the nucleus and the electrons outside the nucleus. interaction. This method is often used to calculate the electronic structure of solid materials, molecules and surfaces, etc.

In DFT calculations, in order to reduce the computational complexity, pseudopotentials are often used to replace the real nuclei-electron interactions. The pseudopotential separates the valence electrons into a local part and a nonlocal part, expands the nonlocal part with a plane wave, and replaces the local part with a pseudoatomic wave function. This can localize the strong interactions around the nucleus, thereby reducing the number of plane waves required for calculation and saving computing resources. However, the use of traditional pseudopotentials may cause some problems, such as losing part of the wave function information in the calculation, especially in critical regions such as chemical bond formation and breaking. To solve these problems, the projected enhanced wave method is introduced. Here, the PAW method is used to solve the problem of traditional pseudopotentials by introducing a set of projection functions (projectors) in the local area of each atom, and projecting the real electronic wave function onto this set of projection functions. This allows for more accurate nuclei-electron interactions and a better description of phenomena such as chemical bond formation and breaking. The projected enhanced wave method also retains the computational efficiency advantages of traditional pseudopotentials. The Perdew-Burke-Ernzerhof (PBE) functional is a widely used exchange-correlation functional in Density Functional Theory (DFT). In DFT, a functional is a function used to describe the

exchange and related energy of electrons, and then solve the ground state density and electronic structure of electrons. The PBE functional was proposed by John P. Perdew, Kieron Burke and Matthias Ernzerhof in 1996, and its full name is Perdew-Burke-Ernzerhof Generalized Gradient Approximation (PBE-GGA). This functional is based on the idea of Generalized Gradient Approximation (GGA), which considers electron exchange-correlation effects on the basis of density gradients. Compared with the earlier local density approximation (Local Density Approximation, LDA), GGA usually performs better in describing the interaction between atoms and molecular structure. PBE functionals are widely used in many fields, especially in the calculation of solid materials, molecular structures and surface reactions. Its advantages include relatively high computational efficiency and good accuracy, which can provide results that are consistent with experimental data. It should be pointed out that although the PBE functional performs well in many cases, it is not suitable for all systems and problems. For a specific system, a specific functional may perform better, so when choosing a suitable functional, it is necessary to comprehensively consider the calculation requirements and system characteristics. It is used here in the Vienna Ab initio Simulation Package (VASP), which can further improve the calculation accuracy. The use of spin-polarized density functional theory (Spin-polarized Density Functional Theory, spin-polarized DFT) is to deal with systems containing magnetic atoms or magnetic materials. Spin-polarized DFT is a variant of density functional theory (DFT) that allows the spins of electrons to have non-zero orientations in space, thereby enabling the description and consideration of magnetic properties in materials. In atoms and materials, electrons have spin, an intrinsic property of electrons that is similar to the electron's rotation around its core. The spin can be either up (+1/2) or down (-1/2). In nonmagnetic systems, it is usually assumed that the spin of electrons is uniformly distributed, that is, the density of electrons with upper spins is equal to the density of electrons with lower spins. The DFT in this case is called a non-spin-polarized DFT. However, in magnetic systems, there is a non-uniform distribution of spins. That is, the density of up-spin electrons is not equal to the density of down-spin electrons. This is due to the magnetic properties of the atoms or the presence of magnetic order or magnetic phase separation in the material, etc. To be able to describe these magnetic systems accurately requires the use of spin-polarized DFT. Spin-polarized DFT allows the spin orientation of electrons to vary in space, so the electron density of both spins can be considered simultaneously. Through spin-polarized DFT, the electron density distribution in different spin directions can be calculated, so as to obtain information such as the magnetic moment, magnetic properties and magnetic interaction of the material.

The cutoff energy of the plane wave basis is the energy cutoff used to expand the plane wave basis function in density functional theory calculations. In DFT calculation, the wave function is approximated by a plane wave, and the expansion of the plane wave requires a certain energy truncation to ensure the accuracy and convergence of the calculation results. A plane wave is a special wave function whose amplitude is uniform in space and does not vary significantly with position. In DFT calculations, plane waves are used to expand the electronic wave function and the periodic potential energy of

periodic crystals. The number and precision of the plane wave basis functions used in the calculation will affect the accuracy and convergence speed of the calculation results. The cutoff energy is an important parameter in the plane wave basis function, which is used to limit the energy range of the plane wave. The choice of cut-off energy should take into account the balance between the properties of the system and the computational efficiency. In general, higher cutoff energies give more accurate results, but also increase computational complexity and computation time. In practical applications, the choice of cut-off energy needs to find a suitable value by testing different cut-off energy values. If the cut-off energy is selected too low, it may cause the calculation results to fail to converge or produce large errors. If the cut-off energy is chosen too high, it will lead to increased computational cost without significant improvement in accuracy. In a word, the cutoff energy is an important parameter in the calculation of plane wave basis DFT. To obtain accurate and efficient calculation results, it is necessary to choose an appropriate cutoff energy reasonably. Here the cut-off energy of the plane wave base is 400 eV.

Monkhorst–Pack k-point sampling is a method used in the calculation of density functional theory to integrate the asymptotic wave function of Brilliant, especially in the calculation of the energy band structure and electronic density of states of periodic crystal systems. In periodic crystals, the electron wave function can be represented by the Bloch wave function, and calculating the integral of the Bloch wave function requires sampling the wave function in the reciprocal space (k-space). Since the inverted space is infinite, it is unrealistic to calculate every k point. In order to obtain sufficiently accurate results with limited computing resources, the Monkhorst–Pack k-point sampling method can be used. This method divides the reciprocal space into a finite grid and computes the integral of the Bloch wave function at each grid point. The selection of sampling points follows the suggestion of Monkhorst and Pack, and the accuracy of calculation can be adjusted by choosing different numbers of sampling points. In conventional calculations, the same number of sampling points are usually selected in each crystal direction, for example, n_x, n_y, n_z points are sampled in the three crystal directions of x, y, and z respectively, so that there are $n_x \times n_y \times n_z$ k-points are used for integration. The Monkhorst–Pack k-point sampling method can help to efficiently integrate the reciprocal space in DFT calculations, so as to obtain more accurate properties such as band structure and electronic density of states. Choosing an appropriate number of k-points is very important to balance computational accuracy and computational cost. All calculations here use 2 × 4 × 1. The vacuum thickness between the two layers is greater than 20 Å to avoid interactions between periodic images. During optimization, the energy and force converged to 10^{-4} eV/atom and 0.02 eV/Å, respectively. Thermal energy and zero point energy (ZPE) corrections are calculated from the G point.

Calculating the change in Gibbs free energy for each elementary step usually requires the use of statistical mechanics. The change in Gibbs free energy for each elementary step can be expressed as:

$$\Delta G = \Delta E + \Delta ZPE - T\Delta S$$

ΔE: ΔE is the total energy change of the system under elementary steps. In DFT, ΔE can be obtained by calculating the energy of the initial state and the final state. ΔZPE: The calculation of the zero-point vibrational energy usually involves calculating the vibrational modes and corresponding frequencies at each elementary step. By calculating the frequency of each mode, the change in zero-point vibrational energy ΔZPE can be obtained. ΔS: The calculation of the entropy change ΔS involves statistical mechanical calculations for the vibrational modes of each elementary step. T is temperature. This can be estimated by considering the Boltzmann distribution to estimate the entropy change under the elementary steps.

The zero-point energy and entropy of the NRR species are calculated from the vibrational frequencies, where only the adsorbate vibrational modes are calculated explicitly, while the catalyst sheet is fixed. The entropy and vibrational frequencies of gas phase molecules were taken from the National Institute of Standards and Technology (NIST) database.

The 19 elementary reactions involved in direct nitrate reduction were computed by DFT calculations and used as input for the microkinetic simulations. The 19 elementary steps are shown below:

$$NO_3^- + * \rightarrow NO_3^* + e^- \text{(2-1)}$$

$$NO_3^* + * \rightarrow NO_2^* + O^* \text{(2-2)}$$

$$NO_2^* + * \rightarrow NO^* + O^* \text{(2-3)}$$

$$NO^* + * \rightarrow N^* + O^* \text{(2-4)}$$

$$N^* + N^* \rightarrow N_2^* + * \text{(2-5)}$$

$$NO^* + NO^* \rightarrow N_2O^* + O^* \text{(2-6)}$$

$$N_2O^* + * \rightarrow N_2^* + O^* \text{(2-7)}$$

$$O^* + H^+ + e^- \rightarrow OH^* \text{(2-8)}$$

$$OH^* + H^+ + e^- \rightarrow H_2O^* \text{(2-9)}$$

$$H^+ + e^- + * \rightarrow H^* \text{(2-10)}$$

$$2H^* \rightarrow H_2 + 2* \text{(2-11)}$$

$$H_2O^* \rightarrow H_2O + * \text{(2-12)}$$

$$NO^* \rightarrow NO + * \text{(2-13)}$$

$$N_2^* \rightarrow N_2 + * \text{(2-14)}$$

$$N_2O^* \rightarrow N_2O + * \text{(2-15)}$$

$$N^* + H^+ + e^- \rightarrow NH^* \text{(2-16)}$$

$$NH^* + H^+ + e^- \rightarrow NH_2^* \quad (2\text{-}17)$$

$$NH_2^* + H^+ + e^- \rightarrow NH_3^* \quad (2\text{-}18)$$

$$NH_3^* \rightarrow NH_3 + * \quad (2\text{-}19)$$

Micro-dynamic calculation

The theoretical reaction rate has the following formulas to calculate:

$$k = Ae^{-\frac{Ea}{KbT}} \text{(2-20)}$$

where k is the rate constant in s^{-1} for the elementary step, The pre-exponential factor (A) contains information about the frequency of collisions between reactants and the randomness of the reactions. It is usually a dominant factor at lower temperatures because the activation energy contribution is smaller at lower temperatures. At high temperatures, the effect of activation energy is more pronounced. The specific value of the pre-exponential factor depends on the type of reaction and the system, and usually needs to be determined by experimental measurement or computational chemical simulation. It plays an important role in kinetic simulations and reaction rate predictions, especially for evaluating the rate constants of chemical reactions as a function of temperature, A was approximated as 10^{13} s^{-1} for all the elementary surface reactions. Ea is the activation energy, T is the temperature, and K_b is Boltzmann's constant. For inactive molecular adsorption (i.e., no significant energy barrier), the adsorption rate is determined by the rate at which gas-phase molecules hit the surface. Evaporation flux (the number of molecules evaporated per unit time per unit area) is related to the number density of gas phase molecules, gas temperature and surface properties. In the case of non-activated adsorption, the gas phase molecules are transferred from the gas phase to the solid surface at a relatively low pressure, at this time there are few collisions between the gas phase molecules, mainly free molecular motions. Therefore, the Hertz-Knudsen equation can be used to describe the rate of adsorption of non-activated molecules:

$$J = An\sqrt{2\pi mkt/h^2}$$

Where J is the number of molecules evaporated per unit time per unit area, also known as evaporation flux; A is the geometric area of the surface; n is the number density of gas molecules; m is the mass of the gas molecule; k is the Boltzmann constant; T is the temperature of the gas; h is Planck's constant. The Hertz-Knudsen equation applies to the evaporation of gas molecules from the surface of a liquid or solid at very low pressure, such as in a vacuum. Under this condition, there are few collisions between gas molecules, and the gas molecular motion is mainly free molecular motion. The Hertz-Knudsen equation does not hold for higher pressures and phase transitions between liquid or solid phases. The Hertz-Knudsen equation is an equation that describes the rate at which gas molecules evaporate. It was proposed independently by physicists Heinrich Hertz and Martin Knudsen in the late 19th and early 20th centuries, respectively. The Hertz-Knudsen equation expresses the relationship between the rate at which gas molecules evaporate from a liquid or solid surface and the nature, temperature, and surface properties of the gas. The equation is based on the principles of statistical mechanics and uses the concepts of the Boltzmann distribution and energy balance.

The molecular adsorption rate constant of species *i* was computed as:

$$k_{ads} = \frac{pA^*}{\sqrt{2\pi k_b T}} S \quad (2\text{-}21)$$

where p is the partial pressure of the adsorbate in the gas phase, A* the surface area of the adsorption site, m the mass of the adsorbate, and S the sticking coefficient, which we assume takes a value of unity for all adsorbates. Assumptions made about molecules in the activated state during the description of molecular desorption. The activation state means that the molecule needs to overcome the energy barrier during the desorption process, that is, the molecule must be in a high-energy state before desorption, and this high-energy state is the activation state. Specifically, the molecule has three rotational degrees of freedom and two translational degrees of freedom. In the active state of the molecule, due to the higher energy, the molecule can rotate (rotational degree of freedom) and move on the surface (translational degree of freedom). The presence of these degrees of freedom affects the energy distribution and dynamic behavior of the molecule. For the theoretical study of molecular desorption, the behavior of molecules in different energy states is usually considered, that is, for different combinations of rotational and translational degrees of freedom, to simulate the energy surface of the activated state. Doing so provides a better understanding of the kinetic behavior of the desorption process, such as the rate of desorption. Accordingly, the rate constant of desorption for adsorbate *i* was calculated as:

$$k_{des} = \frac{k_b T^3}{h^3} \frac{A^* 2 k_b \pi}{\sigma \theta_{rot}} e^{-\frac{E_{des}}{KbT}} \quad (2\text{-}22)$$

where E_{des} is the desorption energy, h is Planck's constant, and σ and θ_{rot} are the symmetry number and the characteristic temperature for rotation, respectively.

The nitrate reduction rate was calculated by the MKMCXX microkinetic modeling software suite for heterogeneous catalysis. In our simulations, the molar ratio of NO_3^- and H^+ in the solution was 1:1 at a reaction temperature of 300 K, which is close to typical experimental reaction conditions. For each of the M components in the kinetic network, a single differential equation for each elementary reaction step was written in the form of:

$$r_i = k_i \prod_{w=1}^{M} c_w^v \quad (2\text{-}23)$$

where ki is the rate constant and c_w and v are the concentration and stoichiometric coefficient of species w in elementary reaction step i. Steady-state coverages were computed by integrating the ordinary differential equations in time until changes in the surface coverages were small ($< 10^{-12}$). Rates of the individual elementary steps were obtained based on the computed steady-state surface coverages. The elementary steps that control the rate of the overall reaction were determined using degree of rate control (DRC) analysis [132].

2-2-3 Electrode preparation

The Cu, Fe and Ti electrode: Cut high-purity Cu, Fe and Ti plate into 12*25 mm (effective area was 12*20mm) to obtain Cu, Fe and Ti electrode.

The Pt electrode: Pt sheet with the size of 1 cm^2 was used as Pt electrode.

The Ag electrode: Ag electrode use Cu plate as the base material. The Cu plates were washed with alcohol and ultrapure water to remove surface impurities. The copper plates were then electropolished with 4 V in 85% phosphoric acid for 2 minutes to remove surface oxides. The obtained Cu plate was reacted with 0.1 M $AgNO_3$ solution to obtain Ag electrode (effective area was 12*20mm).

$$Cu + 2Ag^{+} = Cu^{2+} + 2Ag \quad (2\text{-}24)$$

The Co electrode: Co electrode was prepared by electrodeposition. The obtained Cu plates was then used as a conductive substrate and applied in a 0.1M $CoSO_4$ solution at -2.0 $V_{Ag/AgCl}$ for a period of time. Then, after cleaning with ultrapure water, place it in a furnace at 50°C and dry it to obtain the Co electrode (effective area was 12*20mm).

The Bi electrode: Bi electrode was prepared by electrodeposition. The obtained Cu plates was then used as a conductive substrate and applied in a 0.1M $Bi(NO_3)_3$ solution at -2.0 $V_{Ag/AgCl}$ for a period of time. Then, after cleaning with ultrapure water, place it in a furnace at 50°C and dry it to obtain the Bi electrode (effective area was 12*20mm).

The Mo electrode: Mo electrode was prepared by electrodeposition. The obtained Cu plates was then used as a conductive substrate and applied in a 0.1M Na_2MoO_4 solution at -2.0 $V_{Ag/AgCl}$ for a period of time. Then, after cleaning with ultrapure water, place it in a furnace at 50°C and dry it to obtain the Mo electrode (effective area was 12*20mm).

The Ni electrode: Ni electrode was prepared by electrodeposition. The obtained Cu plates was then used as a conductive substrate and applied in a 0.1M $NiSO_4$ solution at -2.0 $V_{Ag/AgCl}$ for a period of time. Then, after cleaning with ultrapure water, place it in a furnace at 50°C and dry it to obtain the Ni electrode (effective area was 12*20mm).

2-2-4 Electrochemical testing

All electrochemical tests were performed by Potentiostat/Galvanostat HAB-151A (HOKUTO DENKO Corp., Japan) in a three-electrode system at room temperature. The prepared were used as the working electrode, Pt wire was used as the counter electrode and Ag/AgCl (filled with saturated KCl) (013691 RE-1CP, ALS Co., Ltd, Japan) was used as the reference electrode to form a three-electrode system. A 100ml H-type cell was used to study the reduction of nitrate to ammonia. Convert the potential $V_{Ag/AgCl}$ to a reversible hydrogen electrode (V_{RHE}) using the following equation, where $V_{Ag/AgCl}$ *vs.* $^{0}{}_{NHE}$ is 196 mV at 25°C.

$$V_{RHE} = V_{Ag/AgCl} + V_{Ag/AgCl}\ vs.0_{NHE} + 0.059 * pH \text{ (2-25)}$$

A proton exchange membrane (PEM Nafion 211) was used to separate the two chambers. A portion of the solution was taken out for product analysis at regular intervals. 40ml of reaction solution was added to the cathode cell and anode cell, which contained 0.1M sodium sulfate as supporting electrolyte and a certain concentration of potassium nitrate. The resulting reaction solution was diluted ten times and used to identify the product.

2-2-5 Production detection and efficiency calculations

The classical indophenol blue method is used for the identification of ammonia. Dilute the reacted solution in different amounts to ensure that the ammonia concentration in the test solution is within the linear range of this identification method. The identification solution consists of three parts, salicylic acid solution, sodium hypochlorite solution and sodium nitroprusside solution. The salicylic acid solution was obtained by adding 4.4 g of sodium hydroxide, 10 g of salicylic acid and 10 g of sodium citrate to 200 ml of water. Sodium hypochlorite solution was obtained by adding 8 ml sodium hypochlorite (available chlorine 4.00-4.99%) and 1.2 g sodium hydroxide to 40 ml with water. Sodium nitroprusside solution was obtained by adding 0.4 g sodium nitroprusside to 40ml with water. The solution to be identified was mixed with 0.1 ml sodium hypochlorite solution, 0.1 ml sodium nitroprusside solution and 0.5 ml salicylic acid solution, and the volume was adjusted to 10 ml, and the color reaction was at least one hour to ensure that the reaction is complete. The absorption wavelength of ammonia was 697 nm.

The Faradaic efficiency (FE) of ammonia was calculated according to the following equation:

$$\text{FE} = \frac{\text{nZF}}{Q} \text{ (2-26)}$$

Where n is the moles of ammonia generated; Z is the number of electron transfers towards the formation of 1 mol of ammonia which is 8; F is the Faraday constant (96485 C·mol^{-1}); Q is the total current.

The yield rate of NH_3 was calculated using the following equation:

$$\text{NH}_3 \text{ yield rate} = \frac{\text{n}_{NH_3}}{S \times t} \text{ (2-27)}$$

Where S is the area of electrode (2.4 cm^2); t is the reaction time (1 hour).

The selectivity of NH_3 was acquired by the following equation:

$$\text{Selectivity} = \frac{C_{NH_3}}{\Delta C_{NO_3^-}} \text{ (2-28)}$$

Where $\Delta C_{NO_3^-}$ is the concentration difference of nitrate before and after the reaction.

The detection of nitrate and nitrite is analyzed by ion chromatography (metrohm 881 compact IC pro).

The absorbance measurements were performed on Thermo Fisher Varioskan LUX at 697 nm. The obtained calibration curve (Fig. 2-2) was used to calculate the NH_3 concentration.

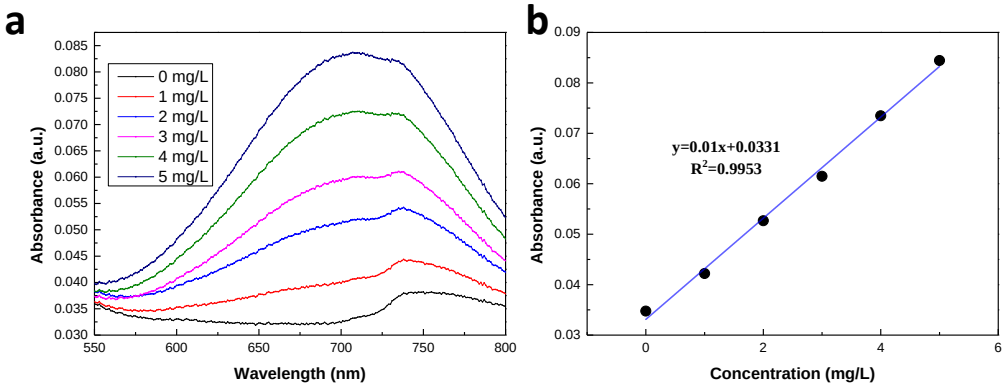

Fig.2-2 (a) the UV-Vis absorption of various NH_3 concentrations. (b) The calibration curve used for calculation of NH_3 concentration.

2-3 DFT results

2-3-1 Nitrate (NO_3^-) and nitrite (NO_2^-) adsorption energy

The most pressing problem facing quantifying the theory of heterogeneous catalysis is to identify suitable quantities or "descriptors" to represent the "bond strengths" of interest to deduce possible mechanisms. Previous studies often used descriptors such as the heat of formation of metal oxides or suitable compounds, or the number of d-orbital electrons. However, until recent advances in computational chemistry, none of these efforts fit well with experimental data. In the conventional HB process for ammonia synthesis, an example of using the heat of oxide formation to describe the activity of ammonia synthesis is shown in the Fig. 2-3a. This kind of descriptor cannot explain the experimental data very well. The volcano plot was greatly improved when the descriptor was changed to the actual nitrogen adsorption energy on the relevant metal surface as a descriptor (see Fig. 2-3b). Here, the same experimental rates are plotted against nitrogen adsorption energies determined from density functional theory (DFT) calculations. This suggests that the adsorption energy of nitrogen on the metal surface better quantitatively describes the Sabatier's principle concept of " bond strengths" than the heat of oxide formation.

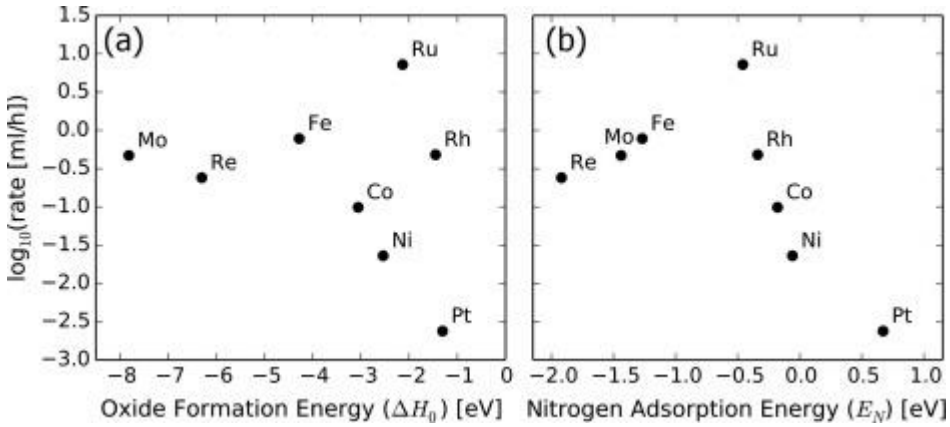

Fig. 2-3 (a) Volcano plot for the ammonia synthesis reaction over K-promoted transition-metal catalysts at 523 K and 0.8 bar using oxide heat of formation as a bond strength descriptor. (b) Volcano plot of the same rates with the nitrogen adsorption energy at stepped metal surfaces as determined by DFT calculations using the RPBE functional as a descriptor. [10]

It can be seen that the first task of exploring the mechanism of nitrate reduction to ammonia should be to clarify the descriptor.

As shown in Fig.2-4, there are two different trends in the adsorption energies of nitrate and nitrite intermediates on various metals. Based on nitrate, the best NRR activity should be obtained by Co, and the worst by Ag. If based on nitrite, the best should be Cu and the worst should be Co. The difference between the two is very obvious. Therefore, it should be easy to obtain the correct result after comparing with the experimental phenomenon.

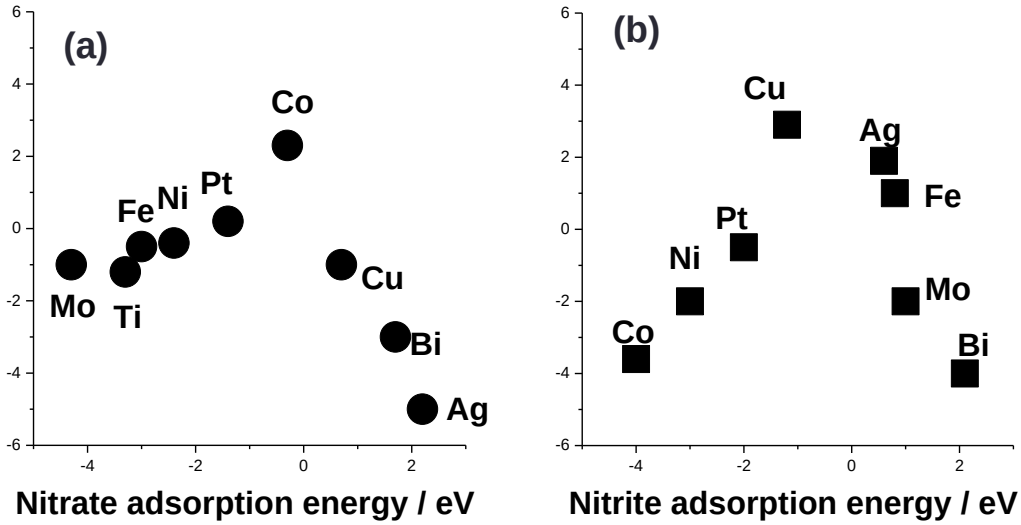

Fig. 2-4. Adsorption energies of different intermediates on various metals (a) Nitrate (b) Nitrite

2-3-1 Hydrogen (H^+) adsorption energy

On the other hand, while catalyzing NRR in aqueous solution, the hydrogen evolution reaction (HER) is also inevitable. The strength of HER as a side reaction will directly affect the activity of NRR. Therefore, we also calculated the HER activity of various metal surfaces using the DFT method as shown in Fig. 2-5. As consistent with the results of many previous studies, metal Pt has excellent HER activity far stronger than other metals. Metallic silver has the worst HER activity among these metals due to too weak adsorption energy.

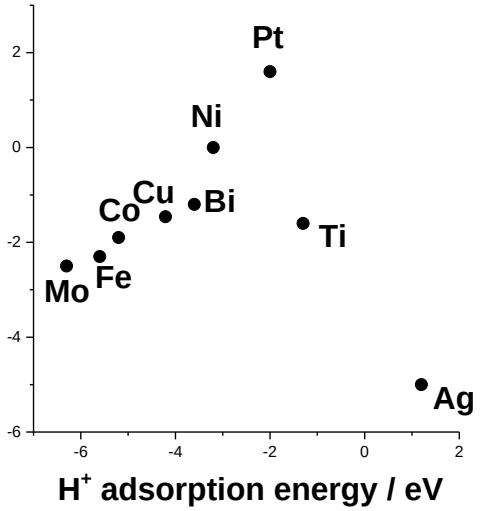

Fig. 2-5. Hydrogen (H^+) adsorption energy on various metals

2-4 Experimental results

Two completely different sets of predictions can be obtained through the previous DFT calculations, one with nitrate adsorption energy as the descriptor and the other with nitrite. In order to verify the DFT calculation results, various metal catalysts (Ag, Fe, Ni, Co, Cu, Bi, Mo, Ti and Pt) were investigated in 0.1 M Na_2SO_4+0.1M KNO_3 solution. The NRR activity of these metals was tested at different potentials.

2-3-1 The NRR catalytic performance on various metals

The NRR catalytic activities of these nine different metals are shown in the Fig.2-6. Impressively, Co element achieved the best NRR activity (> 90% NH_3 FE and nearly 100 % NH_3 selectivity) among the nine elements. Cu, as the best element for nitrite adsorption energy prediction, obtained far worse results than Co (Fig.2-6d and f). Through this difference, the adsorption energy of nitrate can be identified as a descriptor of NRR. Therefore, we can confirm that it is the nitrate adsorption energy that determines the NRR reaction rate.

The unfavorable NRR activity of molybdenum is due to its strong nitrate adsorption energy. At this point DFT predictions can successfully explain the poor NRR activity of molybdenum (Fig.2-6a). Ru metal has achieved excellent catalytic performance, close to 100% NH_3 FE and high NH_3 yield rate. Both platinum and ruthenium are platinum group metal elements. They have similar physical and chemical properties and tend to occur together in the same mineral deposits. Therefore, here we tested the NRR performance of platinum with close physical and chemical properties. As shown in Fig.2-6b, the HER activity of platinum is excellent. Almost all of the electrical energy is consumed producing hydrogen instead of ammonia. The obtained ammonia and nitrite by-products were all below the detection limit, so there is no selectivity data for NH_3 in this experiment. Bismuth is considered to be an excellent catalyst in the related research of electrochemical reduction of nitrogen to ammonia. Due to the moderate adsorption of iron to nitrogen, iron was selected as the catalyst for the traditional Haber-Bosch process. Although the reaction environment, driving force, and reaction mechanism of the electrochemical catalyzed nitrate reduction to ammonia are completely different from those of the traditional Haber-Bosch process, we still chose to test the NRR activity of iron. As shown in the Fig. 2-6c, due to the weakness of the nitrite formation of FE at high potential, the optimal NH_3 FE and selectivity can reach 76.1 % and 62.5 % at -1.0 V_{RHE}, respectively. Then, the Ti electrode was used for NRR test. According to the previous research, the NH_3 FE of titanium metal can obtain more than 66%. Here we did a similar experiment. The results show the NH_3 FE of is only 22.7 %, the nitrite formation FE is greatly suppressed under high potential conditions, so a rather high NH_3 selectivity of 80.1 % can be obtained at -1.0V_{RHE} (Fig. 2-6e). The significantly stronger HER activity limits the NRR activity of Ti. The silver is often regarded as a poor catalyst for HER due to its low hydrogen adsorption free energy and low current density [133]. Here, silver electrodes were used to test the NRR performance. The nitrite formation FE of Ag electrode is very high (almost 100%), which leads to the NH_3 FE being almost 0 at low potential conditions as shown in Fig. 2-6g (from -0.2 V_{RHE} to -0.4 V_{RHE}). As the potential increases, the nitrite formation of FE decreased gradually while the NH_3 FE and selectivity started to increase from nearly 0. Overall, the NH_3 FE and selectivity of the Ag electrode are unsatisfactory (NH_3 FE: 45.2 %, NH_3 selectivity: 18.2 % at -1.0 V_{RHE}) due to the strong preference for nitrite generation. The atomic number of Bi in the periodic table is 83. Unlike the poisonous neighbor elements No. 82 lead and No. 84 polonium, Bi is a non-toxic heavy metal element. Bulk metal Bi is a semimetal with direct plasmonic effect. Due to its advantages such as long Fermi wavelength, high carrier mobility, and surface plasmon resonance (SPR) effect, it has attracted extensive research interest, especially in the fields of photocatalysis and electrocatalysis. Due to Bi's quantum confinement and low energy overlap, it can transform from a semimetal to a semiconductor when it becomes a thin film. Recently, researchers found that metallic Bi can be used for electrocatalytic reduction of ammonia synthesis. Semiconducting Bi is less reactive in HER due to the high adsorption free energy barrier between Bi and H_2. [6] However, the Bi element is limited by too strong nitrate adsorption energy in the test, resulting in low NRR activity (Fig.2-6i).

Overall, the DFT calculations for most elements agree well with the experimental data. Only two elements, platinum and nickel (Fig.2-6b and h), are considered to be excellent NRR catalysts in DFT predictions, yet experimental data show that their activities are poor.

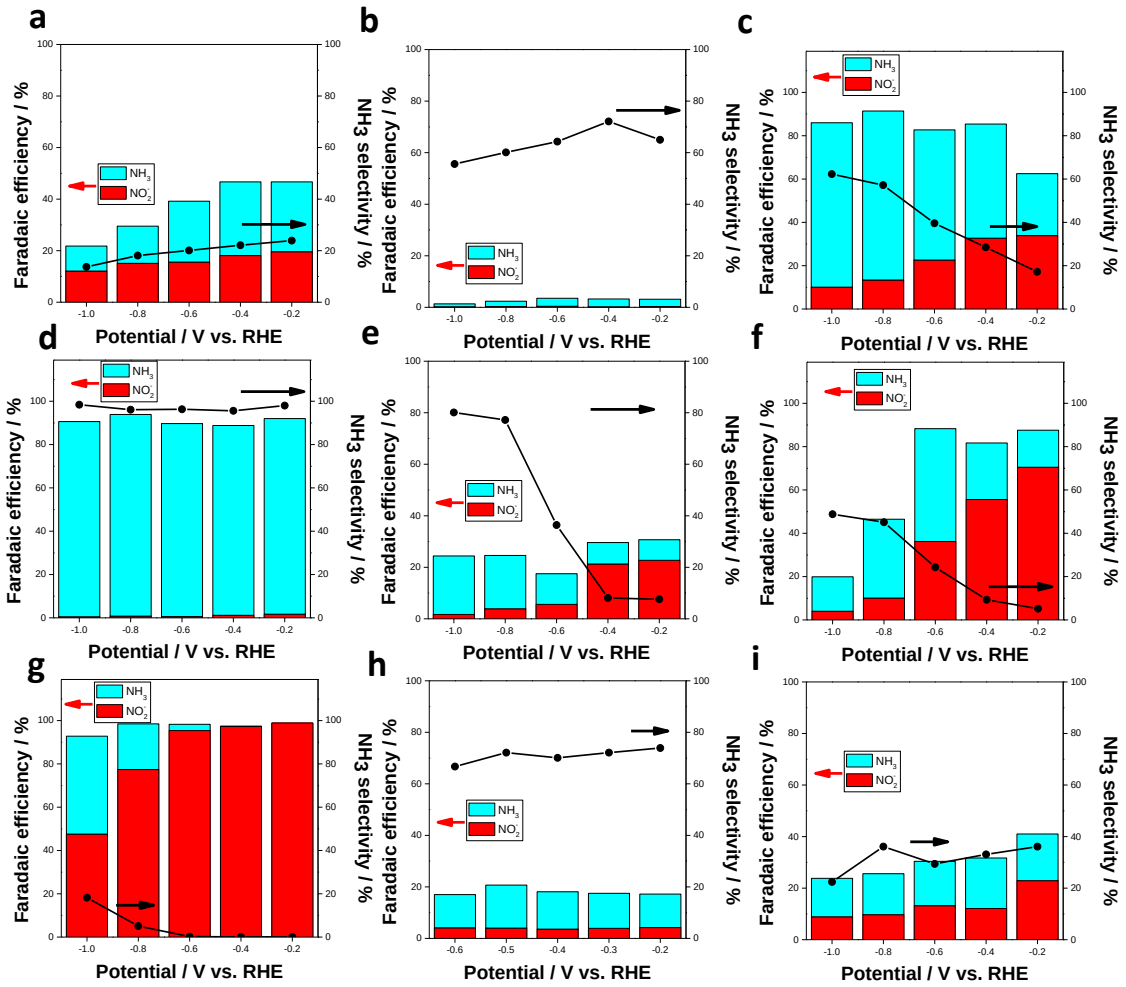

Fig.2-6 Ammonia, nitrite FE and ammonia selectivity on various metals (a) Mo, (b) Pt, (c) Fe, (d) Co, (e) Ti, (f) Cu, (g) Ag, (h) Ni and (i) Bi at a given potentials.

2-3-2 The influence of HER

In the above studies we only considered the NRR in the whole catalytic reaction. The resulting DFT prediction results cannot explain the experimental results very well. From this, we measured HER activity on various metals. Specifically, the amount of species lost to nitrogen (N_{loss}) in the reaction is first obtained through material conservation.

$$\Delta m_{NO_3^-} = m_{N_{loss}} + m_{NO_2^-} + m_{NH_3} \quad (2\text{-}29)$$

The $\Delta m_{NO_3^-}$ is the amount of substance changed by nitrate. The $m_{NO_2^-}$ is the amount of substances that generate nitrite in the catalytic experiment. Both are directly measured by ion chromatography. The m_{NH_3} is the amount of ammonia substance obtained by the reaction, measured by spectrophotometry. The $m_{N_{loss}}$ can be obtained by the above formula. The energy ($E_{N_{loss}}$) required to generate it can then be calculated. The energy consumed to generate hydrogen (E_{H_2}) can then be calculated by energy conservation.

$$E_{total} = E_{N_{loss}} + E_{H_2} + E_{NO_2^-} + E_{NH_3} \quad (2\text{-}30)$$

The E_{total} is the overall power consumption, which is directly recorded by the Potentiostat/Galvanostat HAB-151A (HOKUTO DENKO Corp., Japan) instrument. The $E_{NO_2^-}$ and E_{NH_3} are the computers consumed to generate the corresponding amount of nitrite and ammonia respectively, which are calculated by Faraday's law.

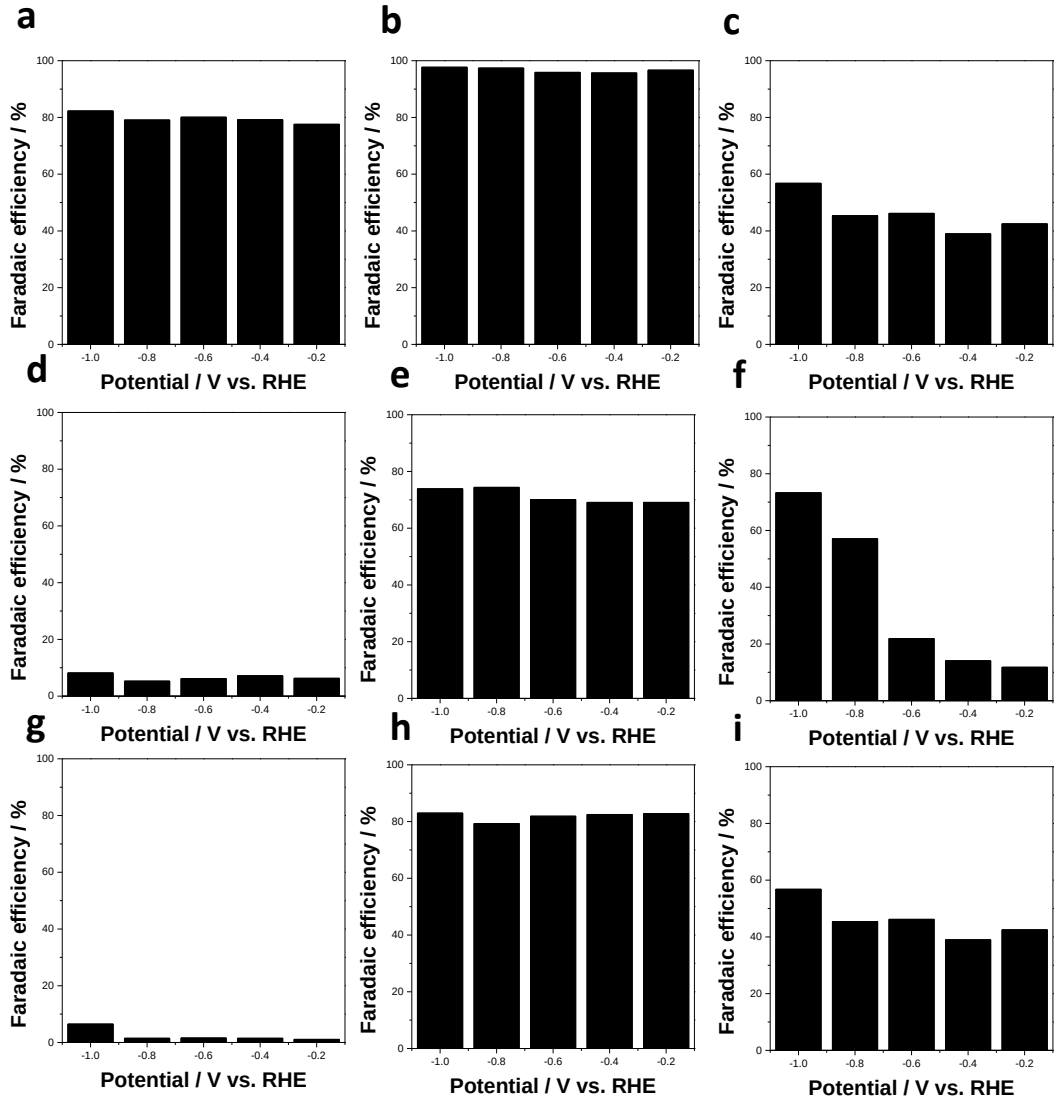

Fig.2-7 The H_2 FE on various metals (a) Mo, (b) Pt, (c) Fe, (d) Co, (e) Ti, (f) Cu, (g) Ag, (h) Ni and (i) Bi at a given potentials.

As shown in Fig.2-7b and h, the HER activity of platinum and nickel is quite strong. Almost 100% of the energy at the platinum electrode is used to generate hydrogen instead of catalytically reducing nitrate to ammonia. This is consistent with the previous findings, most researchers believe that platinum is the best HER catalyst due to the moderate hydrogen (H^+) adsorption energy. Although Ni and Pt have excellent NRR activities, they are also excellent HER catalysts. Therefore, a reasonable explanation is that, There is competition for HER and NRR on Ni and Pt. Under our experimental conditions, HER dominated the system. This shows that to correctly evaluate the ammonia synthesis activity of metals, both NRR and HER need to be considered. The poor HER activity of cobalt and copper may indirectly contribute to the occurrence of NRR.

2-5 Conclusions

The same experiments and DFT calculations confirmed that it is the nitrate (NO_3^-) adsorption energy that determines the NRR activity. After systematically studying nine different metals, cobalt and copper are considered as potential excellent NRR catalysts due to moderate nitrate adsorption energy and poor HER activity. An excellent NRR catalyst needs both moderate nitrate adsorption energy and poor HER activity, both of which are indispensable.

Chapter 3 The study of copper-based and cobalt-based catalysts for catalyzing the reduction of nitrate to ammonia.

3-1 Introduction

Since the dissociation energy (204 kJ/mol) of the O=N bond of nitrate is much lower than that of the triple bond of nitrogen (941 kJ/mol), the NRR reaction has better kinetics. Another advantage of using nitrate as a feedstock is its abundance in nature, especially in groundwater. Therefore, the use of nitrate to produce ammonia in large quantities under ambient conditions not only has the potential to reduce energy consumption, but also helps to solve the problem of environmental pollution. However, the conversion of nitrate to ammonia is an eight-electron transfer.

$NO_3^- + 8e^- + 9H^+ \rightarrow NH_3 + 3H_2O$ (3-1)

The actual potential of this process is very close to the potential of HER (0 V_{RHE}), which will inevitably generate hydrogen gas, resulting in the decline of FE. Therefore, inhibiting the competitive HER may be the key to improve the catalytic activity of the catalyst.

Influenced by this, Co- and Cu-based catalysts were developed and demonstrated to have excellent catalytic activities. However, the high price of Ru greatly limits its potential application value in NRR. Here we follow previous research on Cu-based NRR to develop efficient and affordable NRR catalysts.

3-2 Methods

3-2-1 Materials and reagants

The high-purity Cu plate is provided by Shingo Shoten, Japan. Thiourea (CH_4N_2S), Sodium sulfate (Na_2SO_4•$5H_2O$), Potassium nitrate (KNO_3), Phosphoric acid (85% H_3PO_4), cobalt sulfate ($CoSO_4 \cdot 7H_2O$), Ti plate, sodium hypochlorite (NaClO, available chlorine 4.00-4.99%), sodium nitroprusside ($C_5FeN_6Na_2O$), salicylic acid ($C_7H_6O_3$), Ammonium chloride (NH_4Cl), sodium hydroxide (NaOH) and sodium citrate ($Na_3C_6H_5O_7$). All reagents involved in this experiment are of analytical grade and provided by FUJIFILM Wako Pure Chemical Corporation, Japan. The nitrate solution required for this study was obtained by dissolving potassium nitrate in ultrapure water. The pH value of the solution is adjusted by dilute sulfuric acid and sodium hydroxide solution.

3-2-2 Electrode preparation

The high-purity copper plates were cut into a size of 12*25*0.5 mm (effective area is 12*20 mm). The copper plates were washed with alcohol and ultrapure water to remove surface impurities. The copper plates were then electropolished with 4 V in 85% phosphoric acid for 3 minutes to remove surface oxides. The obtained copper plates were recorded as pure Cu electrodes.

The Cu_2O and CuO electrodes are obtained by heating pure copper electrodes in air. Copper was oxidized by oxygen in air to Cu_2O at 250°C. When the oxidation temperature was further increased to 350 °C, the copper was completely converted to CuO [134].

Finally, Cu_2S and CuS are prepared by substitution reaction on the basis of Cu_2O and CuO. The Cu_2O and CuO reacted with 0.1M thiourea solution in a water bath at 90°C for 2 h (Fig.3-1). The K_{sp} of Cu_2S (2.5×10^{-48}, 25 °C) and CuS (8.0×10^{-37}, 25 °C) are much lower than those of Cu_2O (2.0×10^{-15}, 25 °C) and CuO (1.0×10^{-20}, 25 °C), so this transition from oxide to sulfide can occur through an anion exchange reaction between O^{2-} and S^{2-} anions, which is thermodynamically favorable [135]. The effective geometric area of the obtained electrodes was 12*20 mm.

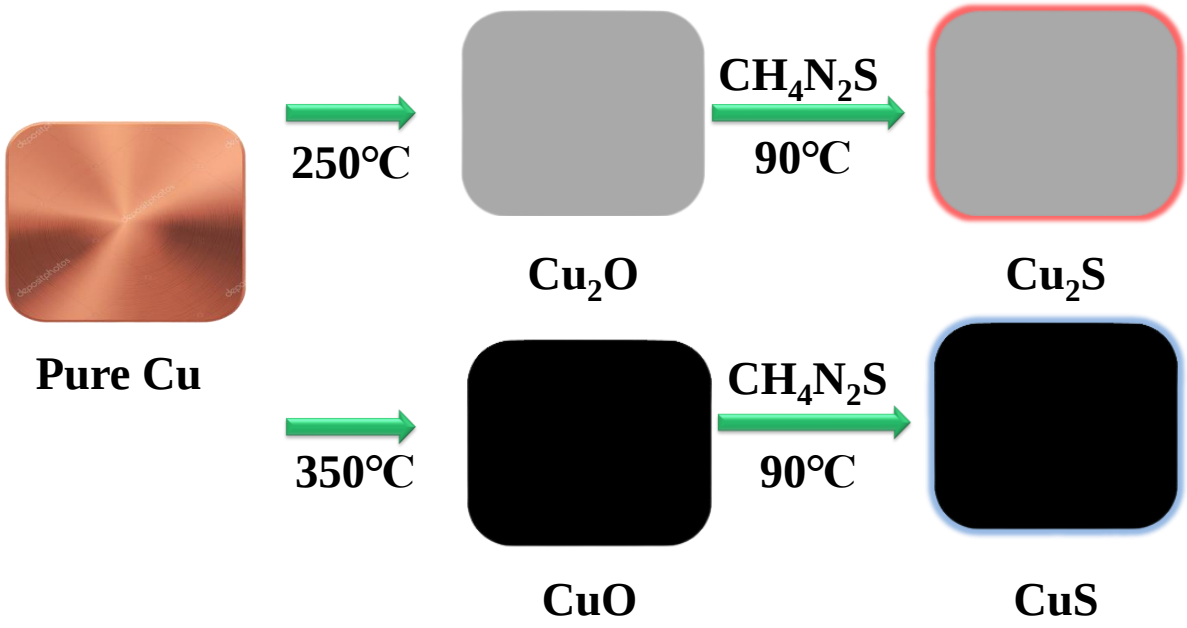

Fig.3-1 Schematic diagram of the processing route of the Cu-based catalyst

The Ti plate was cut into a size of 12×25 mm (effective area is 12×20 mm). The obtained Ti plate was washed with alcohol and ultrapure water to remove surface impurities.

The Co electrode: First of all, dissolve 1.124 g $CoSO_4\cdot7H_2O$ in 100 mL ultrapure water, then add 0.01 g sodium dodecyl sulfate and stirred vigorously for 10 minutes to obtain cobalt solution. The obtained Ti plate was then used as a conductive substrate and applied in a cobalt solution at -2.0 $V_{Ag/AgCl}$ for a period of time. The electrode was then rinsed with alcohol and ultrapure water, dried in an oven at 50 °C. The mass change before and after the Ti plate was calculated to obtain the Co mass loading.

Here, the obtained electrode was referred to as a Co electrode. The color of the Co electrode was silver-white.

The CoO electrode: The Co electrode was heated at 300°C for 2 hours. Part of Co was oxidized to CoO and Co_3O_4 by oxygen at high temperature. The composition of this electrode consists of most of CoO and a small amount of Co_3O_4, so it is referred to as a CoO electrode. The color of CoO electrode was green-black.

The Co_3O_4 electrode: The CoO electrode was put into dilute sodium hypochlorite solution and treated for a period of time. During this process, another part of CoO or $Co(OH)_2$ was oxidized to Co_3O_4 by sodium hypochlorite. The color of Co_3O_4 electrode was black.

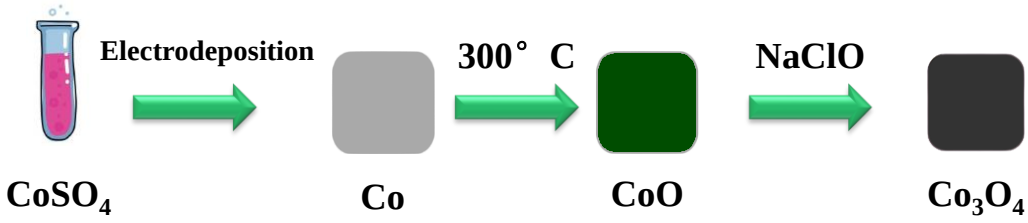

Fig.3-2 Schematic diagram of the processing route of the Co-based catalyst

3-2-3 Electrochemical testing

All electrochemical tests were performed by Potentiostat/Galvanostat HAB-151A (HOKUTO DENKO Corp., Japan) in a three-electrode system at room temperature. The prepared were used as the working electrode, Pt wire was used as the counter electrode and Ag/AgCl (filled with saturated KCl) (013691 RE-1CP, ALS Co., Ltd, Japan) was used as the reference electrode to form a three-electrode system. A 100ml H-type cell was used to study the reduction of nitrate to ammonia. Convert the potential $V_{Ag/AgCl}$ to a reversible hydrogen electrode (V_{RHE}) using the following equation, where $V_{Ag/AgCl}$ *vs.* $^0{}_{NHE}$ is 196 mV at 25°C.

$$V_{RHE} = V_{Ag/AgCl} + V_{Ag/AgCl}\ vs.\ 0_{NHE} + 0.059 * pH \quad (3\text{-}2)$$

A proton exchange membrane (PEM Nafion 211) was used to separate the two chambers. A portion of the solution was taken out for product analysis at regular intervals. 40ml of reaction solution was added to the cathode cell and anode cell, which contained 0.1M sodium sulfate as supporting electrolyte and a certain concentration of potassium nitrate. The resulting reaction solution was diluted ten times and used to identify the product.

3-2-4 Production detection and efficiency calculations

The classical indophenol blue method is used for the identification of ammonia. Dilute the reacted solution in different amounts to ensure that the ammonia concentration in the test solution is within the linear range of this identification method. The identification solution consists of three parts, salicylic

acid solution, sodium hypochlorite solution and sodium nitroprusside solution. The salicylic acid solution was obtained by adding 4.4 g of sodium hydroxide, 10 g of salicylic acid and 10 g of sodium citrate to 200 ml of water. Sodium hypochlorite solution was obtained by adding 8 ml sodium hypochlorite (available chlorine 4.00-4.99%) and 1.2 g sodium hydroxide to 40 ml with water. Sodium nitroprusside solution was obtained by adding 0.4 g sodium nitroprusside to 40ml with water. The solution to be identified was mixed with 0.1 ml sodium hypochlorite solution, 0.1 ml sodium nitroprusside solution and 0.5 ml salicylic acid solution, and the volume was adjusted to 10 ml, and the color reaction was at least one hour to ensure that the reaction is complete. The absorption wavelength of ammonia was 697 nm.

The Faradaic efficiency (FE) of ammonia was calculated according to the following equation:

$$\mathrm{FE} = \frac{\mathrm{nZF}}{Q} \quad (3\text{-}3)$$

Where n is the moles of ammonia generated; Z is the number of electron transfers towards the formation of 1 mol of ammonia which is 8; F is the Faraday constant (96485 $C \cdot mol^{-1}$); Q is the total current.

The yield rate of NH_3 was calculated using the following equation:

$$NH_3 \text{ yield rate} = \frac{n_{NH_3}}{S \times t} \quad (3\text{-}4)$$

Where S is the area of electrode (2.4 cm^2); t is the reaction time (1 hour).

The selectivity of NH_3 was acquired by the following equation:

$$\text{Selectivity} = \frac{C_{NH_3}}{\Delta C_{NO_3^-}} \quad (3\text{-}5)$$

Where $\Delta C_{NO_3^-}$ is the concentration difference of nitrate before and after the reaction.

The detection of nitrate and nitrite is analyzed by ion chromatography (metrohm 881 compact IC pro).

The absorbance measurements were performed on Thermo Fisher Varioskan LUX at 697 nm. The obtained calibration curve (Fig. 3-3) was used to calculate the NH_3 concentration.

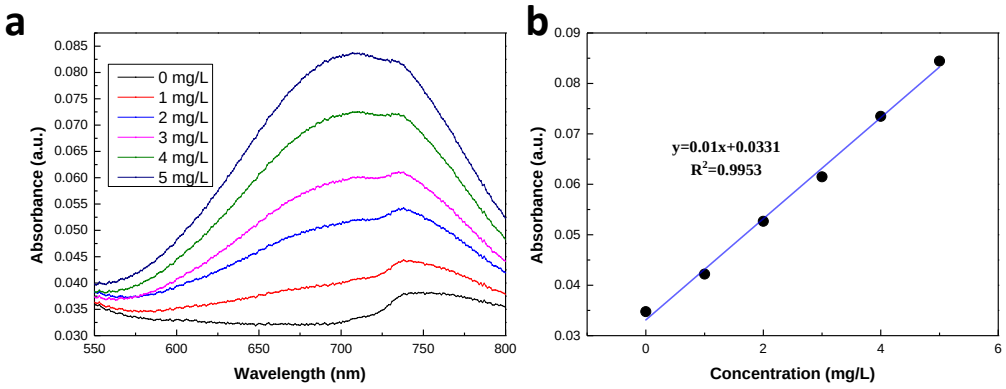

Fig.3-3 (a) the UV-Vis absorption of various NH_3 concentrations. (b) The calibration curve used for calculation of NH_3 concentration.

3-3 Results

3-3-1 The LSV curves of copper-based catalysts

The five electrodes obtained (Cu, CuO, Cu_2O, CuS and Cu_2S) were used to test NRR in 0.1 M Na_2SO_4 (supporting electrolyte) + 0.1 M KNO_3 at room temperature. Before NRR experiments, linear sweep voltammetry **(**LSV**)** curves were performed until the polarization curves reached steady state. Nitrogen was passed through the solution for 5 minutes in advance to remove the interference of dissolved oxygen. As shown in Fig. 3-4, the LSV curves of the electrodes (Cu, CuO, Cu_2O, CuS and Cu_2S) all showed a significant increase in current density in the presence of nitrate, indicating that they all successfully initiated NRR. The Cu electrode exhibited lower current changes over the test potentials range of 0 to -1.0 V_{RHE}, indicating a lower intrinsic NRR activity.

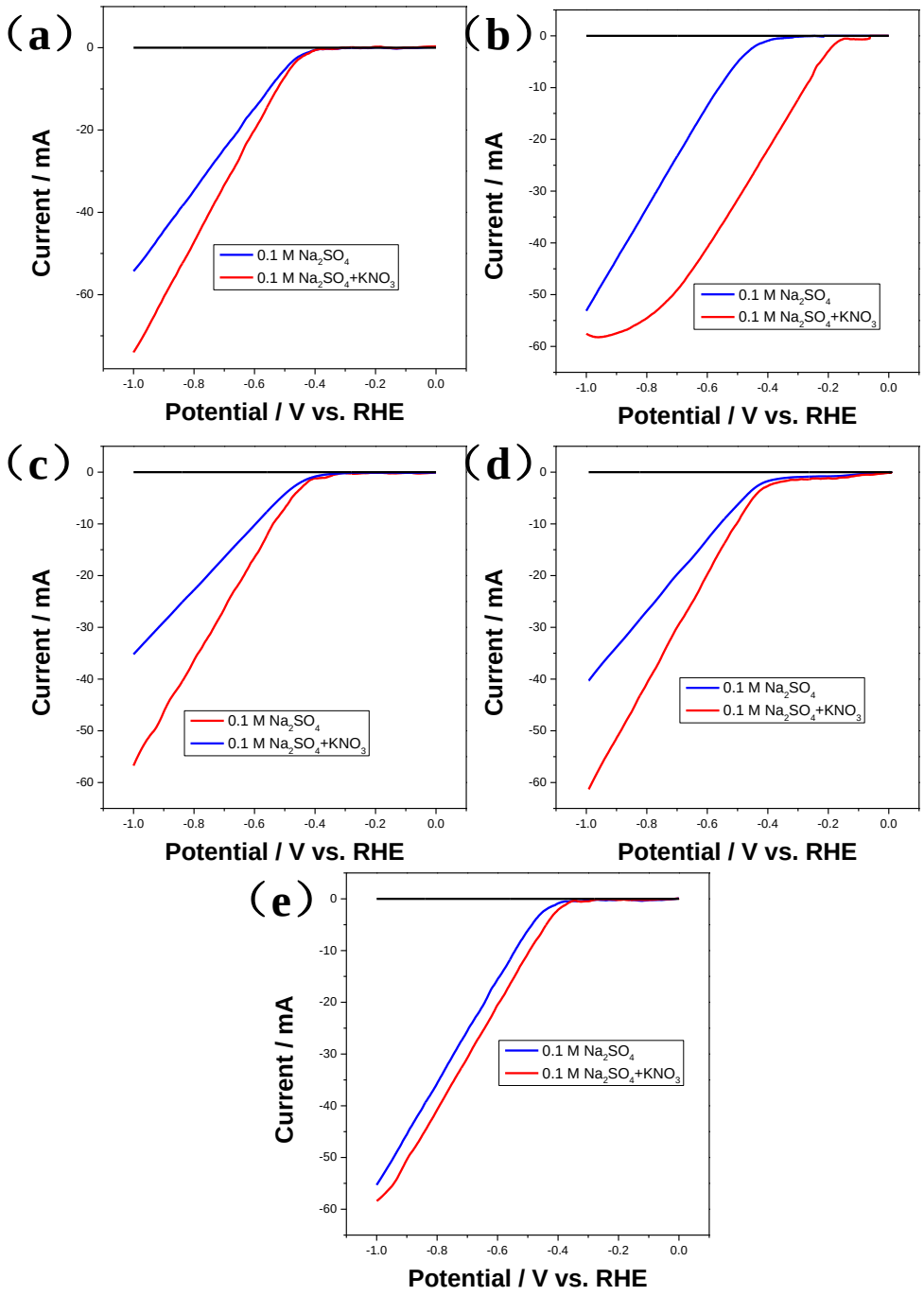

Fig. 3-4 The LSV curves of (a) CuS (b) Cu_2S (c) CuO (d) Cu_2O (e) Cu in 0.1 M Na_2SO_4 with or without 0.1 M KNO_3 at a scan rate of 5 mV s^{-1}

3-3-2 The NRR catalytic activity trend of Cu-based electrodes at different potentials.

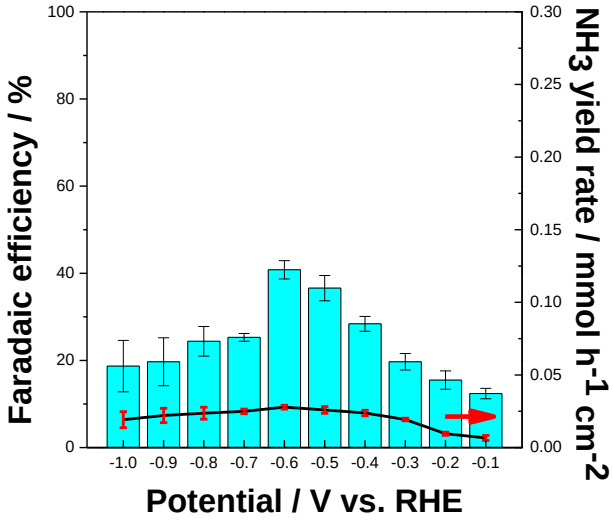

Fig. 3-5 NH_3 FE and yield rate of the Cu electrode at different potentials

Next, the electrocatalytic activity of Cu-based electrodes for NRR was investigated. As shown in Fig. 3-5, the FE and ammonia yield rate of the Cu electrode are both relatively poor only 40.8 % and 0.0278 mmol h^{-1} cm^{-2} (at -0.6 V_{RHE}), respectively.

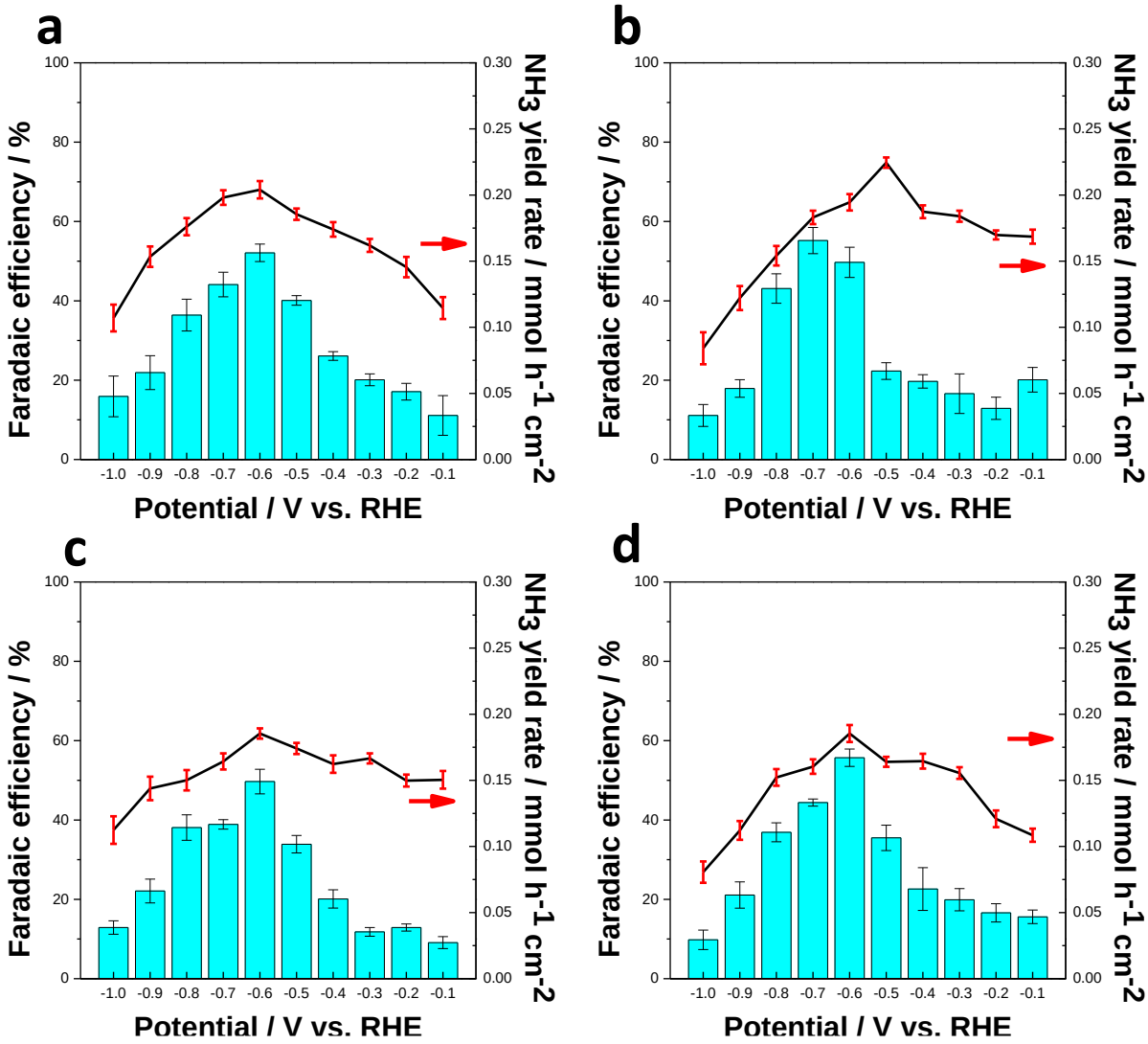

Fig. 3-6 (a) NH_3 FE and yield rate of the CuO electrode at different potentials (b) NH_3 FE and yield rate of the Cu_2O electrode at different potentials (c) NH_3 FE and yield rate of the CuS electrode at different potentials (d) NH_3 FE and yield rate of the Cu_2S electrode at different potentials

Combining Fig.3-6 and Table 3-1, the NRR catalytic performance of CuO, Cu_2O, CuS and Cu_2S electrodes was significantly improved after pure copper electrodes are treated. The FE increased from 40.8% to 55.7%, and the ammonia yield rate also increased nearly 8 times. From –0.1 V_{RHE} to –1.0 V_{REH}, the ammonia yield rate on the electrodes gradually increases, while the FE shows a volcano-shaped curve. After the potential was greater than -0.5 V_{RHE}, the FE and ammonia yield rate showed an overall downward trend. This may be due to the progressive lead of the competing HER at high potentials.

Table 3-1 The optimal catalytic performance for NRR of copper-based catalysts.

Catalyst	FE (%)	NH_3 yield rate (mmol h^{-1} cm^{-2})
Cu	40.8	0.0278
CuO	52.1	0.204
Cu_2O	55.2	0.1831
CuS	49.7	0.1854
Cu_2S	55.7	0.1804

The effects of various applied potentials on the NH_3 yield rate and FE for the products and by-products (NH_3, H_2 and NO_2^-) were studied in 0.1M Na_2SO_4 and 0.1M KNO_3 solution (pH=7).

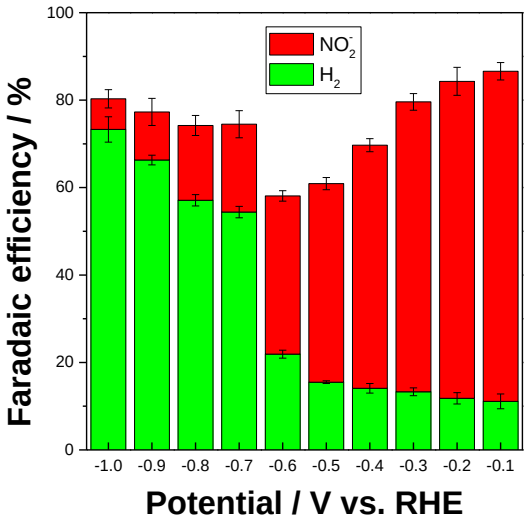

Fig. 3-7 NO_2^- and H_2 FE of the Cu electrode at different potentials

As shown in Fig. 3-7, the FE of hydrogen on the Cu electrode increases with the increase of the potential, and the FE of nitrite decreases with the increase of the potential. This well explains why the NH_3 FE map of the Cu electrode (Fig.3-7) presents a volcano-shaped map. That is, the Cu electrode prefers to generate nitrite (NO_2^- FE of the Cu: 75.5 % at -0.1 V_{RHE}) at low potentials, which leads to the weakened FE of ammonia at low potentials. As the potential continued to increase, the competitive HER (H_2 FE of the Cu: 73.3 % at -1.0 V_{RHE}) gradually took the lead at high potentials, which also led to a decrease in the FE of ammonia. Ammonia FE at the Cu electrode can be optimal only at intermediate potentials where the activity of HER or nitrite-forming reaction is not strong.

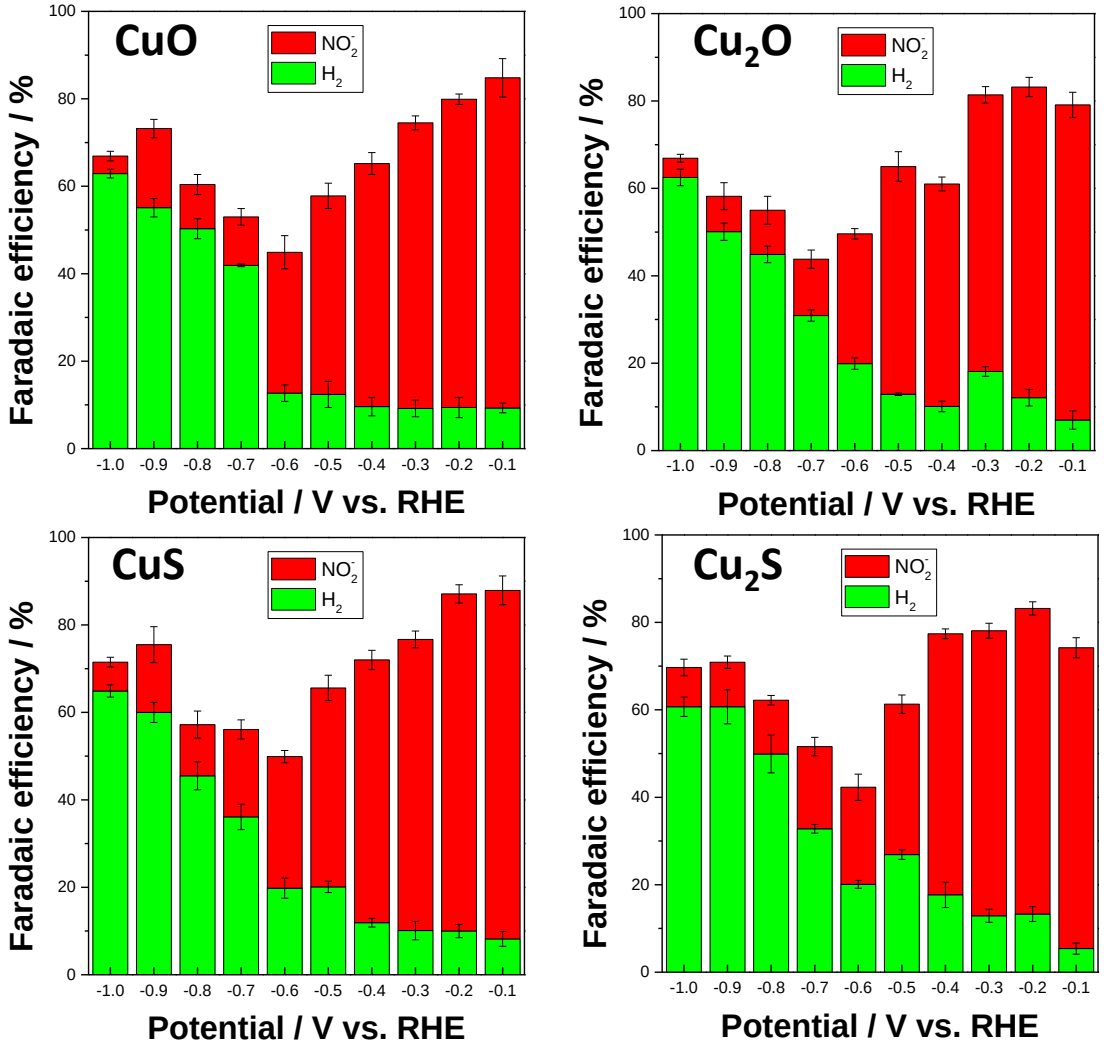

Fig. 3-8 (a) NO_2^- and H_2 FE of the CuO electrode at different potentials (b) NO_2^- and H_2 FE of the Cu_2O electrode at different potentials (c) NO_2^- and H_2 FE of the CuS electrode at different potentials (d) NO_2^- and H_2 FE of the Cu_2S electrode at different potentials

The FE of hydrogen and nitrite on the prepared electrodes (CuO, Cu_2O, CuS and Cu_2S) at different potentials are shown in Fig. 3-8. The prepared electrodes (CuO, Cu_2O, CuS and Cu_2S) basically inherit the product and by-product distribution trends of Cu electrodes at different potentials. For the FE of hydrogen, the prepared electrodes (CuO, Cu_2O, CuS and Cu_2S) showed an obvious decreasing trend, with about 10 % compared to the Cu electrode at -1.0 V_{RHE} (Fig.3-9). For the NH_3 selectivity, their variation values were small (Fig.3-10). This means that the reason for the more NRR catalytic performance of the CuO, Cu_2O, CuS and Cu_2S electrodes may be achieved by suppressing the competitive HER compared to untreated Cu.

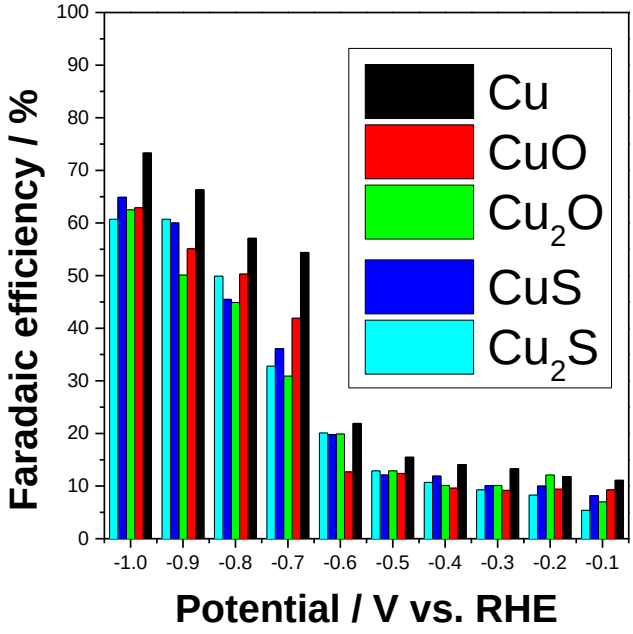

Fig. 3-9 H_2 FE of the prepared electrodes (CuO, Cu_2O, CuS and Cu_2S)

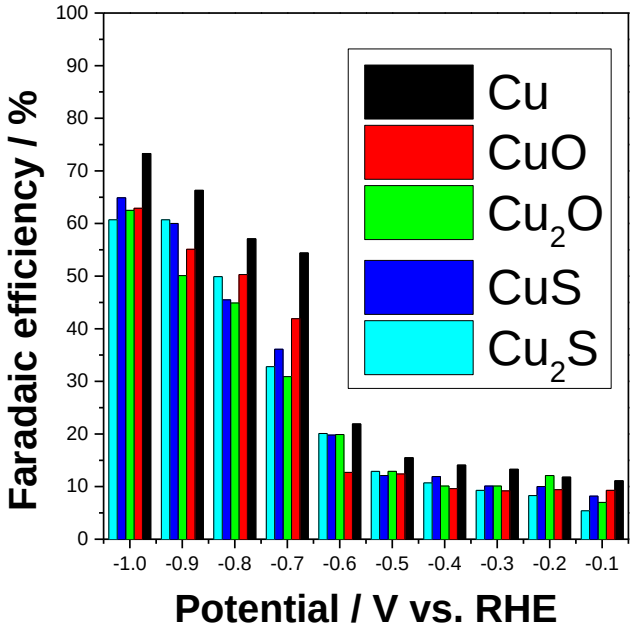

Fig. 3-10 NH_3 selectivity of the prepared electrodes (CuO, Cu_2O, CuS and Cu_2S)

3-3-3 The effect of pH value on NRR catalytic performance

Therefore, in order to further improve the NRR catalytic performance of Cu-based catalysts (Cu, CuO, Cu_2O, CuS and Cu_2S), the following experiments were conducted under the condition of high

potential (avoiding too much nitrite generation) on the effect of pH vaule. In the experiment, the pH value was controlled at 7, 8, 10, 12 and 14 by adding a certain amount of NaOH to the reaction solution.

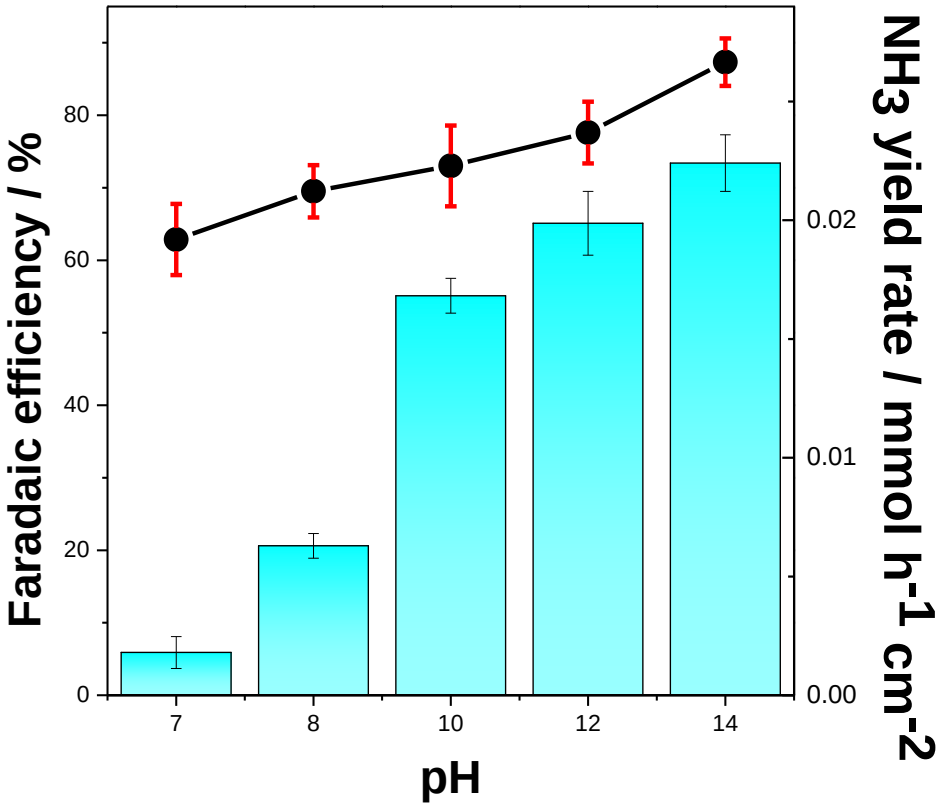

Fig. 3-11 (a) NH_3 FE of the Cu electrode at different pH at -1.0 V_{RHE} (b) NH_3 yield rate of the Cu electrode at different pH at -1.0 $V_{RHE.}$

The experiments were carried out at the high potential (-1.0 V_{RHE}) for the Cu electrode. As shown in Fig. 3-11, both the ammonia FE and the yield on the Cu electrode were enhanced with increasing pH value. This indicates that the inhibition of the competitive HER on the Cu electrode helps to enhance the catalytic activity of NRR. Similarly, the prepared electrodes (CuO, Cu_2O, CuS and Cu_2S) were tested under the same conditions at high potential. Under the condition of high pH value, HER was suppressed on the prepared electrodes, so the catalytic activity of NRR was enhanced (Fig.3-12).

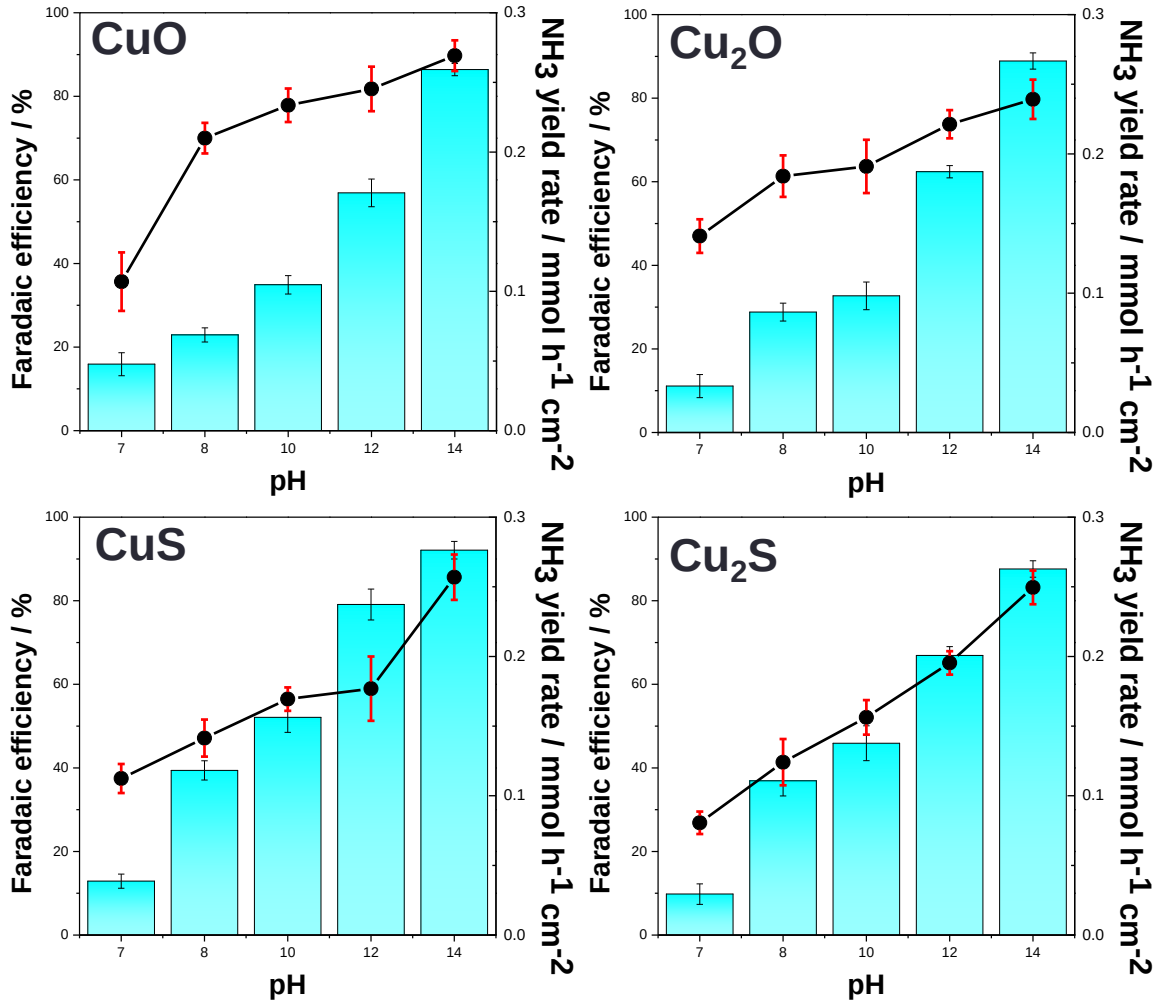

Fig.3-12 (a) NH_3 FE and yield rate of the CuO electrode at different pH at -1.0 $V_{RHE,}$ (b) NH_3 FE and yield rate of the Cu_2O electrode at different pH at -1.0 V_{RHE}, (c) NH_3 FE and yield rate of the CuS electrode at different pH at -1.0 $V_{RHE,}$ (d) NH_3 FE and yield rate of the Cu_2S electrode at different pH at -1.0 V_{RHE}.

3-3-4 The effect of catalyst structure or size on NRR activity

The structure effect of metal catalysts has an important influence on the catalytic activity and selectivity of metal catalysts. From the geometrical point of view, as the metal structure decreases, the low-coordination atoms are gradually exposed and the proportion gradually increases, which significantly changes the structure and proportion of the active center of the catalytic material. From the point of view of electronic structure, the electronic energy levels of metal catalysts also change significantly due to porous structure effect, which greatly affects the orbital hybridization and charge transfer between catalytic materials and reactants.

Therefore, we tried to prepare 3D porous structure Cu-based catalysts on carbon paper (Cu-CP, CuO-CP, Cu_2O-CP, CuS-CP and Cu_2S-CP) by a series of treatments and compare their NRR catalytic activities to study the effect of catalyst structure (Fig.3-13).

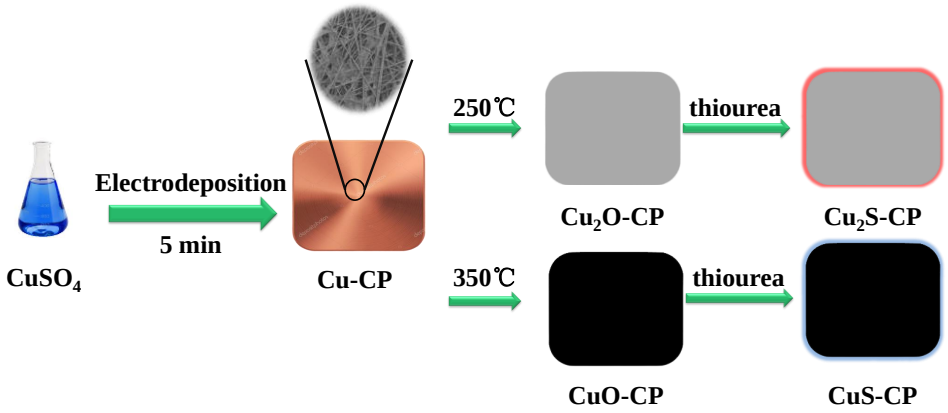

Fig.3-13 Schematic diagram of the processing route of the Cu-based on carbon paper catalyst

The experimental results show that the Cu-CP catalyst has almost no activity (Fig. 3-14a). Almost 100% HER activity was observed (Fig. 3-14b). The same phenomenon was found for the remaining Cu-based (Cu-CP, CuO-CP, Cu_2O-CP, CuS-CP and Cu_2S-CP) electrodes (Fig. 3-15 and 3-16).

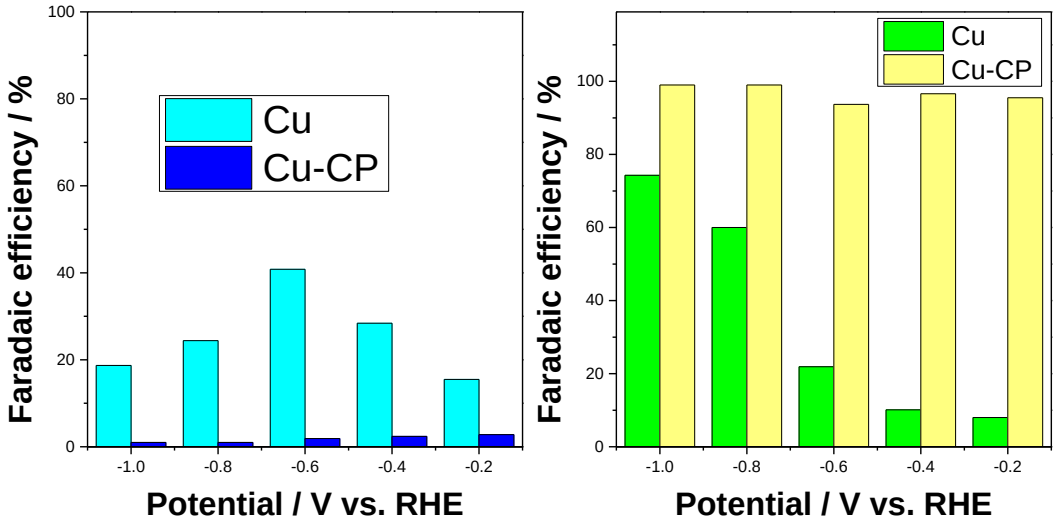

Fig. 3-14 (a) NH_3 FE of the Cu-CP electrode at different potentials, (b) H_2 FE of the Cu-CP electrode at different potentials

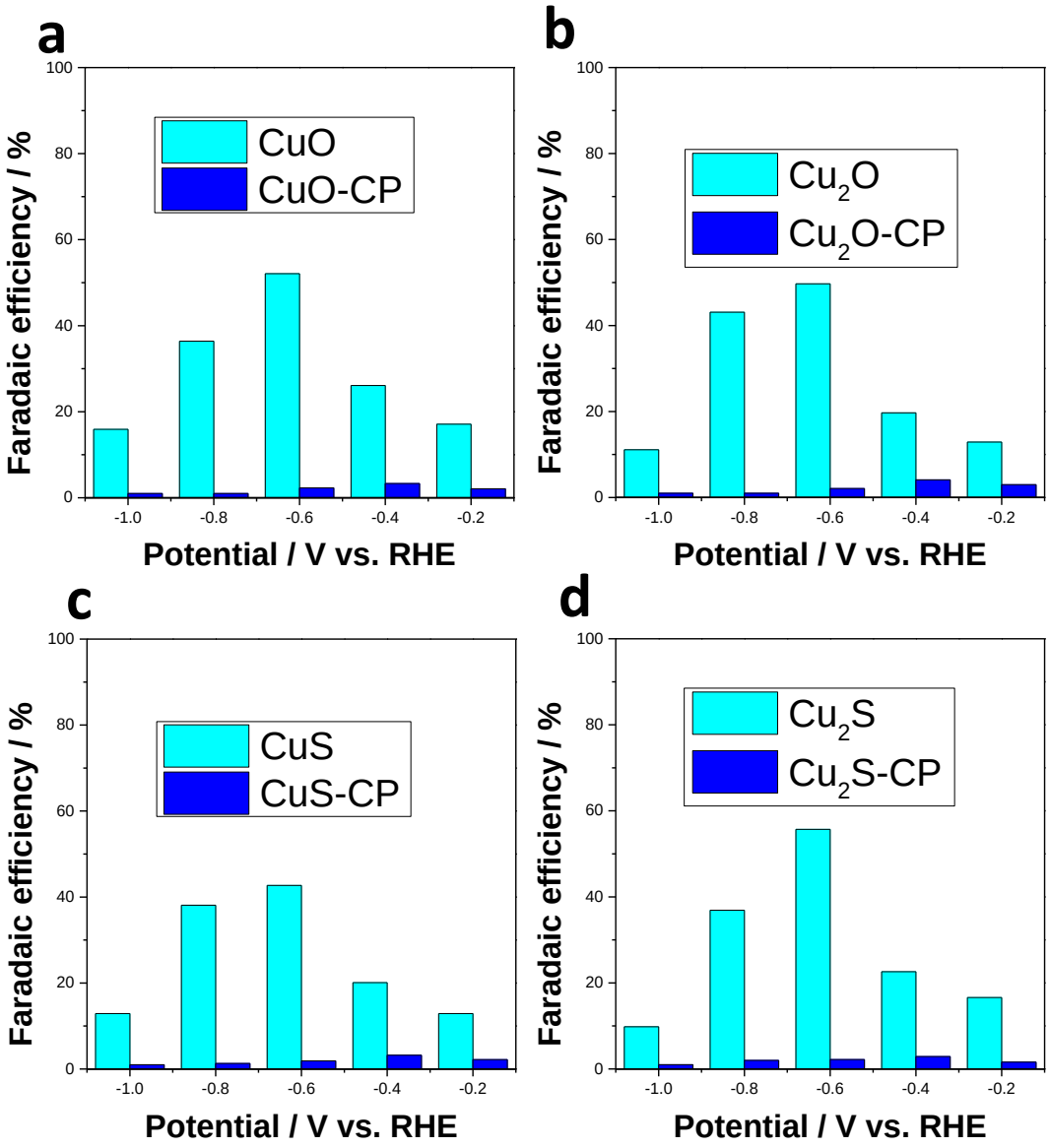

Fig.3-15(a) NH_3 FE of the CuO and CuO-CP electrode at different potentials (b) NH_3 FE of the Cu_2O and Cu_2O-CP electrode at different potentials (c) NH_3 FE of the CuS and CuS-CP electrode at different potentials (d) NH_3 FE of the Cu_2S and Cu_2S-CP electrode at different potentials.

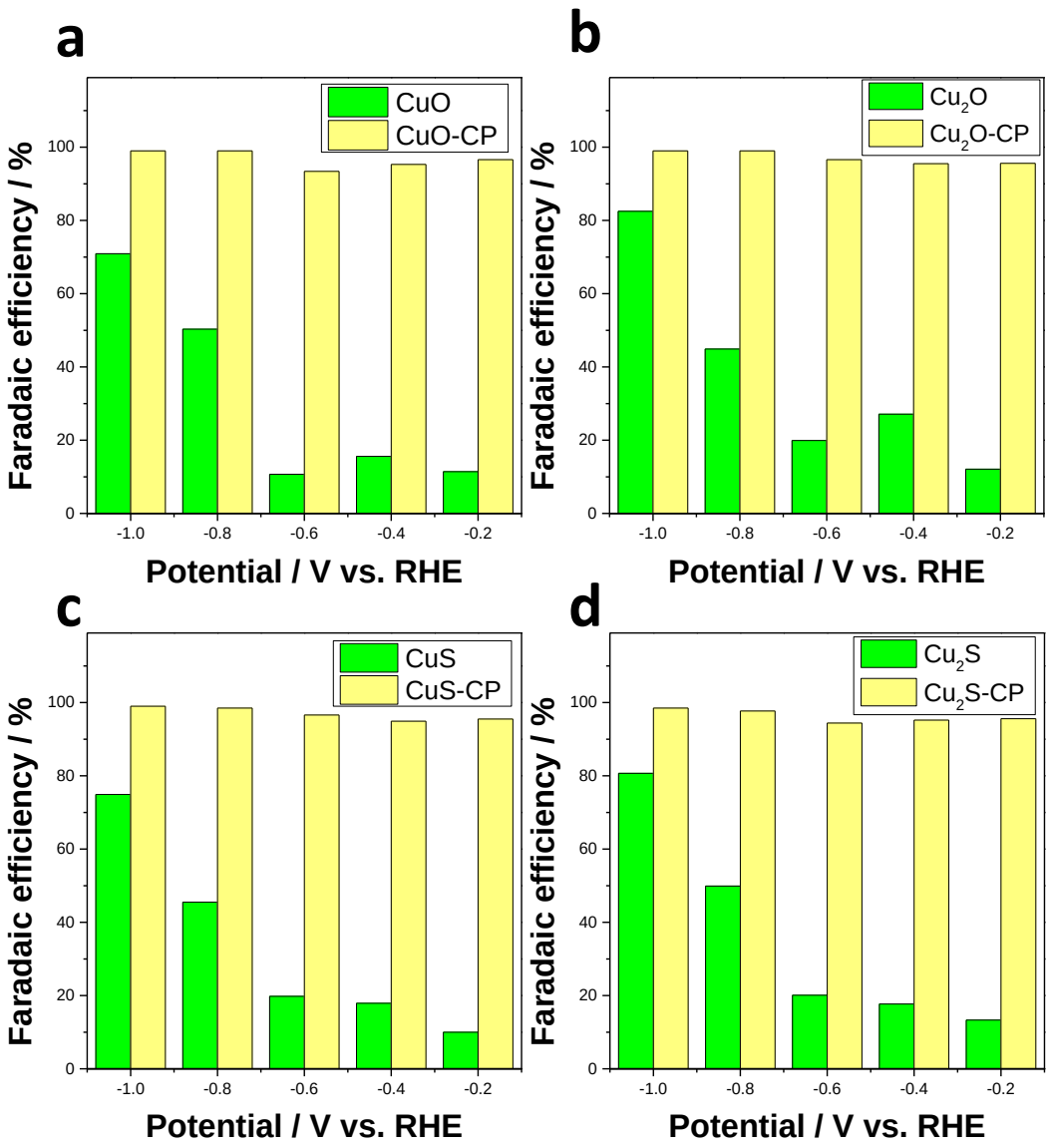

Fig.3-16 (a)H_2 FE of the CuO and CuO-CP electrode at different potentials (b) H_2 FE of the Cu_2O and Cu_2O-CP electrode at different potentials (c) H_2 FE of the CuS and CuS-CP electrode at different potentials (d) H_2 FE of the Cu_2S and Cu_2S-CP electrode at different potentials.

3-3-5 The The LSV curves of of Co-based catalysts

We have known in the previous chapters that among the nine pure metal catalysts, Co element is considered to be the most potential NRR catalyst. For this purpose, we investigated three cobalt-based catalysts.

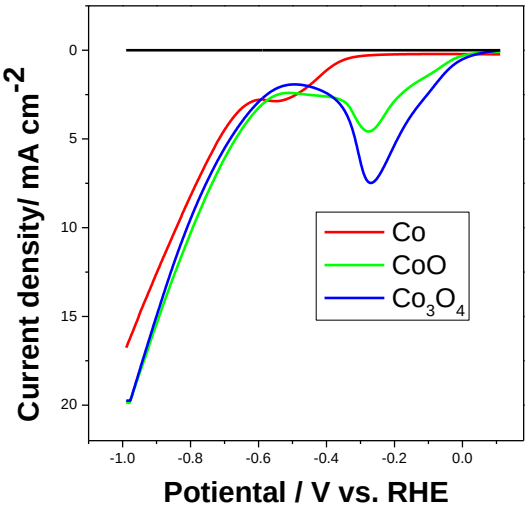

Fig. 3-17 The LSV curves of (red) Co, (green) CoO and (blue) Co_3O_4 electrode in 0.1 M Na_2SO_4 and 0.1 M KNO_3 at a scan rate of 5 mV s^{-1}

Nitrogen gas was passed for 30 minutes to remove oxygen in the solution before scanning, and the scanning speed was 5 mV s^{-1}. As shown in Fig. 3-16, three electrodes were tested for LSV curves in 0.1M potassium nitrate and sodium sulfate solutions. The current density obtained by The Co_3O_4 in the presence of nitrate is significantly larger than that of CoO and Co, indicating that Co_3O_4 has a stronger NRR activity (Fig.3-17).

3-3-6 The NRR catalytic activity of Co-based electrodes at different potentials

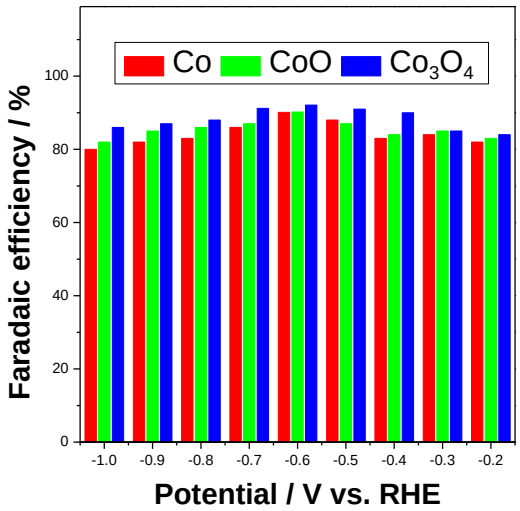

Fig. 3-18 NH_3 FE of (red) Co, (green) CoO and (blue) Co_3O_4 electrode at different potentials

All three cobalt-based electrodes achieved high NRR activity, ranging from -0.2V_{RHE} to -1.0 V_{RHE}. Among them, the Co_3O_4 electrode obtained the highest 92% ammonia FE (at -0.6 V_{RHE}) better than Co and CoO (90.1% and 90.2% at -0.6 V_{RHE}). Surprisingly, their nitrite by-product concentrations were below the detection limit (0.1 ppm). Therefore, it can be considered that their ammonia selectivity is close to 100%.

3-4 Conclusions

Cu-based catalysts are potential NRR catalysts, combination of Cu and O or S will enhance the NRR performance by suppressing HER. Cu-based catalysts are beneficial for NRR at high potential and pH. The 3D porous structure is unfavorable for Cu-based NRR activity due to enhanced HER. The NH_3 yield of Cu-based catalysts is still far inferior to the traditional HB process. Cobalt element is an excellent NRR catalytic activity, and the three cobalt-based catalysts (Co, CoO and Co_3O_4) have achieved near 100% ammonia selectivity and higher than 90% ammonia FE. On the whole, the selectivity of catalysts is likely to be directly determined by the elemental species.

Chapter 4 A porous Co_3O_4-carbon paper electrode enabling nearly 100% electrocatalytic nitrate reduction to ammonia

4-1 Introduction

From the previous chapters we know that the adsorption energy of nitrate determines the activity of NRR, Co and Cu element has the most moderate adsorption energy of nitrate among the nine metals (Ag, Fe, Ni, Co, Cu, Bi, Mo, Ti and Pt) we tested. The selectivity of ammonia is likely to be directly determined by the type of catalyst element. The Cu-based catalysts suffer from poor selectivity. Although high-potential and high-pH methods can be used to achieve better NRR activity on Cu-based catalysts, highly toxic nitrite will inevitably be produced during the catalytic process. In addition, another disadvantage of copper-based catalysts is also very obvious. The limit ammonia yield of Cu-based catalysts (about 0.2 mmol cm^{-2} h^{-1}) is far from meeting the actual needs, and it is far from being comparable to the traditional HB process (< 200 mmol g_{cat}^{-1} h^{-1}). However, Co-based catalysts can maintain 100% ammonia selectivity. Among them, Co_3O_4 has the highest NRR activity among all cobalt-based catalysts. Therefore, in order to obtain better NRR catalysts, in this chapter we will focus on the research of Co_3O_4 catalysts and explore the methods and mechanisms to improve its catalytic performance.

In recent years, various catalysts have been explored and applied to NRR. Determinants of the catalyst's activity and its stability and selectivity include details of its composition, morphology and structure. Also, durability is a very desirable property for the best catalysts as it should run for a longer period of time without showing any degradation in performance. Clearly, over time, catalysts can become deactivated for various reasons; for example, the formation of unwanted intermediates (e.g., H^+) that are strongly bound to the catalyst surface can poison the catalyst, leading to a decrease in its performance. In the search for high-performance catalysts, carbon paper framework catalysts have recently attracted extensive attention as promising and durable catalysts for NRR. Compared with traditional metal-based catalysts, in addition to more flexible structural design. Furthermore, their multilayered hollow structures provide high porosity and thus large active areas and a large number of active sites. All these features can achieve a significant increase in the catalytic activity of NRR.

4-2 Materials and method

4-2-1 Materials and reagants

Sodium sulfate (Na_2SO_4), potassium nitrate (KNO_3), cobalt sulfate ($CoSO_4 \cdot 7H_2O$), Ti plate, sodium hypochlorite (NaClO, available chlorine 4.00-4.99%), sodium nitroprusside ($C_5FeN_6Na_2O$), salicylic acid ($C_7H_6O_3$), Ammonium chloride (NH_4Cl), sodium hydroxide (NaOH) and sodium citrate ($Na_3C_6H_5O_7$). All reagents involved in this experiment are of analytical grade and provided by FUJI-FILM Wako Pure Chemical Corporation, Japan. The nitrate solution required for this study was obtained by dissolving potassium nitrate in ultrapure water.

4-2-2 Electrode preparation

The carbon paper was cut into a size of 12×25 mm (effective area is 12×20 mm). The obtained carbon paper was washed with alcohol and ultrapure water to remove surface impurities.

The Co electrode: First of all, dissolve 1.124 g $CoSO_4 \cdot 7H_2O$ in 100 mL ultrapure water, then add 0.01 g sodium dodecyl sulfate and stirred vigorously for 10 minutes to obtain cobalt solution. The obtained carbon paper was then used as a conductive substrate and applied in a cobalt solution at -2.0 $V_{Ag/AgCl}$ for a period of time. The electrode was then rinsed with alcohol and ultrapure water, dried in an oven at 50 °C. The mass change before and after the carbon paper was calculated to obtain the Co mass loading. Here, the obtained electrode was referred to as a Co electrode. The color of the Co electrode was silver-white.

The CoO electrode: The Co electrode was heated at 300°C for 2 hours. Part of Co was oxidized to CoO and Co_3O_4 by oxygen at high temperature. The composition of this electrode consists of most of CoO and a small amount of Co_3O_4, so it is referred to as a CoO electrode. The color of CoO electrode was green-black.

The Co_3O_4 electrode: The CoO electrode was put into dilute sodium hypochlorite solution and treated for a period of time. During this process, another part of CoO or $Co(OH)_2$ was oxidized to Co_3O_4 by sodium hypochlorite. The color of Co_3O_4 electrode was black.

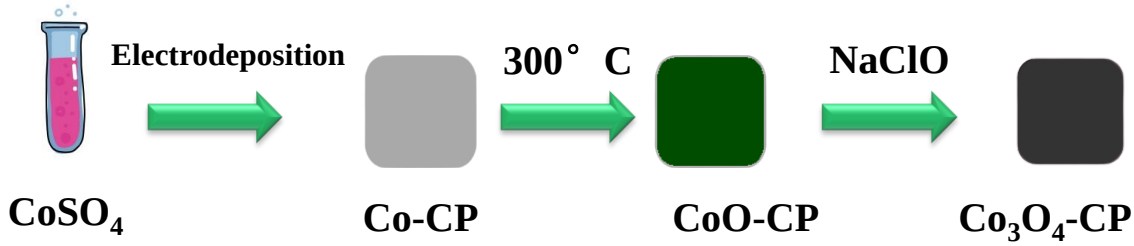

Fig.4-1 Schematic diagram of the processing route of the Co-based catalyst

4-2-3 Electrochemical testing

All electrochemical tests were performed by Potentiostat/Galvanostat HAB-151A (HOKUTO DENKO Corp., Japan) in a three-electrode system at room temperature. The as-prepared Co, CoO and Co_3O_4 was used as the working electrode, Pt wire was used as the counter electrode and Ag/AgCl (filled with saturated KCl) (013691 RE-1CP, ALS Co., Ltd, Japan) was used as the reference electrode to form a three-electrode system. A 100 ml H-type cell was used to study the reduction of nitrate to ammonia. Convert the potential $V_{Ag/AgCl}$ to a reversible hydrogen electrode (V_{RHE}) using the following equation, where $V_{Ag/AgCl}$ *vs.* ^{0}NHE is 196 mV at 25°C.

$$V_{RHE} = V_{Ag/AgCl} + V_{Ag/AgCl}\ vs.0_{NHE} + 0.059 \times pH \quad (4\text{-}1)$$

A proton exchange membrane (PEM Nafion 211) was used to separate the two chambers. A portion of the solution was taken out for product analysis at regular intervals. 80 ml of reaction solution was added to the cathode cell and anode cell, which contained 0.1 M sodium sulfate as supporting electrolyte and 0.1 M potassium nitrate. The resulting reaction solution was diluted dozens of times and used to identify the product and by-product.

4-2-4 Production detection and efficiency calculations

The classical indophenol blue method was used for the identification of ammonia. Dilute the reacted solution in different amounts to ensure that the ammonia concentration in the test solution was within the linear range of this identification method. The identification solution consists of three parts, salicylic acid solution, sodium hypochlorite solution and sodium nitroprusside solution. The salicylic acid solution was obtained by adding 4.4 g of sodium hydroxide, 10 g of salicylic acid and 10 g of sodium citrate to 200 ml of water. Sodium hypochlorite solution was obtained by adding 8 ml sodium hypochlorite and 1.2 g sodium hydroxide to 40 ml with water. Sodium nitroprusside solution was obtained by adding 0.4 g sodium nitroprusside to 40ml with water. The solution to be identified was mixed with 0.1 ml sodium hypochlorite solution, 0.1 ml sodium nitroprusside solution and 0.5 ml salicylic acid solution,

and the volume was adjusted to 10 ml, and the color reaction was at least one hour to ensure that the reaction was complete. The absorption wavelength of ammonia was 697 nm.

The Faradaic efficiency of ammonia was calculated according to the following equation:

$$\mathrm{FE} = \frac{\mathrm{nZF}}{Q} \quad (4\text{-}2)$$

Where n is the moles of ammonia generated; Z is the number of electron transfers towards the formation of 1 mol of ammonia which is 8; F is the Faraday constant (96485 $C \cdot mol^{-1}$); Q is the total current.

The yield rate of NH_3 was calculated using the following equation:

$$NH_3 \text{ yield rate} = \frac{n_{NH_3}}{S \times t} \quad (4\text{-}3)$$

Where S was the area of electrode (2.4 cm^2); t was the reaction time (1 hour).

The selectivity of NH_3 was acquired by the following equation:

$$\text{Selectivity} = \frac{C_{NH_3}}{\Delta C_{NO_3^-}} \quad (4\text{-}4)$$

Where $\Delta C_{NO_3^-}$ was the value of the change in nitrate concentration.

The detection of nitrate and nitrite was analyzed by ion chromatography (metrohm 881 compact IC pro).

4-2-5 Characterization

The scanning electron microscopy (SEM) images were taken with a Keyence VE-9800 3D high-definition electron microscope. The X-ray photoelectron spectroscopy (XPS) images were obtained with AXIS-ULTRA. The absorbance measurements were performed on Thermo Fisher Varioskan LUX at 697 nm. The obtained calibration curve was used to calculate the NH_3 concentration.

4-3 Results

4-3-1 NRR catalytic performance of three Co-based catalysts

All cobalt-based electrodes were subjected to investigation via 1 h electrolysis in an H-type cell. The target product, NH_4^+, present in the reaction solutions were detected utilizing the classical indophenol blue method. In order to differentiate among the NRR activity levels observed among the three cobalt-based catalysts, linear sweep voltammetry (LSV) scans were conducted using 0.1 M Na_2SO_4 + 0.1 M KNO_3. As presented in Fig.4-2, Co_3O_4-CP achieved a higher current density than Co-CP and CoO-CP, demonstrating an enhanced catalytic activity in NRR. The Co_3O_4-CP electrode also yielded a

higher FE and NH_3 yield rate when compared to Co-CP and CoO-CP from −0.2 V_{RHE} to −1.0 V_{RHE} (see Fig. 4-3c and d).

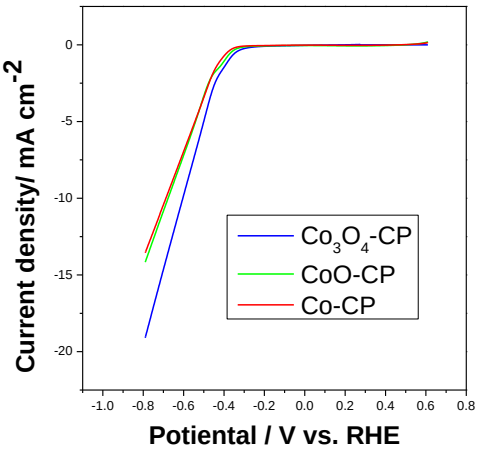

Fig.4-2 The LSV curves of electrodes under 0.1 M Na_2SO_4 + 0.1 M KNO_3 solution

The NRR performance of three different electrodes (Co-CP, CoO-CP and Co_3O_4-CP, electrodeposition time: 2 min, Co mass: 1.07 mg) was first tested, and the results are shown in Fig.3a. The Co_3O_4-CP electrode (82.9%) achieved higher FE than Co-CP and CoO-CP (64.5% and 66.4%) at -0.5 V_{RHE} 0.1M KNO_3. As shown in Table 4-1, the samples treated with sodium hypochlorite for two hours contained the highest Co_3O_4 species components, and also obtained the highest catalytic activity. Therefore, Co_3O_4 species can be considered as the catalytically active species in this study.

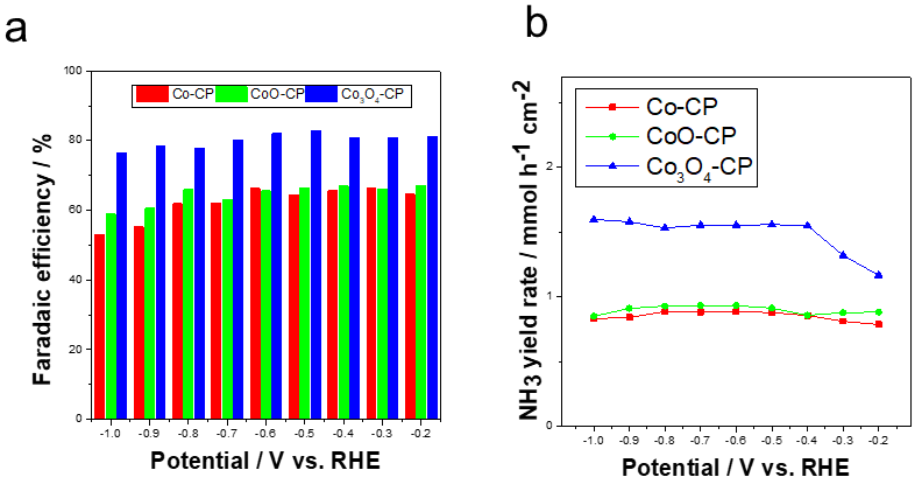

Fig.4-3 (a) NH_3 FE of Co-CP, CoO-CP and Co_3O_4-CP at different potentials, (b) NH_3 yield rate of Co-CP, CoO-CP and Co_3O_4-CP at different potentials.

Table 4-1 Percentage of various cobalt species in Co-CP, CoO-CP and Co_3O_4-CP samples

	Species concentration (atomic %)			
Samples	Co	CoO	Co_3O_4	Others
Co-CP-1	53	38	3	6
Co-CP-2	21	63	5	11
Co-CP-3	7	63	19	11

4-3-2 Influence of electrodeposition time on NRR catalytic performance of Co_3O_4-CP

In view of this, we continued to test Co_3O_4-CP catalysts with different electrodeposition time to continue to optimize the NRR rate. As shown in Fig.4-4, when the electrodeposition time was increased from 1 to 5 min, the FE of NRR gradually increased from 78.7% to nearly 100%. This indicates that the quality of the Co_3O_4-CP (Co mass) loading on the carbon paper has an influence on the NRR. The reason why the Co_3O_4-CP-2 min (Co mass 1.07 mg) failed to achieve the maximum FE may be due to the insufficient Co mass loaded on carbon paper. As the electrodeposition time continued to increase to 6 and 7 min, the FE of the NRR began to deviate from the optimal value. Here we speculate that it is due to excessive Co loading mass. The CoO or $Co(OH)_2$ species reacted with NaClO to generate a large amount of Co_3O_4. When the mass of Co_3O_4 exceeded a certain value, the carbon paper will no longer be able to support, and part of the Co_3O_4 would fall off the electrode. Regarding this point, it has confirmed in many experiments, and found that Co_3O_4 has fallen off at the bottom of the reaction vessel. Therefore, in the following experiments, Co_3O_4-CP with an electrodeposition time of 5 minutes (Co mass 3.65 mg) was used as the working electrode.

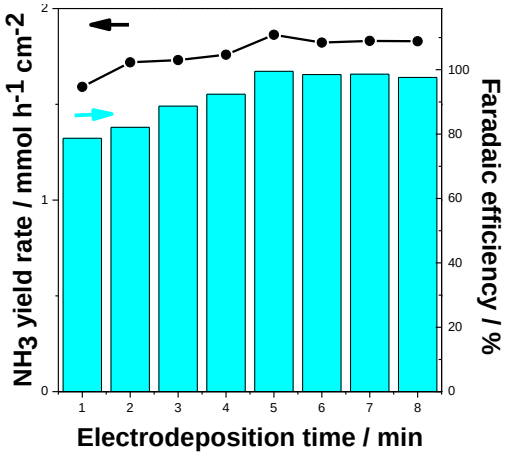

Fig.4-4 The NH_3 FE and yield rate of Co_3O_4-CP in different electrodeposition time at -1.0 V_{RHE}

4-3-3 Influence of high-temperature treatment time on catalytic performance

The study aimed to determine the impact of varying high-temperature treatment durations (0 h, 2 h, 12 h, 24 h, and 48 h) on the NRR. The data revealed that the NRR activity of the electrode exhibited optimal performance after 2 h of heat treatment (as seen in Fig.4-5). Interestingly, as the duration of heat treatment increased, the NRR performance of the electrode tended to decrease. This may have been caused by the prolonged heat treatment that led to catalyst aggregation, thereby reducing the number of available active sites for catalysis. [136, 137]

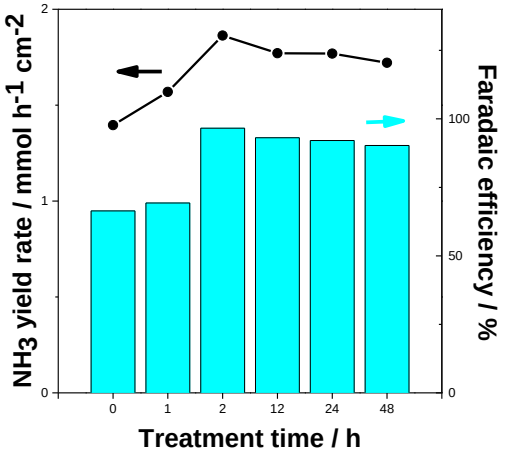

Fig.4-5 NH_3 FE and yield rate of Co_3O_4-CP under different high-temperature treatment time at −1.0 V_{RHE}

4-3-4 Influence of NaClO oxidation time on catalytic performance

The effect of NaClO treatment time on NRR was subsequently investigated, wherein Co_3O_4-CP was prepared by controlling the NaClO treatment time (0 h, 2 h, 12 h, 24 h, 48 h, and 96 h), and their NRR activities were compared. As depicted in Fig. 4-7, the optimal NH_3 FE and yield rate were observed at 48 h of NaClO treatment. The XPS data revealed that the Co_3O_4 species content was highest in the 48 h treatment time, as shown in Table 4-2, thereby establishing a positive correlation between the Co_3O_4 species content and the NRR catalytic activity of the Co_3O_4-CP electrode.

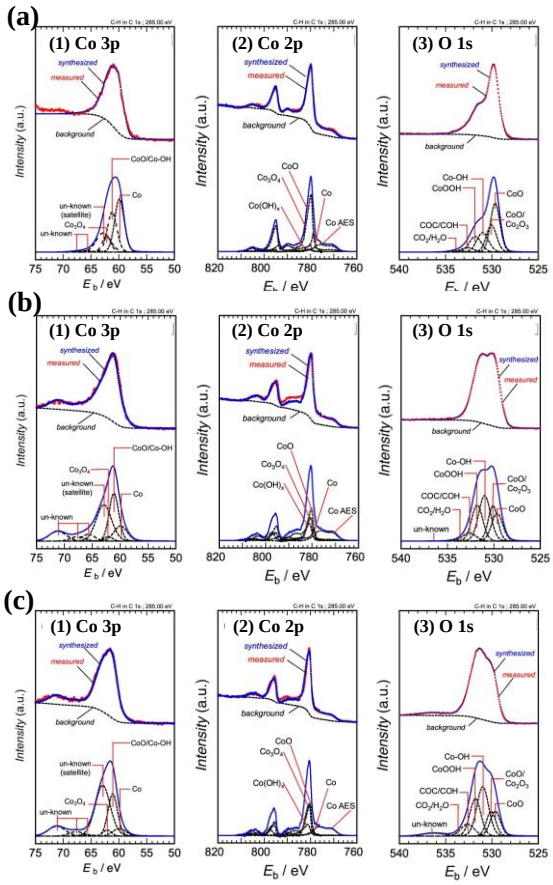

Fig. 4-6 XPS spectra of the various NaClO treatment time samples: (a) 0 h (b) 2 h and (c) 2 days.

Table 4-2 Percentage of various cobalt species in NaClO treatment time samples

	Species concentration (atomic %)			
Samples	Co	CoO	Co_3O_4	Others
0 h	19	63	1	17
2 h	14	55	14	17
12 h	16	51	16	17
24 h	13	49	19	19
48 h	5	54	26	15
72 h	5	52	22	21
96 h	4	52	19	25

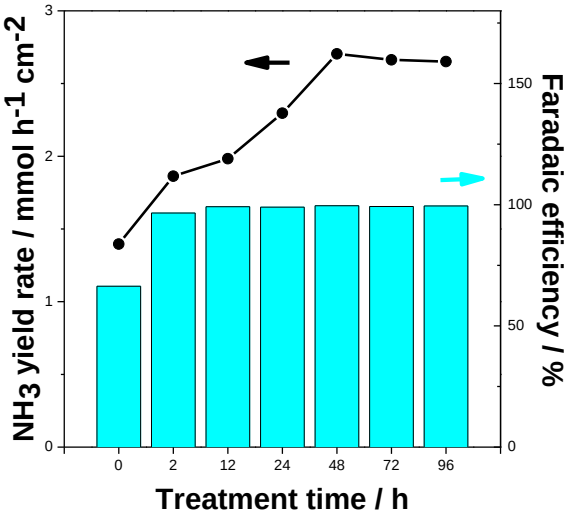

Fig.4-7 (a) NH_3 FE and yield rate of Co_3O_4-CP under different NaClO treatment time at −1.0 V_{RHE}.

After optimizing the preparation process of Co_3O_4-CP, the performance of the NRR electrode was tested in a 0.1M Na_2SO_4 + 0.1M KNO_3 solution at ambient conditions. The Co_3O_4-CP electrode achieved a FE of almost 100% (not less than 98.9%) from −0.2 V_{RHE} to −1.0 V_{RHE}. Moreover, it exhibited a maximum NH_3 yield rate of 3.43 mmol h^{-1} cm^{-2} at −1.0 V_{RHE} (Fig. 4-8).

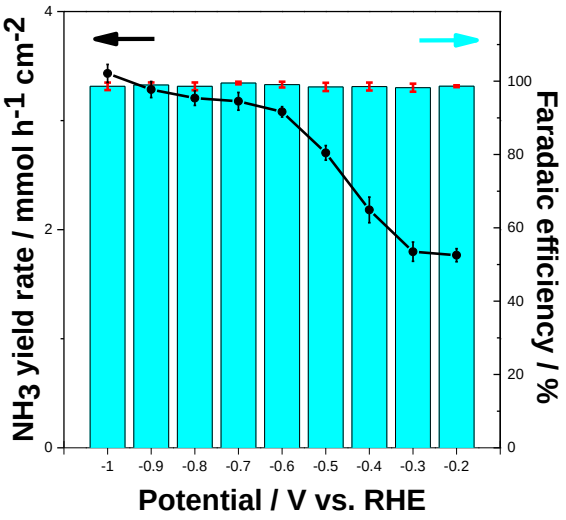

Fig.4-8 The NH_3 FE and yield rate of Co_3O_4-CP at different potentials.

After one hour of catalytic reaction, the concentrations of by-products were analysed. The by-product nitrite was found at a low concentration level ranging from 0.002 to 0.007 ppm (mg/L) (Fig. 4-9). So, the NH_3 selectivity for NRR is considered to be close to 100%.

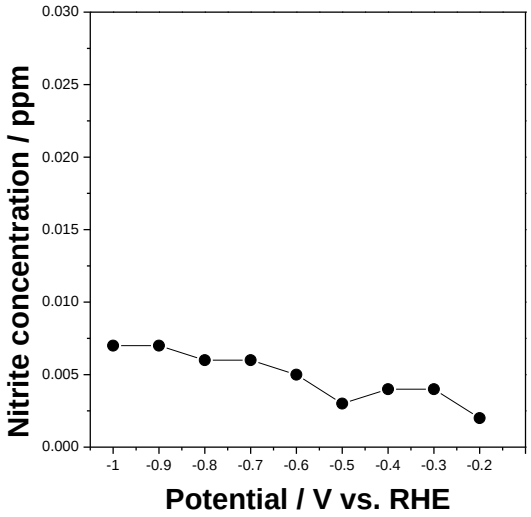

Fig.4-9 By-product nitrite concentration of Co_3O_4-CP at different potentials

4-3-5 Wide application range of the Co_3O_4-CP catalyst

Catalysts having a wider range of applications have many benefits, some of which include: 1. Reduced cost and complexity: Using one catalyst with a wide range of applications can simplify the production process and reduce the number of different catalysts required. This reduces production costs, reduces catalyst management and maintenance, and simplifies the catalyst synthesis and recovery process. 2. Promoting R&D and innovation: Catalysts with broad applicability can encourage more research and innovation. Researchers can apply this catalyst to different chemical transformations and explore new reaction conditions and catalytic mechanisms, thereby promoting scientific progress and the development of new technologies. 3. Enhanced sustainability: Catalysts with broad applicability can be used in a variety of reactions, including eco-friendly reactions and sustainable chemical synthesis. This helps to reduce environmental pollution, save energy and resources, and promote the development of green chemistry. 4. Accelerated conversion rates: Catalysts with broad application ranges generally have higher catalytic activity and higher conversion rates. This makes the chemical reaction more efficient and can be completed in a shorter time.

All in all, catalysts with broader applicability are more flexible, economical, and environmentally sustainable, can promote R&D and innovation, and provide higher reaction selectivity and conversion rate. This makes catalysts with a wide range of applications valuable in many fields, such as chemical synthesis, energy conversion, and environmental protection.

The effectiveness of Co_3O_4-CP for electrochemical NRR was analysed by conducting NRR tests at varying concentrations of nitrate and pH values. The findings have demonstrated that the Co_3O_4-CP is capable of maintaining nearly 100% FE at nitrate concentrations exceeding 0.02 mol/L (as shown in Fig. 4-10). Moreover, the NH_3 FE of the Co_3O_4-CP remained largely unaltered in both neutral and alkaline solutions (Fig. 4-11). These results provide compelling evidence that the Co_3O_4-CP possesses remarkable efficiency in catalysing NH_3 synthesis across a broad range of environmental conditions.

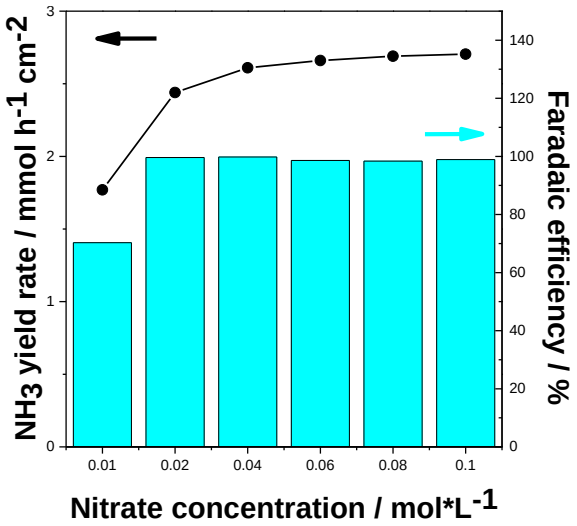

Fig.4-10 The NH_3 FE and yield rate of Co_3O_4-CP under different nitrate concentrations at −1.0 V_{RHE}

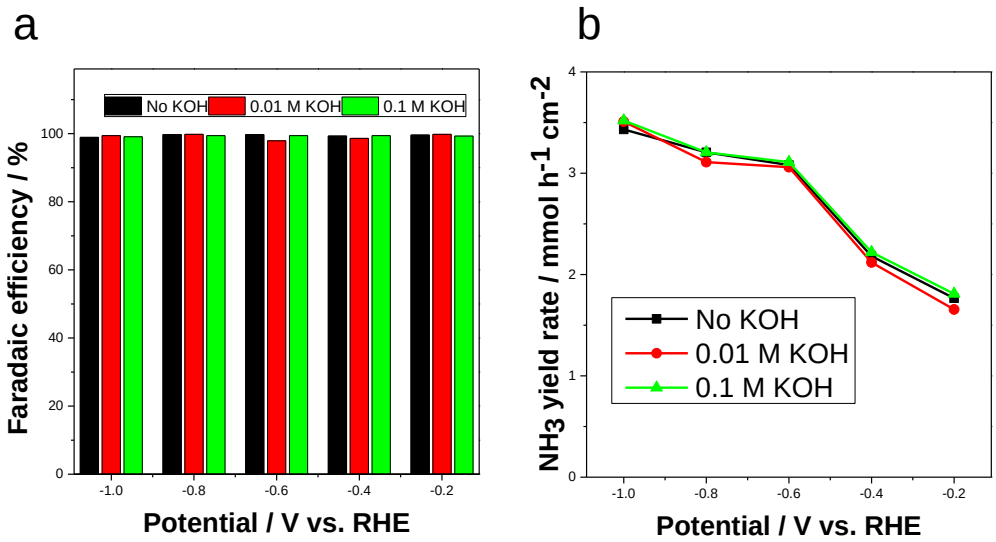

Fig.4-11 (a) NH_3 FE of Co_3O_4-CP under different KOH concentrations at −1.0 V_{RHE}, (b) NH_3 yield rate of Co_3O_4-CP under different KOH concentrations at −1.0 V_{RHE}.

4-3-6 The considerable stability of the Co_3O_4-CP

The electrocatalytic stability of the catalyst was an important factor to evaluate its potential application value. The catalytic durability of Co_3O_4-CP was evaluated by performing NRR at a voltage of -1.0 V_{RHE}. As shown in Fig. 4-12, the ammonia yield rates and FE of the catalyst did not decrease significantly within 4×24 h (FE: 95.5%, ammonia yield: 3.20 mmol h^{-1} cm^{-2}). As the reaction time continued to increase, the ammonia yield rates and FE decayed to 2.98 mmol h^{-1} cm^{-2} and 67.0 % when the

reaction time was 7×24 hours. As shown in Table 4-3, the Co_3O_4-CP showed considerable stability, retaining more than 90% of the maximum ammonia yield and more than 95% of FE after 4×24 h of continuous NRR experiments. And after a 7×24 h NRR experiment, there is an overwhelming advantage over some of the reported catalysts in terms of ammonia yield.

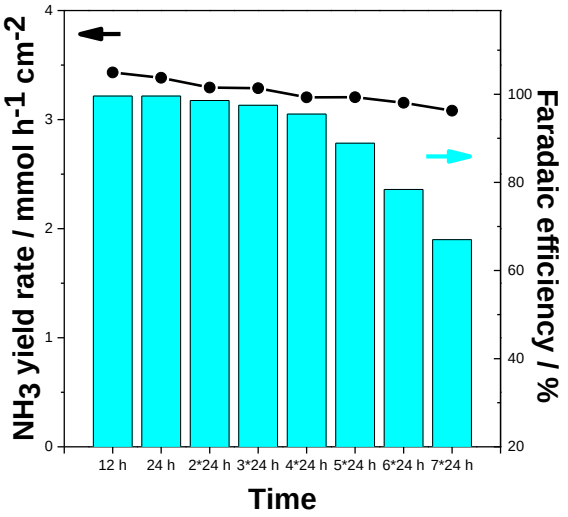

Fig.4-12 NH_3 FE and yield rate of the Co_3O_4-CP in 12 h, 24 h, 2x24 h, 3x24 h, 4x24 h, 5x24 h, 6x24 h and 7x24 h at −1.0 V_{RHE}.

Table 4-3 Reported catalysts for the nitrate reduction to ammonia

Catalysts	FE	NH_3 yield	Conditions
Ti	82%	-	–1.0 V_{RHE} 0.3 M KNO_3 acidic pH
TiO_2	66.3%	0.024 mmol g_{cat}^{-1} h^{-1}	–1.6 V_{SCE} 3.6 mM KNO_3 neutral pH
TiO_{2-x}	85%	0.045 mmol g_{cat}^{-1} h^{-1}	–1.6 V_{SCE} 3.6 mM KNO_3 neutral pH
Cu-PTCDA	85.9%	0.026 mmol cm^{-2} h^{-1}	–0.4 V_{RHE} 3.6 mM KNO_3 neutral pH
$Cu_{50}Ni_{50}$	99%	-	–0.1 V_{RHE} 0.1 M KNO_3 pH 14
Cu/Cu_2O	95.8%	0.245 mmol cm^{-2} h^{-1}	–0.85 V_{RHE} 14.3 mM KNO_3 neutral pH
Strained Ru	nearly 100%	5.56 mmol g_{Co}^{-1} h^{-1} (1.17 mmol cm^{-2} h^{-1})	–0.2 V_{RHE} 1 M KNO_3 pH 14
Co_3O_4-CP	nearly 100%	2255 mmol g_{Co}^{-1} h^{-1} (3.43 mmol cm^{-2} h^{-1})	–1.0 V_{RHE} 0.1 M KNO_3 neutral pH
Used Co_3O_4-CP (After 4×24 h)	95.5%	2100 mmol g_{Co}^{-1} h^{-1} (3.20 mmol cm^{-2} h^{-1})	–1.0 V_{RHE} 0.1 M KNO_3 neutral pH
Ru-based	-	＜200 mmol g_{cat}^{-1} h^{-1}	High temperature and pressure

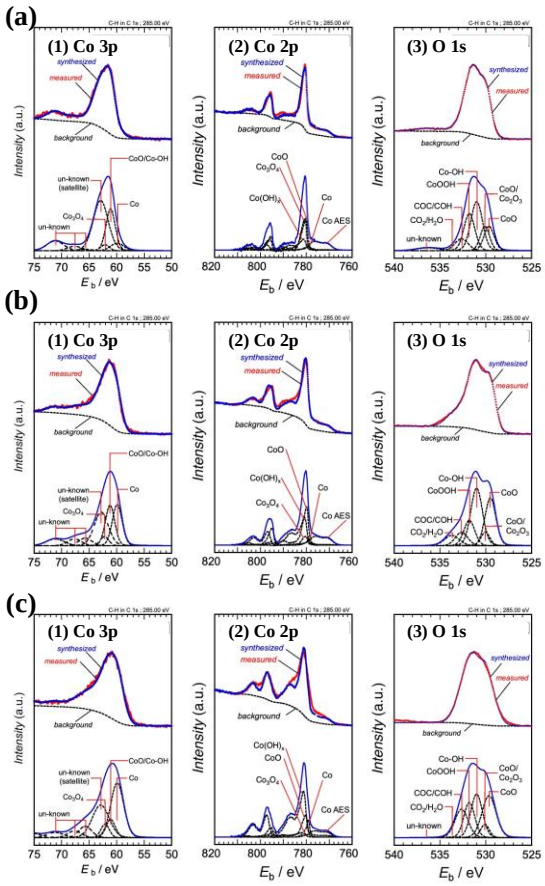

Fig. 4-13 XPS spectra of the different use of time samples: (a) 0 h (b) 12 h and (c) 7×24 h.

4-3-7 Structure and morphology of Co-based catalysts on carbon paper

The morphology of the obtained samples was observed by SEM, as shown in Fig. 4-14. It can be seen from Fig. 4-14a that the carbon paper was composed of complex interlaced carbon fibers. The enlarged image of the carbon paper was shown in Fig. 4-14b, and there were large voids among the 3D interlaced carbon fibers. It can be seen from Fig. 4-14c and d that the Co_3O_4-carbon paper (CP)obtained by the electrodeposition method can be uniformly attached to the carbon fibers. By comparing the SEM pictures of carbon paper and Co_3O_4-CP. It can be clearly found that the Co_3O_4-CP catalyst was densely and uniformly grown on carbon fibers by electrodeposition. On the basis of carbon paper, a Co_3O_4-CP electrode with a 3D porous structure was successfully fabricated. The CP was tested by NRR alone, showing almost no catalytic activity, thus eliminating the influence of CP on catalytic activity (Fig.4-15).

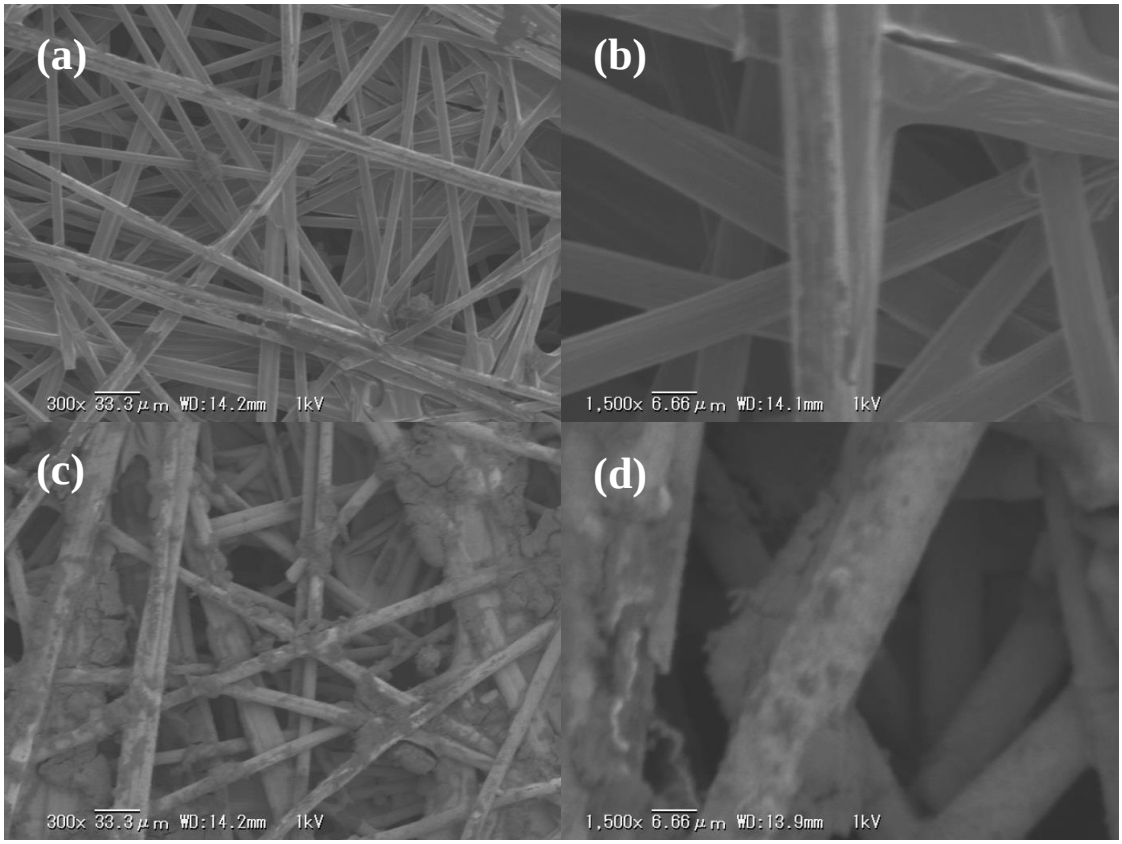

Fig. 4-14 SEM image of (a) carbon paper (33.3 μm), (b) carbon paper (6.66 μm), (c) Co_3O_4-carbon paper (33.3 μm), (d) Co_3O_4-carbon paper (6.66 μm).

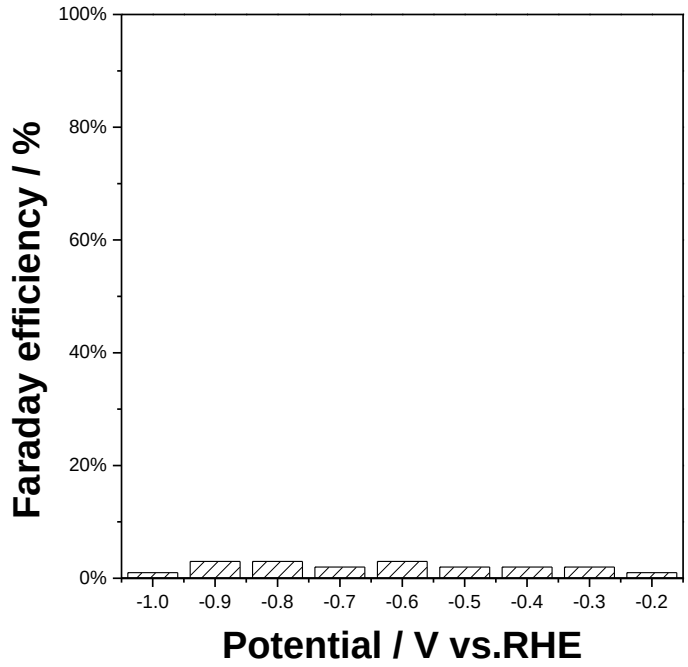

Fig.4-15 NH_3 FE of carbon paper at different potentials

To investigate the chemical composition and surface chemical state of the as-prepared electrodes, XPS measurements were performed. As shown in Fig.4-16a from the measured spectra of three different electrodes (Co-CP, CoO-CP and Co_3O_4-CP), all of them were mainly composed of Co and O elements. As shown in Fig. 2b, the peaks at 67.8 and 780.2 eV found in the Co_3O_4 sample belong to Co_3O_4, while the peaks at 78.7, 530.5 and 780.5 eV belong to CoO, and 779.8 eV belongs to $Co(OH)_2$. As shown in Fig. 4-16c and d, the XPS spectra of Co and CoO showed that at least two different cobalt compounds were contained therein. The reason why CoO, $Co(OH)_2$ and trace of Co_3O_4 were found in the Co electrode may be that scattered and fine Co was unstable in air and easily reacted with oxygen directly. This is in line with previous related studies [138, 139]. As shown in Table 1, the three electrodes contained different proportions of cobalt species. To determine the crystal structure, we performed a single crystal powder X-ray diffraction (XRD) test on the samples. The Fig. 4-17 shows the observed and calculated XRD patterns of the samples. The main diffraction peaks of Co-CP observed at 2θ=44.2° and 51.5° belong to (1,1,1) and (2,0,0) Co planes (PDF No: 00-015-0806). The main diffraction peaks of CoO-CP observed at 2θ=42.4° and 61.5° belong to (2,0,0) and (2,2,0) CoO planes (PDF No: 00-009-0402). The main diffraction peaks of Co_3O_4-CP observed at 2θ=31.1°, 36.2°, 44.8° and 59.3° belong to (2,2,0), (3,1,1), (4,0,0) and (5,1,1) Co_3O_4 planes (PDF No: 00-042-1467). The intensity difference is attributed to disordered object species in the pores, which is not accounted for in the crystal structure model. These detection results demonstrate that Co-CP, CoO-CP and Co_3O_4-CP electrodes were successfully fabricated.

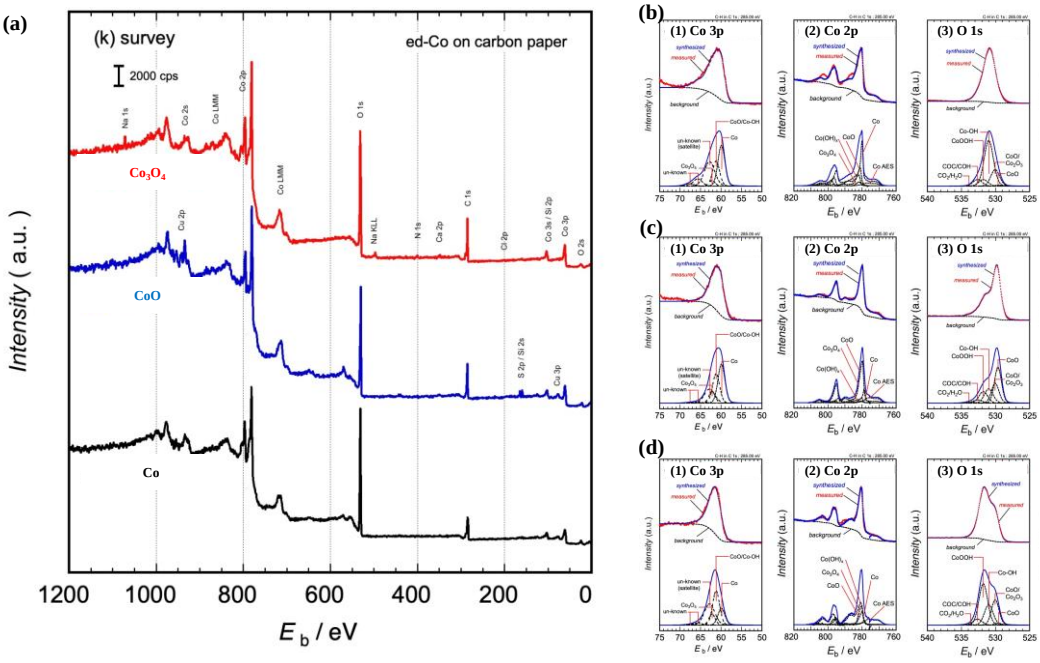

Fig. 4-16 XPS spectra of the samples: (a) survey scan, (b) Co-CP, (c) CoO-CP, and (d) Co_3O_4-CP.

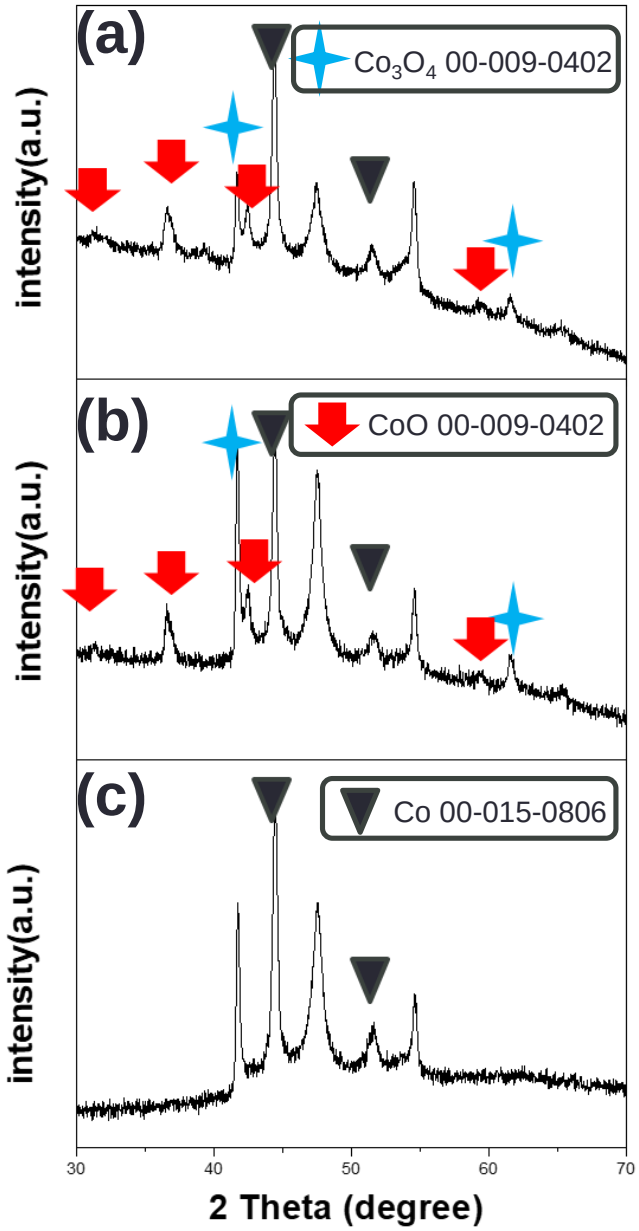

Fig. 4-17 XRD spectra of: (a) Co_3O_4-CP (b) CoO-CP and (c) Co-CP.

Table 4-4 Percentage of various cobalt species in Co-CP, CoO-CP and Co_3O_4-CP samples.

	Percentage (%)		
Samples	**Co**	**CoO**	**Co_3O_4**
Co-CP	53	38	3
CoO-CP	21	63	5
Co_3O_4-CP	7	63	19

4-3-8 Efficient and affordable the Co_3O_4-CP for NRR catalysts

Another must-have feature for catalysts for large-scale practical application is affordability. The huge cost of precious metal catalysts will greatly limit their applications. Take the ruthenium-based

catalyst as an example [125], one of the best reported catalysts, the price of noble metal Ru was about 312 times that of metal Co (The average price of Ru was 271.83 U.S. dollars per troy ounce (about 31.1 g), Co was 28000 U.S. dollars per metric ton (10^6 g) in 2020). Calculated for ammonia production per gram of catalyst per hour, Ru was nearly 419 times higher than Co. From this calculation, the cost of producing moles of ammonia on the catalyst, the Co_3O_4-CP catalyst is about 130,000 times less than the Ru-based catalyst. Therefore, due to the advantages of Co_3O_4-CP catalyst in terms of high catalytic activity and affordable cost, it endows Co_3O_4-CP with great potential for NRR application.

4-4 Reaction Mechanism

From the above analysis and discussion, it can be seen that the electrocatalytic NRR performance of the as-prepared Co_3O_4-CP electrode was excellent compared to previous studies. However, the origin of this efficient catalysis was unknown. Next, we sought to understand the origin of the efficient catalytic ammonia electrosynthesis of Co_3O_4-CP electrode.

4-4-1 high intrinsic activity of the Co_3O_4 species

First, we compared the NRR activity of Co_3O_4-CP, CoO-CP and Co-CP electrodes, we can see that Co_3O_4-CP >CoO-CP>Co-CP. By studying the composition of the electrode, it can be clearly found that the reason for the best catalytic performance of the Co_3O_4-CP electrode may be that the content of Co_3O_4 species was the highest as shown in Table 1. Subsequent experiments with prolonged sodium hypochlorite treatment time again showed that the Co_3O_4 species content in the electrode can significantly affect the FE and ammonia yield rate of NRR experiments. Then, the relationship between the composition change and catalytic activity of the Co_3O_4-CP electrode was compared. The FE and ammonia yield rate of the Co_3O_4-CP electrode decayed after a period of time after continuous NRR-catalyzed reaction. In this regard, XPS tests were performed to study the compositional changes of the electrodes. The Co_3O_4 species component in the electrode decays with the use of time, and the catalytic performance also decays. Therefore, the above three different test experiments have proved that the Co_3O_4 species and the high catalytic performance of NRR are closely related. After continuous use for 7×24 h, the study under the condition that only 2% of the Co_3O_4 species remained in the electrode can obtain excellent catalytic performance in terms of ammonia yield rates compared to the previous study. From this, we can think that one of the origins of the efficient catalysis of NRR by the Co_3O_4-CP electrode may be the high intrinsic activity of the Co_3O_4 species therein.

4-4-2 The contribution of the 3D porous structure

As discussed above and shown in Fig. 4-14, the Co_3O_4-CP electrode was confirmed to have a 3D porous structure. To confirm the effect of the 3D porous structure on the NRR experiments, Co_3O_4-Ti without the 3D porous structure was prepared as a control sample using the same preparation method. Here, the Ti plate substrate is a flat metal plate with a purity of 99%, as compared to the carbon paper substrate used before with a porosity of up to 80%. The results are shown in Fig. 4-18, the catalytic activity of Co_3O_4-Ti was significantly lower than that of Co_3O_4-CP at all tested voltages. Therefore, it can be considered that the high NRR catalytic activity of the Co_3O_4-CP electrode may originate from its 3D porous structure.

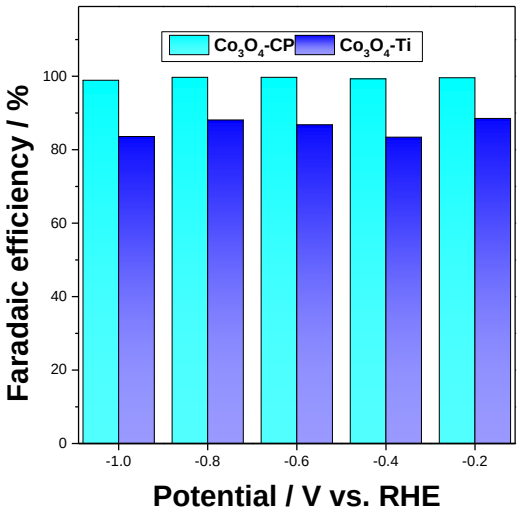

Fig.4-18 NH_3 FE of Co_3O_4-CP and Co_3O_4-Ti at different potentials.

4-4-3 Suppression of HER by the Co_3O_4 species

The reaction solution system of this experiment was composed of 0.1M Na_2SO_4 and KNO_3. From the previous by-product analysis results, it was found that there was almost no side reaction other than the HER. So there were only two reactions in the whole reaction process, NRR and HER:

$$NO_3^- + 8e^- + 9H^+ \rightarrow NH_3 + 3H_2O \quad (4\text{-}5)$$

$$2H^+ + 2e^- \rightarrow H_2 \quad (4\text{-}6)$$

According to previous studies, the current density at the same potential can be used as a standard to evaluate the HER activity of the electrode in the HER-only condition. [140-147] For this reason, the experiments in 0.1 M Na_2SO_4 solution were designed to investigate activity of the HER on the electrodes. The electrodes with different Co_3O_4 species content were obtained using the same process by controlling different NaClO treatment time. They have different current densities at the same potential (Fig. 4-19).

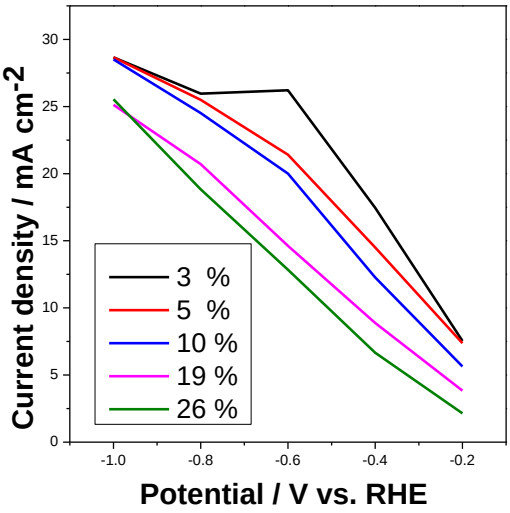

Fig.4-19 The HER current density of electrodes with different Co_3O_4 species content at different potentials

The electrode with higher Co_3O_4 species content has lower current density, which indicates its poorer HER activity. Meantime, these electrodes were tested for NRR performance in 0.1 M Na_2SO_4 + 0.1 M KNO_3 solution. The Co_3O_4-CP with higher Co_3O_4 species content showed higher NRR activity (Fig. 4-20).

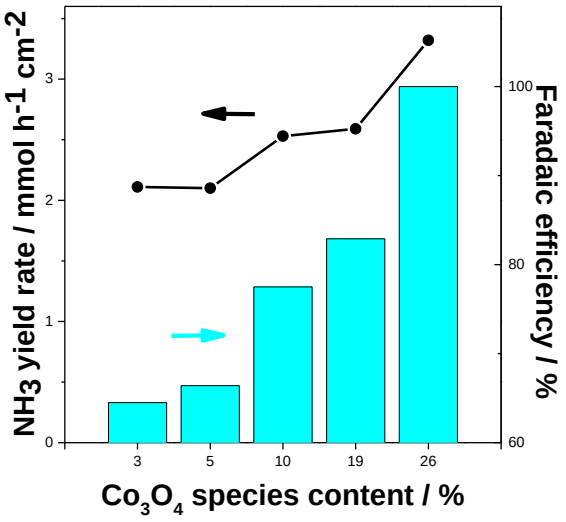

Fig.4-20 NH_3 FE and yield rate of electrodes with different Co_3O_4 species content at −1.0 V_{RHE}

The corresponding by-product analysis shows the Co_3O_4-CP with different Co_3O_4 species content kept extremely low nitrite concentrations, and the NH_3 selectivity was almost 100% at all conditions (Fig. 4-21). Then, by the law of conservation of energy, the FE of H_2 can be calculated (Fig. 4-22). The results shows that high Co_3O_4 species content suppressed HER during NRR. The HER was suppressed to nearly 0 at Co_3O_4 species content of 26 %. Therefore, it may be reasonable to speculate that the higher

Co_3O_4 species content on the Co_3O_4-CP suppressed the competitive HER and thus indirectly enhances the NRR activity in 0.1 M Na_2SO_4 + 0.1 M KNO_3 solution at all given conditions.

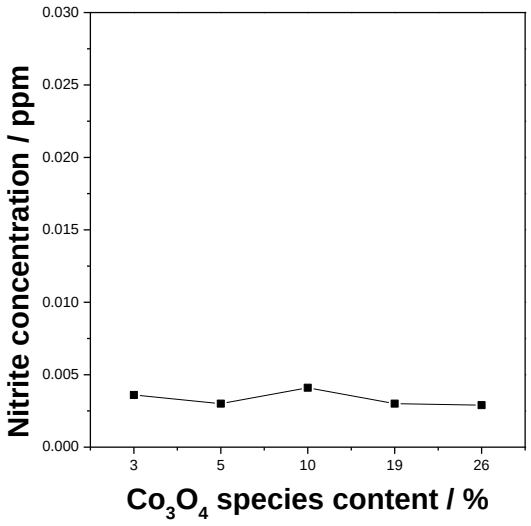

Fig.4-21 By-product nitrite concentration of electrodes with different Co_3O_4 species content at −1.0 V_{RHE}

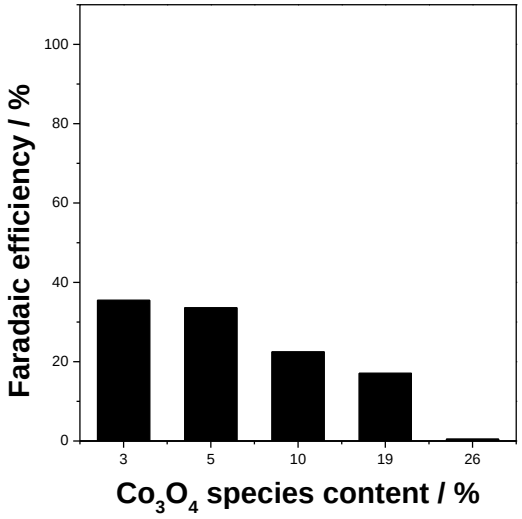

Fig.4-22 H_2 FE of electrodes with different Co_3O_4 species content at −1.0 V_{RHE}

4-5 Conclusion

In conclusion, we successfully synthesized novel Co_3O_4-CP catalysts on carbon paper by a facile process using affordable Co metal and used them to electrocatalyze the reduction of nitrate to ammonia in neutral pH under ambient condition. Nearly 100% FE for ammonia synthesis can be maintained at application voltages from -0.2 V_{RHE} to -1.0 V_{RHE}. The highest ammonia yield was obtained as 3.48 mmol h^{-1} cm^{-2}, and the high catalytic activity of 2.98 mmol h^{-1} cm^{-2} remained after continuous use for 7×24 h. The comprehensive experimental results suggest that the 3D porous structure of Co_3O_4-CP electrode, high intrinsic activity of Co_3O_4 species and its poor HER activity may be the origin of the excellent NRR catalytic activity of Co_3O_4-CP electrode. These excellent properties demonstrated the great application potential of using Co_3O_4 as an electrocatalyst for catalyzing nitrate reduction to ammonia.

Chapter 5 Conclusion and discussion

This thesis aims to explore and study catalysts for the efficient electrocatalytic reduction of nitrate to ammonia. Through in-depth studies on the mechanism and catalyst performance of this catalytic reaction, we aim to improve the energy efficiency and environmental sustainability of ammonia synthesis. In this study, we employ a variety of experimental and characterization techniques, as well as theoretical simulations, to evaluate the catalytic activity and selectivity of different catalysts and reveal the details of the reaction mechanism.

First, we reviewed the reaction mechanism of nitrate reduction to ammonia. This reaction involves a complex electrocatalytic process, including steps such as adsorption, dissociation, intermediate formation, and ammonia release. We analyze different mechanistic hypotheses and reaction pathways and summarize key findings from previous studies. Then, we employed theoretical simulation methods, such as density functional theory (DFT), to explore the detailed mechanism of nitrate reduction to ammonia. By constructing reaction models and calculating electronic structures, we are able to predict the structures and stability of reaction intermediates, and study the activation energy and reaction kinetics of key steps. These theoretical calculations provide insight into the details of the reaction mechanism.

During the research, we also combined the experimental data for verification. Through electrochemical testing and catalyst characterization techniques, we obtained experimental observations of the reaction process. These experimental data and theoretical simulation results corroborate each other and strengthen our understanding of the mechanism of nitrate reduction to ammonia. At the end of Chapter 2, we summarize the main findings from the mechanistic studies of nitrate reduction to ammonia. We identify the formation and dissociation processes of key reaction intermediates, revealing energy barriers and rate-limiting steps in the reaction pathways. These findings have important implications for designing and optimizing highly efficient catalysts and improving reaction conditions for ammonia synthesis.

Overall, the findings in Chapter 2 provide insights into the mechanism of nitrate reduction to ammonia. Through theoretical simulation and experimental verification, we revealed the characteristics of key reaction steps and intermediates, providing a theoretical basis for further improving the efficiency

and selectivity of ammonia synthesis. These research results are of great significance for promoting the development and application of ammonia synthesis.

The Chapter 3 of this dissertation focuses on the study of copper and cobalt-based catalysts in the reduction of nitrate to ammonia. We found that the ammonia selectivity is likely to be directly influenced by the elemental species, and the cobalt-based catalysts exhibited excellent catalytic potential.

First, we detail the use of copper and cobalt as catalysts for the reduction of nitrate to ammonia. These two catalysts have been widely studied and applied to this reaction, and have different catalytic activities and selectivities. We summarize the characteristics and performance of copper- and cobalt-based catalysts in previous studies.

Next, we designed and prepared a series of copper- and cobalt-based catalysts, and evaluated their catalytic performance. Through electrochemical tests and product analysis, we determined the catalytic activity and ammonia selectivity of the different catalysts. The results show that the cobalt-based catalyst exhibits excellent catalytic performance with high ammonia selectivity and high electrocatalytic activity, while the copper-based catalyst has relatively low ammonia selectivity.

To explain this finding, we performed further characterization and analysis. Using X-ray photoelectron spectroscopy (XPS), and other characterization techniques, we investigated the surface composition, crystal structure, and morphology of the catalysts. These characterization results reveal the microscopic features of copper and cobalt-based catalysts, providing an explanation for their differences in catalytic performance.

Finally, we discuss the underlying mechanism of cobalt-based catalysts in the reduction of nitrate to ammonia. We propose a possible reaction mechanism involving the formation and dissociation of active sites and intermediates on the cobalt catalyst surface. The results of these mechanistic studies provide guidance for further optimizing the activity and selectivity of Co-based catalysts.

In summary, the Chapter 3 of this thesis investigates the performance of copper- and cobalt-based catalysts in the reduction of nitrate to ammonia. We found that the ammonia selectivity is likely to be directly affected by the elemental species, and the cobalt-based catalyst exhibited excellent catalytic potential. These findings are of great significance for developing highly efficient catalysts for ammonia

synthesis and improving reaction selectivity, and provide a basis for further catalyst design and optimization.

The Chapter 4 focuses on exploring methods for improving the performance of Co_3O_4 catalysts, and found that Co_3O_4 can obtain extremely high catalytic ability on carbon paper supports.

First, we introduce the application of Co_3O_4 as a catalyst in the reduction of nitrate to ammonia. We summarize the properties and performance of Co_3O_4 in previous studies, including its electrocatalytic activity and selectivity.

We then look at ways to enhance the catalytic performance of Co_3O_4. We chose carbon paper as the support and prepared Co_3O_4catalyst/carbon paper composites. By controlling the preparation conditions and the loading amount of the catalyst, we obtained highly dispersed and uniformly distributed Co_3O_4 particles on carbon paper.

Next, we performed catalytic performance evaluations and compared them with conventional catalysts. Through electrochemical tests and product analysis, we found that the Co_3O_4-CP catalyst exhibited extremely high catalytic ability, high ammonia selectivity and excellent electrocatalytic activity. This result indicates that the catalytic performance of Co3O4 has been significantly enhanced under the synergistic effect of the carbon paper support.

To gain insight into this finding, we performed further characterization and analysis. We studied the structure and morphology of Co_3O_4-CP composites by scanning electron microscopy (SEM), transmission electron microscopy (TEM) and X-ray diffraction (XRD). These characterization results reveal the uniform distribution of Co_3O_4 particles and the conductive properties of carbon paper, providing an explanation for the enhanced catalytic performance.

Finally, we discuss the reason why Co_3O_4-CP exhibits extremely high catalytic ability on carbon paper. We speculate that this may be due to the fact that the carbon paper provides a better electron transport path and a larger active surface area, which promotes the reactivity of the Co_3O_4 catalyst.

In summary, the fourth chapter focuses on improving the performance of Co_3O_4-CP catalysts, and found that Co_3O_4-CP can obtain extremely high catalytic ability on carbon paper supports. This study provides important insights into the development of highly efficient catalysts for ammonia synthesis

and optimization of support materials, and provides valuable guidance for further research and applications in related fields.

Acknowledgements

This piece of work and my three years in the Doctoral program at Tohoku University would not be successful without the guidance, invaluable contributions, and inspiration of great individuals.

First and foremost, I am immeasurably grateful to Prof. Chihiro Inoue, my supervisor, for his kindly guidance and untiring support. His professional conduct and attitudes have changed my perspective and inspired me a lot. Without any of the roles he played, I would not be able to come to Japan, finish my doctoral degree. I am forever grateful to his generosity.

My deepest appreciations and heartfelt thanks to Industry-academia-government collaboration Researcher Huang Yi for his supervision and support through the years. My discussion with him were indeed stimulating and his suggestions were truly beneficial to my research. His wit and vigor are equally inspiring. I appreciate his extremely valuable assistance from sampling to the writing of this research work.

I am indebted to Assoc. Proc. Chien meifang for her valuable comments and bright insights have improved my experiment skill.

I would like to express our sincere gratitude to Prof. Takahashi and Prof. Kamitakahara for valuable advice from the interim defenses to the final defenses.

Achievement list

Publications in doctoral period：

1) Rao, X.F., et al., Recent progress in noble metal electrocatalysts for nitrogen-to-ammonia conversion. Renewable & Sustainable Energy Reviews, 2022. 168. (Chapter 1, doi.org/10.1016/j.rser.2022.112845)
2) Rao, X.F., et al., A porous Co_3O_4-carbon paper electrode enabling nearly 100% electrocatalytic reduction of nitrate to ammonia，Materials Reports Energy. (Chapter 4, doi.org/10.1016/j.matre.2023.100216)

Reference

1. Seo, Y. and S. Han, *Economic Evaluation of an Ammonia-Fueled Ammonia Carrier Depending on Methods of Ammonia Fuel Storage.* Energies, 2021. **14**(24): p. 8326.
2. Machaj, K., et al., *Ammonia as a potential marine fuel: A review.* Energy Strategy Reviews, 2022. **44**: p. 100926.
3. Güthner, T. and B. Mertschenk, *Cyanamides*, in *Ullmann's Encyclopedia of Industrial Chemistry*. 2006.
4. Scherer, H.W., et al., *Fertilizers, 1. General*, in *Ullmann's Encyclopedia of Industrial Chemistry*. 2009.
5. Service, R.F., *Liquid sunshine*. 2018, American Association for the Advancement of Science.
6. Hao, Q., et al., *Catalytic reduction of nitrogen to produce ammonia by bismuth-based catalysts: state of the art and future prospects.* Materials Horizons, 2020. **7**(4): p. 1014-1029.
7. Van der Ham, C.J., M.T. Koper, and D.G. Hetterscheid, *Challenges in reduction of dinitrogen by proton and electron transfer.* Chemical Society Reviews, 2014. **43**(15): p. 5183-5191.
8. Qin, Q., et al., *Single-site gold catalysts on hierarchical N-doped porous noble carbon for enhanced electrochemical reduction of nitrogen.* Small Methods, 2018. **2**(12): p. 1800202.
9. Khalil, I.E., et al., *The Role of Defects in Metal–Organic Frameworks for Nitrogen Reduction Reaction: When Defects Switch to Features.* Advanced Functional Materials, 2021. **31**(17): p. 2010052.
10. Medford, A.J., et al., *From the Sabatier principle to a predictive theory of transition-metal heterogeneous catalysis.* Journal of Catalysis, 2015. **328**: p. 36-42.
11. Bao, D., et al., *Electrochemical reduction of N2 under ambient conditions for artificial N2 fixation and renewable energy storage using N2/NH3 cycle.* Advanced materials, 2017. **29**(3): p. 1604799.
12. Pang, F., et al., *Bimodal nanoporous Pd3Cu1 alloy with restrained hydrogen evolution for stable and high yield electrochemical nitrogen reduction.* Nano Energy, 2019. **58**: p. 834-841.
13. Bao, D., et al., *Electrochemical Reduction of N_2 under Ambient Conditions for Artificial N_2 Fixation and Renewable Energy Storage Using N_2/NH_3 Cycle.* Advanced Materials, 2017. **29**(3): p. 1604799.
14. Zheng, J., et al., *Photoelectrochemical Synthesis of Ammonia on the Aerophilic-Hydrophilic Heterostructure with 37.8% Efficiency.* Chem, 2019. **5**(3): p. 617-633.
15. Zhang, K., et al., *Low-Coordinated Gold Atoms Boost Electrochemical Nitrogen Reduction Reaction under Ambient Conditions.* ACS Sustainable Chemistry & Engineering, 2019. **7**(12): p. 10214-10220.
16. Zhang, W., et al., *Facet-Dependent Catalytic Performance of Au Nanocrystals for Electrochemical Nitrogen Reduction.* ACS Applied Materials & Interfaces, 2020. **12**(37): p. 41613-41619.
17. Shi, M.M., et al., *Au Sub-Nanoclusters on TiO_2 toward Highly Efficient and Selective Electrocatalyst for N_2 Conversion to NH_3 at Ambient Conditions.* Advanced Materials, 2017. **29**(17): p. 1606550.
18. Zhang, J., et al., *Adsorbing and Activating N_2 on Heterogeneous Au–Fe_3O_4 Nanoparticles for N_2 Fixation.* Advanced Functional Materials, 2019. **30**(4): p. 1906579.

19. Li, Y., et al., *High-efficiency electrocatalyst for N2 conversion to NH3 based on Au nanoparticles loaded on defective WO3−x.* Chemical Communications, 2019. **55**(88): p. 13307-13310.
20. Zheng, J., et al., *Tuning the Electron Localization of Gold Enables the Control of Nitrogen-to-Ammonia Fixation.* Angewandte Chemie International Edition, 2019. **58**(51): p. 18604-18609.
21. Zhao, S., et al., *An oxygen vacancy-rich two-dimensional Au/TiO_2 hybrid for synergistically enhanced electrochemical N_2 activation and reduction.* Journal of Materials Chemistry A, 2020. **8**(14): p. 6586-6596.
22. Liu, D., et al., *Synergistic Electrocatalytic Nitrogen Reduction Enabled by Confinement of Nanosized Au Particles onto a Two-Dimensional Ti3C2 Substrate.* ACS Applied Materials & Interfaces, 2019. **11**(29): p. 25758-25765.
23. Li, S.J., et al., *Amorphizing of Au Nanoparticles by CeOx -RGO Hybrid Support towards Highly Efficient Electrocatalyst for N_2 Reduction under Ambient Conditions.* Advanced Materials, 2017. **29**(33): p. 1700001.
24. Li, Y., et al., *Boron-doped silver nanosponges with enhanced performance towards electrocatalytic nitrogen reduction to ammonia.* Chemical Communications, 2019. **55**(98): p. 14745-14748.
25. Ji, L., et al., *Nanostructured Bromide-Derived Ag Film: An Efficient Electrocatalyst for N2 Reduction to NH3 under Ambient Conditions.* Inorganic Chemistry, 2018. **57**(23): p. 14692-14697.
26. Huang, H., et al., *Ag nanosheets for efficient electrocatalytic N_2 fixation to NH_3 under ambient conditions.* Chemical Communications, 2018. **54**(81): p. 11427-11430.
27. Li, X., H. Xie, and J. Mao, *Ag nanoparticles-reduced graphene oxide hybrid: an efficient electrocatalyst for artificial N2 fixation to NH3 at ambient conditions.* Journal of Materials Science, 2020. **55**(12): p. 5203-5210.
28. Gao, W.Y., et al., *Morphology-dependent electrocatalytic nitrogen reduction on Ag triangular nanoplates.* Chemical Communications, 2019. **55**(72): p. 10705-10708.
29. Kordali, V., G. Kyriacou, and C. Lambrou, *Electrochemical synthesis of ammonia at atmospheric pressure and low temperature in a solid polymer electrolyte cell.* Chemical Communications, 2000(17): p. 1673-1674.
30. Zhao, L., et al., *Artificial N_2 fixation to NH_3 by electrocatalytic Ru NPs at low overpotential.* Nanotechnology, 2020. **31**(29): p. 29LT01.
31. Wang, D., et al., *Energy-Efficient Nitrogen Reduction to Ammonia at Low Overpotential in Aqueous Electrolyte under Ambient Conditions.* ChemSusChem, 2018. **11**(19): p. 3416-3422.
32. Xu, G.R., et al., *Ruthenium(iii) polyethyleneimine complexes for bifunctional ammonia production and biomass upgrading.* Journal of Materials Chemistry A, 2019. **7**(44): p. 25433-25440.
33. Liu, H.M., et al., *Surfactant-free atomically ultrathin rhodium nanosheet nanoassemblies for efficient nitrogen electroreduction.* Journal of Materials Chemistry A, 2018. **6**(7): p. 3211-3217.
34. Chen, T., et al., *Reactive Ionic Liquid Enables the Construction of 3D Rh Particles with Nanowire Subunits for Electrocatalytic Nitrogen Reduction.* Chemistry-An Asian Journal, 2020. **15**(7): p. 1081-1087.
35. Kugler, K., et al., *Galvanic deposition of Rh and Ru on randomly structured Ti felts for the electrochemical NH_3 synthesis.* Physical Chemistry Chemical Physics, 2015. **17**(5): p. 3768-3782.

36. Xu, W., et al., *Nanoporous Palladium Hydride for Electrocatalytic N_2 Reduction under Ambient Conditions.* Angewandte Chemie International Edition, 2020. **59**(9): p. 3511-3516.
37. Lv, J., et al., *Interface and defect engineer of titanium dioxide supported palladium or platinum for tuning the activity and selectivity of electrocatalytic nitrogen reduction reaction.* J Colloid Interface Sci, 2019. **553**: p. 126-135.
38. Wang, J., et al., *Ambient ammonia synthesis via palladium-catalyzed electrohydrogenation of dinitrogen at low overpotential.* Nature Communications, 2018. **9**(1): p. 1795.
39. Lan, R., J.T.S. Irvine, and S. Tao, *Synthesis of ammonia directly from air and water at ambient temperature and pressure.* Scientific Reports, 2013. **3**(1): p. 1145.
40. Lan, R. and S. Tao, *Electrochemical synthesis of ammonia directly from air and water using a $Li^+/H^+/NH_4^+$ mixed conducting electrolyte.* RSC Advances, 2013. **3**(39): p. 18016-18021.
41. Sheets, B.L. and G.G. Botte, *Electrochemical nitrogen reduction to ammonia under mild conditions enabled by a polymer gel electrolyte.* Chemical Communications, 2018. **54**(34): p. 4250-4253.
42. Du, C., et al., *Interface hydrophobic tunnel engineering: A general strategy to boost electrochemical conversion of N_2 to NH_3.* Nano Energy, 2022. **92**: p. 106784.
43. Deng, Y., et al., *The rational adjusting of proton-feeding by Pt-doped FeP/C hollow nanorod for promoting nitrogen reduction kinetics.* Applied Catalysis B: Environmental, 2021. **291**: p. 120047.
44. Zhang, M., et al., *Pt/TiO_{2-x} nanofibrous aerogel for effective nitrogen reduction: A simple strategy for simultaneous Pt formation and TiO_{2-x} vacancy engineering.* Chinese Chemical Letters, 2021.
45. Nash, J., et al., *Electrochemical Nitrogen Reduction Reaction on Noble Metal Catalysts in Proton and Hydroxide Exchange Membrane Electrolyzers.* Journal of the Electrochemical Society, 2017. **164**(14): p. F1712-F1716.
46. Dai, Z., et al., *Phosphorus incorporation accelerates ammonia electrosynthesis over a mesoporous Au film.* Chemical Communications, 2022.
47. Wang, X., et al., *Atomically dispersed Au_1 catalyst towards efficient electrochemical synthesis of ammonia.* Science Bulletin, 2018. **63**(19): p. 1246-1253.
48. Qin, Q., et al., *Single-Site Gold Catalysts on Hierarchical N-Doped Porous Noble Carbon for Enhanced Electrochemical Reduction of Nitrogen.* Small Methods, 2018. **2**(12): p. 1800202.
49. Chen, Y., et al., *Highly Productive Electrosynthesis of Ammonia by Admolecule-Targeting Single Ag Sites.* ACS Nano, 2020. **14**(6): p. 6938-6946.
50. Hao, R., et al., *Efficient Electrochemical Nitrogen Fixation over Isolated Pt Sites.* Small, 2020. **16**(22): p. 2000015.
51. Peng, W., et al., *Spontaneous Atomic Ruthenium Doping in Mo_2CTX MXene Defects Enhances Electrocatalytic Activity for the Nitrogen Reduction Reaction.* Advanced Energy Materials, 2020. **10**(25): p. 2001364.
52. Yu, B., et al., *Tuning the Catalytic Preference of Ruthenium Catalysts for Nitrogen Reduction by Atomic Dispersion.* Advanced Functional Materials, 2020. **30**(6): p. 1905665.
53. Tao, H.C., et al., *Nitrogen Fixation by Ru Single-Atom Electrocatalytic Reduction.* Chem, 2019. **5**(1): p. 204-214.
54. Geng, Z., et al., *Achieving a Record-High Yield Rate of 120.9 μg NH_3 $mg_{cat.}^{-1}$ h^{-1} for N_2 Electrochemical Reduction over Ru Single-Atom Catalysts* Advanced Materials, 2018. **30**(40): p. 1803498.

55. Liu, Y., et al., *Coupling Cu with Au for enhanced electrocatalytic activity of nitrogen reduction reaction.* Nanoscale, 2020. **12**(3): p. 1811-1816.
56. Xue, Z.H., et al., *Electrochemical Reduction of N2 into NH3 by Donor-Acceptor Couples of Ni and Au Nanoparticles with a 67.8% Faradaic Efficiency.* J Am Chem Soc, 2019. **141**(38): p. 14976-14980.
57. Mao, Y.J., et al., *Excavated cubic platinum-iridium alloy nanocrystals with high-index facets as highly efficient electrocatalysts in N_2 fixation to NH_3.* Chemical Communications, 2019. **55**(63): p. 9335-9338.
58. Tong, W., et al., *Exposed facet-controlled N_2 electroreduction on distinct Pt_3Fe nanostructures of nanocubes, nanorods and nanowires.* National Science Review, 2020. **8**(1): p. nwaa088.
59. Tong, W., et al., *Crystal-Phase-Engineered PdCu Electrocatalyst for Enhanced Ammonia Synthesis.* Angewandte Chemie International Edition, 2020. **59**(7): p. 2649-2653.
60. Nazemi, M., et al., *Electrosynthesis of Ammonia Using Porous Bimetallic Pd–Ag Nanocatalysts in Liquid- and Gas-Phase Systems.* ACS Catalysis, 2020. **10**(17): p. 10197-10206.
61. Pang, F., et al., *Hierarchical nanoporous Pd_1Ag_1 alloy enables efficient electrocatalytic nitrogen reduction under ambient conditions.* Chemical Communications, 2019. **55**(68): p. 10108-10111.
62. Fu, W., et al., *Pd-Co nanoalloys nested on CuO nanosheets for efficient electrocatalytic N_2 reduction and room-temperature Suzuki-Miyaura coupling reaction.* Nanoscale, 2019. **11**(3): p. 1379-1385.
63. Yang, L., et al., *PdAgCu Alloy Nanoparticles Integrated on Three-Dimensional Nanoporous CuO for Efficient Electrocatalytic Nitrogen Reduction under Ambient Conditions.* Langmuir, 2020. **36**(19): p. 5112-5117.
64. Guo, J., et al., *Tunable synthesis of multiply twinned intermetallic Pd_3Pb nanowire networks toward efficient N_2 to NH_3 conversion.* Journal of Materials Chemistry A, 2019. **7**(35): p. 20247-20253.
65. Wang, Q.Q., et al., *Au_1Co_1 Alloy Supported on Graphene Oxide with Enhanced Performance for Ambient Electrolysis of Nitrogen to Ammonia.* ACS Sustainable Chemistry & Engineering, 2020. **8**(1): p. 44-49.
66. Shi, M.M., et al., *Anchoring PdCu Amorphous Nanocluster on Graphene for Electrochemical Reduction of N_2 to NH_3 under Ambient Conditions in Aqueous Solution.* Advanced Energy Materials, 2018. **8**(21): p. 1800124.
67. Liu, A., et al., *Two-dimensional CuAg/Ti_3C_2 catalyst for electrochemical synthesis of ammonia under ambient conditions: a combined experimental and theoretical study.* Sustainable Energy & Fuels, 2020. **4**(10): p. 5061-5071.
68. Manjunatha, R. and A. Schechter, *Electrochemical synthesis of ammonia using ruthenium-platinum alloy at ambient pressure and low temperature.* Electrochemistry Communications, 2018. **90**: p. 96-100.
69. Zhang, J., et al., *Sustainable nitrogen fixation over Ru single atoms decorated Cu_2O using electrons produced from photoelectrocatalytic organics degradation.* Chemical Engineering Journal, 2022. **428**: p. 130373.
70. Zhao, L., et al., *Rational design of bimetallic $Rh_{0.6}Ru_{0.4}$ nanoalloys for enhanced nitrogen reduction electrocatalysis under mild conditions.* Journal of Materials Chemistry A, 2021. **9**(1): p. 259-263.
71. Lv, J., et al., *Construction of PdO–Pd interfaces assisted by laser irradiation for enhanced electrocatalytic N_2 reduction reaction.* Journal of Materials Chemistry A, 2019. **7**(20): p. 12627-12634.

72. Xie, H.T., et al., *PdP_2 nanoparticles-reduced graphene oxide for electrocatalytic N_2 conversion to NH_3 under ambient conditions.* Journal of Materials Chemistry A, 2019. **7**(43): p. 24760-24764.
73. Yang, X., et al., *Low-Coordinate Step Atoms via Plasma-Assisted Calcinations to Enhance Electrochemical Reduction of Nitrogen to Ammonia.* Small, 2020. **16**(17): p. 2000421.
74. Zhang, W., et al., *Enhancing electrochemical nitrogen reduction with Ru nanowires via the atomic decoration of Pt.* Journal of Materials Chemistry A, 2020. **8**(47): p. 25142-25147.
75. Wang, H.J., et al., *Metal-Nonmetal One-Dimensional Electrocatalyst: AuPdP Nanowires for Ambient Nitrogen Reduction to Ammonia.* ACS Sustainable Chemistry & Engineering, 2019. **7**(18): p. 15772-15777.
76. Wang, H., et al., *Three-dimensional Pd-Ag-S porous nanosponges for electrocatalytic nitrogen reduction to ammonia.* Nanoscale, 2020. **12**(25): p. 13507-13512.
77. Wang, Z., et al., *Effects of AuCuB Catalysts with Porous Nanostructures on Electrosynthesis of Ammonia.* ACS Sustainable Chemistry & Engineering, 2020. **8**(33): p. 12588-12594.
78. Li, W., et al., *Ambient Electrosynthesis of Ammonia Using Core-Shell Structured Au@C Catalyst Fabricated by One-Step Laser Ablation Technique.* ACS Applied Materials & Interfaces, 2019. **11**(47): p. 44186-44195.
79. Liu, G., et al., *Ambient Electrosynthesis of Ammonia on a Core-Shell-Structured $Au@CeO_2$ Catalyst: Contribution of Oxygen Vacancies in CeO_2.* Chemistry, 2019. **25**(23): p. 5904-5911.
80. Yang, C., et al., *A Generalized Surface Chalcogenation Strategy for Boosting the Electrochemical N_2 Fixation of Metal Nanocrystals.* Advanced Materials, 2020. **32**(24): p. e2001267.
81. Nazemi, M., S.R. Panikkanvalappil, and M.A. El-Sayed, *Enhancing the rate of electrochemical nitrogen reduction reaction for ammonia synthesis under ambient conditions using hollow gold nanocages.* Nano Energy, 2018. **49**: p. 316-323.
82. Nazemi, M. and M.A. El-Sayed, *The Role of Oxidation of Silver in Bimetallic Gold-Silver Nanocages on Electrocatalytic Activity of Nitrogen Reduction Reaction.* Journal of Physical Chemistry C, 2019. **123**(18): p. 11422-11427.
83. Nazemi, M., et al., *Ambient Ammonia Electrosynthesis from Nitrogen and Water by Incorporating Palladium in Bimetallic Gold-Silver Nanocages.* Journal of the Electrochemical Society, 2020. **167**(5): p. 054511.
84. Zhang, Q.W., et al., *Composition-dependent electrochemical activity of Ag-based alloy nanotubes for efficient nitrogen reduction under ambient conditions.* Electrochimica Acta, 2019. **321**: p. 134691.
85. Zhang, N., et al., *Surface-Regulated Rhodium-Antimony Nanorods for Nitrogen Fixation.* Angewandte Chemie International Edition, 2020. **59**(21): p. 8066-8071.
86. Wang, H., et al., *Direct fabrication of bi-metallic PdRu nanorod assemblies for electrochemical ammonia synthesis.* Nanoscale, 2019. **11**(12): p. 5499-5505.
87. Wang, J., et al., *A General Strategy to Glassy M-Te (M = Ru, Rh, Ir) Porous Nanorods for Efficient Electrochemical N_2 Fixation.* Advanced Materials, 2020. **32**(11): p. 1907112.
88. Bai, J., et al., *Glycerol oxidation assisted electrocatalytic nitrogen reduction: ammonia and glyceraldehyde co-production on bimetallic RhCu ultrathin nanoflake nanoaggregates.* Journal of Materials Chemistry A, 2019. **7**(37): p. 21149-21156.

89. Wang, Z., et al., *Ambient Electrochemical Synthesis of Ammonia from Nitrogen and Water Catalyzed by Flower-Like Gold Microstructures.* ChemSusChem, 2018. **11**(19): p. 3480-3485.
90. Wang, H.J., et al., *One-pot synthesis of bi-metallic PdRu tripods as an efficient catalyst for electrocatalytic nitrogen reduction to ammonia.* Journal of Materials Chemistry A, 2019. **7**(2): p. 801-805.
91. Kumar, R.D., et al., *Trimetallic PdCuIr with long-spined sea-urchin-like morphology for ambient electroreduction of nitrogen to ammonia.* Journal of Materials Chemistry A, 2019. **7**(7): p. 3190-3196.
92. Yu, H., et al., *Bimetallic Ag_3Cu porous networks for ambient electrolysis of nitrogen to ammonia.* Journal of Materials Chemistry A, 2019. **7**(20): p. 12526-12531.
93. Pang, F.J., et al., *Bimodal nanoporous Pd_3Cu_1 alloy with restrained hydrogen evolution for stable and high yield electrochemical nitrogen reduction.* Nano Energy, 2019. **58**: p. 834-841.
94. Wang, Z.Q., et al., *Ambient Nitrogen Reduction to Ammonia Electrocatalyzed by Bimetallic PdRu Porous Nanostructures.* ACS Sustainable Chemistry & Engineering, 2019. **7**(2): p. 2400-2405.
95. Li, Y.H., et al., *One-step synthesis of self-standing porous palladium-ruthenium nanosheet array on Ni foam for ambient electrosynthesis of ammonia.* International Journal of Hydrogen Energy, 2020. **45**(11): p. 5997-6005.
96. Zhao, H., et al., *High-performance nitrogen electroreduction at low overpotential by introducing Pb to Pd nanosponges.* Applied Catalysis B-Environmental, 2020. **265**: p. 118481.
97. Lee, H.K., et al., *Favoring the unfavored: Selective electrochemical nitrogen fixation using a reticular chemistry approach.* Science Advances, 2018. **4**(3): p. eaar3208.
98. Lv, X.W., et al., *ZIF-supported AuCu nanoalloy for ammonia electrosynthesis from nitrogen and thin air.* Journal of Materials Chemistry A, 2020. **8**(18): p. 8868-8874.
99. Yang, Y., et al., *Nanoporous Gold Embedded ZIF Composite for Enhanced Electrochemical Nitrogen Fixation.* Angewandte Chemie International Edition, 2019. **58**(43): p. 15362-15366.
100. Sim, H.Y.F., et al., *ZIF-Induced d-Band Modification in a Bimetallic Nanocatalyst: Achieving Over 44 % Efficiency in the Ambient Nitrogen Reduction Reaction.* Angewandte Chemie International Edition, 2020. **59**(39): p. 16997-17003.
101. Zhao, X., et al., *In situ nano Au triggered by a metal boron organic polymer: efficient electrochemical N_2 fixation to NH3 under ambient conditions.* Journal of Materials Chemistry A, 2019. **7**(36): p. 20945-20951.
102. Wang, H., et al., *Ambient Electrosynthesis of Ammonia: Electrode Porosity and Composition Engineering.* Angewandte Chemie International Edition, 2018. **57**(38): p. 12360-12364.
103. Xiong, W., et al., *Electrocatalytic ammonia synthesis catalyzed by mesoporous nickel oxide nanosheets loaded with Pt nanoparticles.* Chinese Journal of Catalysis, 2022. **43**(5): p. 1371-1378.
104. Zhang, M., et al., *A mesoporous Au film with surface sulfur modification for efficient ammonia electrosynthesis.* Journal of Materials Chemistry A, 2020. **8**(39): p. 20414-20419.
105. Zhao, Y., et al., *Revealing Ammonia Quantification Minefield in Photo/Electrocatalysis.* Angewandte Chemie International Edition, 2021. **60**(40): p. 21728-21731.
106. Choi, J., et al., *Identification and elimination of false positives in electrochemical nitrogen reduction studies.* Nature communications, 2020. **11**(1): p. 1-10.

107. Rivett, M.O., et al., *Nitrate attenuation in groundwater: a review of biogeochemical controlling processes.* Water research, 2008. **42**(16): p. 4215-4232.
108. Fujii, H., K. Nakagawa, and M. Kagabu, *Decomposition approach of the nitrogen generation process: empirical study on the Shimabara Peninsula in Japan.* Environmental Science and Pollution Research, 2016. **23**(22): p. 23249-23261.
109. Kumazawa, K., *Nitrogen fertilization and nitrate pollution in groundwater in Japan: Present status and measures for sustainable agriculture.* Nutrient Cycling in Agroecosystems, 2002. **63**(2): p. 129-137.
110. Zhou, M., W. Wang, and M. Chi, *Enhancement on the simultaneous removal of nitrate and organic pollutants from groundwater by a three-dimensional bio-electrochemical reactor.* Bioresource Technology, 2009. **100**(20): p. 4662-4668.
111. Islam, M. and R. Patel, *Synthesis and physicochemical characterization of Zn/Al chloride layered double hydroxide and evaluation of its nitrate removal efficiency.* Desalination, 2010. **256**(1-3): p. 120-128.
112. Cao, M., et al., *Domestic wastewater causes nitrate pollution in an agricultural watershed, China.* Science of The Total Environment, 2022. **823**: p. 153680.
113. Tyagi, S., et al., *Strategies for Nitrate removal from aqueous environment using Nanotechnology: A Review.* Journal of Water Process Engineering, 2018. **21**: p. 84-95.
114. Teimouri, A., et al., *Chitosan /Zeolite Y/Nano ZrO2 nanocomposite as an adsorbent for the removal of nitrate from the aqueous solution.* International Journal of Biological Macromolecules, 2016. **93**: p. 254-266.
115. Alikhani, M. and M. Moghbeli, *Ion-exchange polyHIPE type membrane for removing nitrate ions: Preparation, characterization, kinetics and adsorption studies.* Chemical engineering journal, 2014. **239**: p. 93-104.
116. Mendow, G., et al., *A novel process for nitrate reduction in water using bimetallic Pd-Cu catalysts supported on ion exchange resin.* Journal of environmental chemical engineering, 2017. **5**(2): p. 1404-1414.
117. Primo, O., et al., *Nitrate removal from electro-oxidized landfill leachate by ion exchange.* Journal of hazardous materials, 2009. **164**(1): p. 389-393.
118. Egea-Corbacho, A., S.G. Ruiz, and J.M.Q. Alonso, *Removal of emerging contaminants from wastewater using nanofiltration for its subsequent reuse: Full–scale pilot plant.* Journal of Cleaner Production, 2019. **214**: p. 514-523.
119. Epsztein, R., et al., *Elucidating the mechanisms underlying the difference between chloride and nitrate rejection in nanofiltration.* Journal of Membrane Science, 2018. **548**: p. 694-701.
120. Reig, M., et al., *Rejection of ammonium and nitrate from sodium chloride solutions by nanofiltration: Effect of dominant-salt concentration on the trace-ion rejection.* Chemical engineering journal, 2016. **303**: p. 401-408.
121. Park, J.Y. and Y.J. Yoo, *Biological nitrate removal in industrial wastewater treatment: which electron donor we can choose.* Applied microbiology and biotechnology, 2009. **82**(3): p. 415-429.
122. Mousavi, S., et al., *Development of nitrate elimination by autohydrogenotrophic bacteria in bio-electrochemical reactors–A review.* Biochemical Engineering Journal, 2012. **67**: p. 251-264.
123. Pous, N., et al., *Cathode potential and anode electron donor evaluation for a suitable treatment of nitrate-contaminated groundwater in bioelectrochemical systems.* Chemical Engineering Journal, 2015. **263**: p. 151-159.
124. Rao, X., et al., *Efficient nitrate removal from water using selected cathodes and Ti/PbO2 anode: Experimental study and mechanism verification.* Separation and Purification Technology, 2019. **216**: p. 158-165.

125. Li, J., et al., *Efficient Ammonia Electrosynthesis from Nitrate on Strained Ruthenium Nanoclusters.* Journal of the American Chemical Society, 2020. **142**(15): p. 7036-7046.
126. Wang, Y., et al., *Unveiling the Activity Origin of a Copper-based Electrocatalyst for Selective Nitrate Reduction to Ammonia.* Angewandte Chemie International Edition, 2020. **59**(13): p. 5350-5354.
127. Wang, Y., et al., *Enhanced Nitrate-to-Ammonia Activity on Copper–Nickel Alloys via Tuning of Intermediate Adsorption.* Journal of the American Chemical Society, 2020. **142**(12): p. 5702-5708.
128. McEnaney, J.M., et al., *Electrolyte Engineering for Efficient Electrochemical Nitrate Reduction to Ammonia on a Titanium Electrode.* ACS Sustainable Chemistry & Engineering, 2020. **8**(7): p. 2672-2681.
129. Jia, R., et al., *Boosting Selective Nitrate Electroreduction to Ammonium by Constructing Oxygen Vacancies in TiO2.* ACS Catalysis, 2020. **10**(6): p. 3533-3540.
130. Chen, G.-F., et al., *Electrochemical reduction of nitrate to ammonia via direct eight-electron transfer using a copper–molecular solid catalyst.* Nature Energy, 2020. **5**(8): p. 605-613.
131. Kyriakou, V., et al., *An Electrochemical Haber-Bosch Process.* Joule, 2020. **4**(1): p. 142-158.
132. Liu, J.-X., et al., *Activity and Selectivity Trends in Electrocatalytic Nitrate Reduction on Transition Metals.* ACS Catalysis, 2019. **9**(8): p. 7052-7064.
133. Li, Y., et al., *Hydrogen Evolution Electrocatalyst Design: Turning Inert Gold into Active Catalyst by Atomically Precise Nanochemistry.* Journal of the American Chemical Society, 2021. **143**(29): p. 11102-11108.
134. Lee, Y.-I., et al., *Tunable synthesis of cuprous and cupric oxide nanotubes from electrodeposited copper nanowires.* Journal of nanoscience and nanotechnology, 2011. **11**(2): p. 1455-1458.
135. Lee, Y.-I., *Selective transformation of Cu nanowires to Cu2S or CuS nanostructures and the roles of the Kirkendall effect and anion exchange reaction.* Materials Chemistry and Physics, 2016. **180**: p. 104-113.
136. Han, Z., et al., *High Efficient Mesoporous Co3O4 Nanocatalysts For Methane Combustion at Low Temperature.* 2016. **1**(5): p. 979-983.
137. Wang, H.J., et al., *Mesoporous Co3O4 for Low Temperature CO Oxidation: Effect of Calcination Temperatures on Their Catalytic Performance.* Journal of Nanoscience and Nanotechnology, 2011. **11**(5): p. 3843-3850.
138. Wang, Y.X., et al., *Enhanced exchange bias of isolated Co/CoO nanocaps.* Journal of Alloys and Compounds, 2011. **509**(23): p. 6626-6630.
139. Deng, X., et al., *Metallic Co Nanoarray Catalyzes Selective NH3 Production from Electrochemical Nitrate Reduction at Current Densities Exceeding 2 A cm−2.* Advanced Science, 2021. **8**(7): p. 2004523.
140. Wang, H. and L.J.C.O.i.E. Gao, *Recent developments in electrochemical hydrogen evolution reaction.* 2018. **7**: p. 7-14.
141. Zou, X., et al., *Cobalt-embedded nitrogen-rich carbon nanotubes efficiently catalyze hydrogen evolution reaction at all pH values.* 2014. **126**(17): p. 4461-4465.
142. Hunt, S.T., T. Nimmanwudipong, and Y.J.A.C. Román-Leshkov, *Engineering Non-sintered, Metal-Terminated Tungsten Carbide Nanoparticles for Catalysis.* 2014. **126**(20): p. 5231-5236.
143. YoungáChung, D., H. ChuláHam, and S.J.N. JongáYoo, *Edge-exposed MoS 2 nano-assembled structures as efficient electrocatalysts for hydrogen evolution reaction.* 2014. **6**(4): p. 2131-2136.

144. Huang, Z., et al., *Cobalt phosphide nanorods as an efficient electrocatalyst for the hydrogen evolution reaction.* 2014. **9**: p. 373-382.
145. Gong, Q., et al., *Ultrathin MoS2 (1–x) Se2 x alloy nanoflakes for electrocatalytic hydrogen evolution reaction.* 2015. **5**(4): p. 2213-2219.
146. Wang, Z.-L., et al., *C and N hybrid coordination derived Co–C–N complex as a highly efficient electrocatalyst for hydrogen evolution reaction.* 2015. **137**(48): p. 15070-15073.
147. Wu, H.B., et al., *Porous molybdenum carbide nano-octahedrons synthesized via confined carburization in metal-organic frameworks for efficient hydrogen production.* 2015. **6**(1): p. 6512.